

Radiative processes in accreting black holes

Grzegorz Wardziński
gwar@camk.edu.pl

PhD Thesis written under the supervision of
Professor Andrzej A. Zdziarski

N. Copernicus Astronomical Center
Warszawa, April 2002

Acknowledgements

In the first place, I would like to thank my supervisor, Professor Andrzej Zdziarski, for his inspiring guidance, support and patience throughout the years of my studies. I am grateful to him for setting ambitious goals and for helping me find my own way to achieve them.

It is a pleasure to thank all the persons, both in the N. Copernicus Astronomical Center and in other institutes, who taught me, with whom I worked or had discussions. I am grateful to them for their invaluable help, for sharing their knowledge with me and showing me different ways of doing science.

Contents

Preface	vii
1 Introduction	1
1.1 The development of X-ray and γ -ray astronomy	2
1.2 Observational properties of accreting black holes	2
1.2.1 Black holes in X-ray binaries	3
1.2.2 Supermassive black holes	5
1.3 Accretion flow models	6
1.3.1 Basic concepts	7
1.3.2 Optically thick accretion flows	8
1.3.3 Optically thin accretion flows	10
1.4 Radiative processes	14
1.4.1 Optically thick disc emission	14
1.4.2 Comptonization	15
1.4.3 X-ray reflection and relativistic effects	18
1.5 Unresolved issues	19
1.5.1 Geometry of the flow	20
1.5.2 The role of magnetic fields	20
1.5.3 The source of seed photons	21
1.5.4 Electron distribution in the hot plasma	22
1.5.5 Other issues	23
2 GX 339–4 observations	25
2.1 The black hole candidate GX 339–4	25
2.2 Data selection and reduction	26
2.3 Spectral models	28
2.3.1 Hard state observations	30
2.3.2 The off state spectrum	37
2.3.3 Temperature – luminosity relation	39
2.4 X-ray variability	41

3	Thermal CS emission	45
3.1	Thermal synchrotron radiation	45
3.1.1	Synchrotron emission coefficient in a thermal plasma	46
3.1.2	Angle-averaged emission coefficient	52
3.1.3	Synchrotron self-absorption	54
3.1.4	Effect of bremsstrahlung on the turnover frequency	56
3.2	Comptonization of synchrotron photons	58
3.2.1	The Comptonization spectrum	58
3.2.2	Synchrotron radiation as a source of soft photons	60
4	CS emission from hybrid plasmas	65
4.1	Hybrid electron distributions	65
4.2	Synchrotron emission from hybrid plasmas	68
4.2.1	Comparison of spectra from thermal and hybrid plasmas	68
4.2.2	Turnover frequency	70
4.3	Hybrid synchrotron self-Comptonization	72
4.3.1	Comptonization by a hybrid electron distribution	74
4.3.2	Hybrid synchrotron emission as seed photons	77
5	CS emission in accretion flows	81
5.1	Thermal CS emission	82
5.1.1	Hot accretion flow model	82
5.1.2	Coronal model - equipartition with radiation energy density	87
5.1.3	Coronal model – dissipation of magnetic field	90
5.1.4	Magnetic fields in the disc	92
5.1.5	General remarks	96
5.2	Hybrid CS emission	97
5.2.1	Efficiency of hybrid CS emission	97
5.2.2	Cygnus X-1	97
5.2.3	GX 339–4	101
5.2.4	General remarks	101
5.3	Optical and X-ray spectrum in GX 339–4	103
6	Summary	109
	Bibliography	115

Preface

It is well known that the black hole, unlike other astrophysical objects, cannot be observed directly.¹ Therefore the only way to discover its presence is through its gravitational interaction with the surrounding matter.

This property, that a physical phenomenon cannot be investigated directly, is not as unique to black holes as it may seem, at least if we adopt a methodological point of view. It is already in the primary school when students are taught that they cannot measure the temperature of water by inserting a thermometer. They can only measure the temperature of the thermometer itself, and (provided the instrument has reached thermal equilibrium with the fluid) from that they can judge about the temperature of water.

Accretion discs, where gravitational energy is released, play the role of ‘black hole thermometers’ in astrophysics. Their radiation, its spectrum and variability patterns are what we read off a thermometer display and from that we judge about the presence of a black hole.

The analogy with simple temperature measurements is, however, not very far-reaching. First of all, we cannot freely choose an instrument that would ‘measure’ properties of the black hole. In fact, we observe a variety of such instruments and even a greater and more puzzling variety of readings. These readings are not calibrated against each other as a result of e.g. different black hole masses or different environmental conditions. Thus, judging from the readings we have at our disposal about the black hole itself (e.g. about its spin) is a most difficult and demanding task.

However, contrary to a simple thermometer, ‘black hole thermometers’ are extremely interesting in themselves. Observations of accreting black holes have stimulated investigation of general relativistic effects, radiative processes throughout the electromagnetic spectrum, physics of magnetized plasmas or experimental X-ray spectroscopy, to name only a few. Thus, while the quest for a definite proof of the existence of black holes may be still the most exciting reason underlying studies of

¹Hawking radiation is negligible for black holes of astrophysical masses.

accretion flows, it is no longer the main one, since these studies themselves are very useful for our understanding of how Nature works.

This Thesis is devoted to the task of obtaining constraints on models of accretion flows onto black holes from X-ray and γ -ray observations, which, in author's humble opinion, is a most exciting way of doing astrophysics. Our framework, which we further extend, is thus defined by contemporary models of accretion flows on one hand and by current observational knowledge on the other. In particular, we investigate Comptonization of synchrotron radiation (which we hereafter abbreviate as the CS process) in a semi-relativistic, optically thin plasma accreting onto a black hole

In Chapter 1 we begin with observational and theoretical background – we present main observational results for accreting black holes both in X-ray binaries and in Active Galactic Nuclei (AGNs), as well as sketch contemporary theoretical models of accretion flows, introduce relevant radiative processes and in particular discuss the remaining caveats in our understanding of accretion flows.

Spectral and temporal analyses of broadband X- and γ -ray observations of an accreting Galactic black hole candidate GX 339–4 are then presented in Chapter 2. The constraints on physical parameters of a plasma close to the black hole we obtain provide us with a framework within which we can test our models of CS emission in an accretion flow.

These models are then developed in Chapter 3, where we investigate thermal, highly self-absorbed synchrotron emission and its subsequent Comptonization in optically thin, thermal plasmas of parameters typical for accreting black holes and obtain convenient analytical description of these processes. This analysis is further extended to the case of hybrid (i.e. containing both a thermal and a non-thermal component) electron distributions in Chapter 4.

In Chapter 5 we finally investigate the efficiency of Comptonized synchrotron emission in accretion flows. For this purpose we introduce simplified models of two accretion flow geometries – a hot disc and a patchy corona. Then, the predictions of our models are tested against observational constraints both from our spectra of GX 339–4 and from spectra of other objects, in particular Cygnus X-1. This allows us for speculating on the strength of magnetic field in accretion flows. The results of the Thesis are eventually summarized and discussed in Chapter 6.

The results presented here are based on the following articles, where the first two have been already published in the Monthly Notices of Royal Astronomical Society and the last one is to be submitted:

- Wardziński G., Zdziarski A. A., *Thermal synchrotron radiation and its Comptonization in compact X-ray sources*, 2000, MNRAS, 314, 183

- Wardziński G., Zdziarski A. A., *Effects of non-thermal tails in Maxwellian electron distributions on synchrotron and Compton processes*, 2001, MNRAS, 325, 963 (Erratum: 2001, MNRAS, 327, 351)
- Wardziński G., Zdziarski A. A., Gierliński M., Grove J. E., Jahoda K., Johnson W. N., *X- and γ -ray observations of the black hole candidate GX 339-4 in the hard state*, 2002, MNRAS, to be submitted

Chapter 1

Introduction

The notion and the basic idea of black holes is more than two hundred years old but it was only in the first half of the previous century when appropriate tools have been developed and the original idea of objects light cannot escape was backed up by theoretical investigations employing the general theory of relativity – the description of gravitational forces as we know them today.

It took still a few more decades until the idea of black holes made it from theoretical investigations to observational approach. The development of X-ray astronomy showed a much larger variety of sources in the sky than optical astronomers had known and opened new horizons for investigations of celestial bodies. Luminous X-ray sources have been observed both in our and in other galaxies. The comparison of their observed luminosities with their sizes (derived from variability time scales) showed that as efficient process of mass to energy conversion as the release of potential energy in a strong gravitational field of a black hole (or a neutron star) is necessary to explain their activity, at least within the framework of the contemporary physics. This process takes place in the form of *accretion* of gas onto the black hole, which is accompanied by emission mainly in the form of UV, X-ray and γ -ray photons.

In this Chapter, we review in short the present state of knowledge on accreting black holes. We start with a concise history of the development of X-ray astronomy. Then, observational results for stellar-mass and supermassive black holes are presented. Following this, we introduce models of accretion flows, main radiative processes, and review some important problems and questions that require further studies.

1.1 The development of X-ray and γ -ray astronomy

Making the development of X-ray and γ -ray astronomy possible required carrying detectors above the Earth's atmosphere, which was achieved for the first time in 1949 with detectors onboard rockets, when X-ray emission from the Sun was observed. In 1965 the first observation of another Galactic source, Sco X-1 was performed, again with a detector onboard a rocket. The satellite era began in the late 1960s and early 1970s with a γ -ray satellite *OSO-3*, X-ray missions *Uhuru* and *HEAO* series and others. Their observations allowed for detection and classification of numerous X-ray sources, among them accreting compact objects – neutron stars and black holes. The 1980s and 1990s brought rapid technical development. Among others, observations by *ROSAT*, *Ginga*, *ASCA*, *CGRO*, *RXTE* and *BeppoSAX* satellites provided broad-band (from hundreds of eV to MeV range) spectra of accreting black holes as well as allowed for timing analysis on millisecond time scales.

It appears that in the first years of the 21st century we are again at the beginning of a new era in high-energy astrophysics. The recent satellite missions *XMM-Newton* and *Chandra* have provided spectral and spatial resolution in the soft X-ray band allowing for much more advanced physical models to be used by astrophysicists. This concerns in particular soft X-ray spectroscopy, which will allow for testing of sophisticated models of the state of the plasma. Missions that will soon start operating, *Integral* (2002), *Astro-E* (2005) and *GLAST* (2006) should produce a similar leap in hard X-ray and γ -ray observations.¹

It has to be noted, however, that so far we have not been able to spatially resolve emission from accretion flows, though a future mission, *Constellation X* (2008), may provide us with such possibility.

1.2 Observational properties of accreting black holes

We observe two separate classes of accreting black holes, the difference being in their masses. The first one is stellar-mass black holes in binary systems (Black Hole Binaries, hereafter BHBs), i.e. those with masses of the order of $10 M_{\odot}$ (where M_{\odot} is the mass of the Sun) and accreting matter from their stellar companions. The other class encompasses supermassive black holes, with masses of the order of

¹The division of the X- and γ -ray spectral band is rather free. In our work we classify emission in the range of hundreds of eV to a few keV as soft X-ray band, then up to tens of keV as hard X-ray band and everything above as γ -rays.

$10^6 - 10^9 M_\odot$, residing in centres of galaxies (AGNs). It has been proposed that there might exist black holes of intermediate masses, of the order of $100 M_\odot$, however this result remains unconfirmed (see Section 1.2.1).

1.2.1 Black holes in X-ray binaries

An X-ray binary may contain an accreting black hole or a neutron star. The latter can be immediately identified if X-ray pulses (due to neutron star rotation) or bursts (resulting from explosions of accumulated gas) are observed. In the lack of these features, the decisive criterion allowing for distinguishing between the two types of compact objects is the mass. All known neutron stars have masses close to the Chandrasekhar limit, $1.4 M_\odot$ (Thorsett & Chakrabarty 1999), and theoretically it is expected that the mass of a neutron star cannot exceed $\approx 3 M_\odot$ (Rhoades & Ruffini 1974).

The mass of the compact object has been measured precisely enough to prove the presence of a black hole² in about ten X-ray binaries. The measured black hole masses were in the range from ~ 5 to $\sim 15 M_\odot$ (e.g. Kubota 2000), which suggests that there is a gap between masses of neutron stars and black holes.

When the mass of the accreting object cannot be determined, other criteria have to be applied, either basing on the spectra or on the variability pattern of the X-ray emission and there is about a dozen of sources classified as black hole candidates.

It has been e.g. proposed (Zdziarski et al. 1998) that Comptonization spectrum produced in a plasma of electron temperature $T_e \gtrsim 7 \times 10^8$ K (or $kT_e \gtrsim 50$ keV, where k is the Boltzmann constant) is a signature of a black hole — on the contrary, Comptonization spectra produced in accretion flows onto neutron stars would indicate the temperature of $kT_e \lesssim 30$ keV. However, Piraino et al. (1999) reported detection of X-ray emission from a plasma of the temperature $kT_e \approx 250$ keV in an accreting neutron star 4U 0614+091.

Another criterion, proposed by Sunyaev & Revnivtsev (2000), employs different shapes of the power density spectra (PDS) of accreting black holes and neutron stars. The main difference lies in the frequency span of the PDS. In the case of accreting black holes, very little variability is observed above ~ 50 Hz, while neutron stars still exhibit strong variability at frequencies $\gtrsim 500$ Hz.

Among accreting black holes in binary systems we observe both persistent and transient sources. In the former (Cygnus X-1 and LMC X-3) strong X-ray emission is observed continuously, while the latter (e.g. GX 339-4) exhibit bursts and quiescence periods. In both classes at least two distinct spectral states are observed, so called soft (historically also known as high) and hard (low).

²Provided the theories of stellar evolution, on which the mass criterion depends, are correct.

In the soft state, the X-ray spectrum is composed of a strong, narrow component peaked at a few keV and a soft power-law spectrum, extending without any observable cut-off up to hundreds of keV (e.g. Grove et al. 1998). The soft X-ray emission is usually attributed to an optically thick disc of temperature varying with radius (we discuss this model in more detail in Section 1.4.1), while the power-law spectrum is expected to originate via the Compton process (Section 1.4.2) in optically thin, hot plasmas (e.g. Gierliński et al. 1999). Superimposed on the latter component are signatures of Compton reflection of the power-law emission from a cold medium, presumably the optically thick disc, including a fluorescent iron $K\alpha$ line (Section 1.4.3).

The hard state is characterized by much weaker soft component, which peaks below 1 keV. On the other hand the Comptonized component is harder and much more prominent, extending up to ~ 100 keV, where a cut-off (most likely of thermal origin) is observed. Similar reflection features are found (e.g. Gierliński et al. 1997).

Usually the luminosity of a black hole in the hard state is lower than that in the soft one and is of the order of a few per cent of the Eddington luminosity. The latter corresponds to the balance between gravitation and radiation pressure in a spherical plasma cloud and can be approximated as

$$L_E \approx 1.5 \times 10^{38} \frac{M}{M_\odot} \text{ erg s}^{-1}, \quad (1.1)$$

where M is the mass of the black hole. Thus, the typical luminosity of a BHB in the hard state, with a $10 M_\odot$ black hole, would be of the order of 10^{37} erg s^{-1} .

For completeness we mention that BHBs are also observed in other spectral states – the very high state (which is basically a sum of the soft and hard state spectra, with prominent disc component and hard Comptonization spectrum) when the luminosity is close to the Eddington one, and the quiescent state, when the luminosity is extremely low (see, e.g., Done 2002 and references therein).

BHBs in the hard state exhibit significant rapid X-ray variability with typical time scales from milliseconds to hours (e.g. Revnivtsev, Gilfanov & Churazov 2001). In the soft state the X-ray variability is typically weaker than in the hard state (e.g. van der Klis 1994). Also variability on much longer time scales is observed, which is however related not to innermost parts of the accretion flow, but rather to varying accretion rate or changes in outer parts of the accretion disc (e.g. Chen, Shrader & Livio 1997).

In the hard state radio emission from accreting black holes is often observed and attributed to synchrotron radiation in large scale outflows in the system. Extreme cases are objects with high accretion rates, where the outflow producing radio emission is highly collimated and ultra-relativistic (e.g. GRS 1915+105) – so called microquasars (e.g. Mirabel & Rodriguez 1999).

There is also a separate class of objects, Ultra Luminous X-ray sources (ULXs), observed in nearby galaxies. Their luminosities are of the order of 10^{40} erg s $^{-1}$, while their spectral properties are in general similar to Galactic BHBs. These sources may correspond to black holes with masses of the order of $100 M_{\odot}$ accreting moderately (Makishima et al. 2000), though this interpretation remains doubtful as many ULXs have been found in star-forming regions. Another possibility would be that we observe beamed (and thus amplified) X-ray emission from high-mass X-ray binaries (King et al. 2001), which would be then a phenomenon similar to microquasars.

1.2.2 Supermassive black holes

In the case of supermassive black holes, residing in centres of galaxies, the variety of different types of objects, classified by their spectral properties, is larger than for BHBs (see e.g. Véron-Cetty & Véron 2000 for a recent review). This results most likely from more complicated and diverse environment of supermassive black holes, as well as from better statistics due to much larger number of objects observed.

The first classification criterion is the luminosity of the active nucleus compared to that of the host galaxy. Objects where the central engine outshines the galaxy emission so that it is hardly observable, have been historically classified as quasars. On the other hand, when the galaxy emission could be observed, the sources were described as active galaxies. X-ray and bolometric luminosities of quasars amount to $\sim 10^{46}$ and $\sim 10^{48}$ erg s $^{-1}$, respectively. In general, luminous active galaxies are by at least two magnitudes weaker. On the other hand, low-luminosity active galaxies have their X-ray luminosities at the level of $10^{40} - 10^{41}$ erg s $^{-1}$.

The inclination at which an AGN is observed is an important factor determining its spectrum, as was shown by Antonucci & Miller (1985) and is the key point of the classification scheme of active galaxies. AGNs observed at low inclinations have broad optical emission lines (corresponding to velocities of a few thousand km s $^{-1}$) and are classified (in the case of radio-quiet objects; see below for classification of radio-loud sources) as Seyfert 1 galaxies. The optical lines are produced most likely in outflows from the accretion flow in the nucleus. When the inclination is high, so that the nucleus is obscured by a molecular torus, we can observe only narrow lines (hundreds of km s $^{-1}$) and the galaxy is classified as a Seyfert 2 type. Intrinsic X-ray spectra of accretion flows in Seyfert 1s are similar to those of black hole binaries in the hard state. Seyfert galaxies are highly variable in the X-rays (see e.g. Mushotzky, Done & Pounds 1993; Ulrich, Maraschi & Urry 1997), with significant variability on time scales of the order of ~ 1000 s and longer.

A specific class of Seyfert galaxies should be mentioned here, namely Narrow Line Seyfert 1 galaxies. In their spectra a strong soft X-ray excess (which peaks at

energies < 1 keV) is observed (e.g. Puchnarewicz et al. 2001). Narrow Line Seyfert 1s might constitute a counterpart of soft-state black hole binaries, which hypothesis is, however, still subject to many uncertainties. In particular, the variability of Narrow Line Seyfert 1s is much stronger than that observed in the soft state of BHBs at corresponding time scales.

A fraction of AGNs is radio loud, and their radio emission comes from jets and in particular radio lobes (at distances from the nucleus exceeding $\sim 10^8$ pc), where the jets dissipate their kinetic energy. The jets are relativistic, at velocities approaching the speed of light in some objects. Radio loud counterparts of Seyfert 1 and 2 galaxies are named, respectively, Broad and Narrow Line Radio Galaxies. There is a special case, when a radio galaxy is observed almost face-on, so that the Doppler boosted emission from the jet dominates the whole spectrum – such objects are classified as blazars. Their spectra are composed of two distinct features – the first one is produced by synchrotron emission in the jet and peaks in the infrared to soft X-ray range, while the second results from Compton processes in the same plasma and peaks in the γ -rays, with emission extending up to MeV or TeV range.

Also low-luminosity AGNs are observed, in which objects the accretion rate onto the central black hole is most likely very small (e.g. in some LINERs, or Low Ionization Nuclear Emission line Region objects). It has to be noted that in some low-luminosity AGNs the X-ray activity of a galaxy is due to starburst activity.

1.3 Accretion flow models

As we can see from the observational characteristics of accreting black holes presented above, the following goals have to be achieved in modelling of accretion flows:

- Modelling the structure and emission spectra of two distinct phases of an accretion flow – one optically thick and cold (where blackbody-like emission and X-ray reflection are produced) and the other optically thin and hot, where Comptonization spectrum originates. This should encompass the processes governing the accretion, dynamics and physical parameters of the accretion flow, its geometry, interaction between the two phases and modelling the relevant radiative processes.
- The above models have to be applicable in a wide range of luminosities (or accretion rates), from substantially sub-Eddington to super-Eddington ones.
- Explaining the observed short- and long-time variability of accretion flows. By short-time variability we mean the one at time scales corresponding to changes in the accretion flow where most of the gravitational energy is liberated. These

time scales are short compared to those connected with changes occurring in the outer regions of the disc and related to the rate at which matter is delivered to the accretion disc.

- Explaining mechanisms leading to production of outflows in accretion flows on one hand, and their collimation and acceleration to ultra-relativistic velocities on the other.
- Finally, the above goals should be carried out taking into account relativistic effects and possibly the role of the spin of the black hole.

Below in our introduction to accretion flow models we concentrate on the first two of the tasks listed above, as they are the most relevant for the subject of this Thesis.

1.3.1 Basic concepts

Let us assume a gas cloud orbiting a black hole (or any other body) at Keplerian orbits. Then, nearby gas layers would have different orbital velocities and, as a result, friction (e.g. due to viscosity though it seems that magnetic fields are involved in this process, see Section 1.5.2) is expected to appear. This would then lead particles to lose part of their potential energy (which can be later radiated) and settle on lower orbits, while their angular momentum would be transported outwards. As a result, accretion of mass onto the black hole would take place. Historically, the idea of viscous accretion discs was first proposed by Lynden-Bell (1969).

In the relativistic case of accretion onto a black hole, dissipation of energy can take place most likely only down to the marginally stable orbit, below which no stable orbits exists. For a non-rotating (Schwarzschild) black hole, this orbit is located at $6R_g$, where by R_g we denote the gravitational radius, $R_g = GM/c^2$, in which expression G stands for the gravitational constant and c is the velocity of light.

We can easily estimate the efficiency of energy production in an accretion flow using Newtonian approximation. If gas rotation remains Keplerian down to the marginally stable orbit, then the liberated energy per unit mass equals

$$E_{\text{lib}} = \frac{GM}{12R_g} = \frac{c^2}{12}, \quad (1.2)$$

i.e. approximately 8 per cent of the rest mass of the accreting gas is converted to energy and can be in principle radiated. This classical approximation remains in good agreement with the results of relativistic theory, which predicts the efficiency of ≈ 6 per cent for non-rotating black holes. However, the efficiency can amount to 42 per cent for a rotating (Kerr) black hole.

If the rate at which gas accretes is \dot{M} ,³ the luminosity of an accretion disc around a non-rotating black hole is

$$L \approx 5 \times 10^{45} \frac{\dot{M}}{M_{\odot} \text{ yr}^{-1}} \text{ erg s}^{-1}. \quad (1.3)$$

It is convenient to express the accretion rate in units related to the Eddington luminosity,

$$\dot{m} = \frac{\dot{M} c^2}{L_E}, \quad (1.4)$$

so that when $\dot{m} = 1/0.06$, the luminosity of a Schwarzschild black hole would equal the Eddington one.

1.3.2 Optically thick accretion flows

Shakura-Sunyaev disc

The first complete accretion flow model was proposed by Shakura (1972) but is better known from the subsequent article by Shakura & Sunyaev (1973). A relativistic version was put forward by Novikov & Thorne (1973). In this model it is assumed that gas forms a geometrically thin disc in which it rotates in Keplerian orbits and that the inflow velocity is much smaller than the free-fall one. The viscous torque (or, more precisely, the only non-zero component of the stress tensor, $t_{r\phi}$), responsible for transporting angular momentum outwards (and thus making accretion possible) in this model was assumed to be proportional to the total vertically-averaged pressure in the disc, p_{total} , i.e.

$$t_{r\phi} = \alpha_v p_{\text{total}}, \quad (1.5)$$

where $\alpha_v < 1$ is the so called viscosity parameter. The larger α_v , the more efficient transport of angular momentum outwards, which, at a constant \dot{M} , leads to higher radial velocity of the flow and lower surface density of the disc, Σ .

Interestingly, the liberated energy is not dissipated locally but instead carried out to larger radii and, as a result, the local energy dissipation rate in outer parts of the disc is larger than the local rate of potential energy decrease. The dissipated power, Q_{diss} , is assumed to be immediately radiated away from the disc, i.e.

$$Q_{\text{diss}} = Q_{\text{rad}}, \quad (1.6)$$

³We assume the accretion rate to be constant throughout the accretion flow, which assumption is likely to be violated, as we mention in the discussion on outflows in Section 1.3.3.

where Q_{rad} is the power radiated by the disc. The local flux from unit surface at the radius R is then

$$F(R) = \frac{3GM\dot{M}}{8\pi R^3} \left(1 - \sqrt{\frac{6R_g}{R}}\right). \quad (1.7)$$

At low accretion rates (roughly below a few per cent of the Eddington luminosity for BHs, which value rather weakly depends on α_v) the gas pressure dominates throughout the accretion disc. However, when the accretion rate increases, a radiation pressure-dominated region develops in the inner part of the disc. Then the disc becomes secularly unstable, since in the radiation-dominated zone an increase of local \dot{M} is accompanied by a decrease of Σ (this is because the stress tensor is inversely proportional to the column density) which leads to a disruption of the flow. The disc becomes also thermally unstable, since the heating rate grows faster than the cooling rate at increasing disc height.

Since the Shakura-Sunyaev disc is optically thick, its local radiation spectrum can be roughly approximated as blackbody one (we discuss the Shakura-Sunyaev disc spectrum in more detail in Section 1.4.1). In X-ray binaries it peaks at energies ~ 1 keV, while for AGNs at ~ 10 eV [see equation (1.10) below]. Thus, though the Shakura-Sunyaev model is valid for the accretion rates found in most of these objects, it is unable to explain the observed emission of accreting black holes at energies higher than 10 keV. We will return to this issue below.

Slim discs

With the increasing accretion rate, also the optical depth to absorption, τ , in the disc increases. The distance radiation has to travel until it escapes from the disc is roughly proportional to τ^2 and close to the Eddington rate the radiation escape-time exceeds the time scale of accretion (Jaroszyński, Abramowicz & Paczyński 1980). Then, a part of the produced radiation is *advected* under the black hole horizon, i.e. the energy balance relation (1.6) takes the form

$$Q_{\text{diss}} = Q_{\text{rad}} + Q_{\text{adv}}, \quad (1.8)$$

where Q_{adv} is the part of energy carried below the horizon. As a result, the radiative efficiency of the flow is diminished, compared to the standard one. Accretion flows where advection occurs are often named ADAFs, i.e. Advection Dominated Accretion Flows.

Abramowicz et al. (1988) showed that as a result of advection a new accretion disc solution is possible at moderately super-Eddington accretion rates. The flow is optically thick and the pressure is dominated by radiation. However, because of advection, the flow becomes now stable. Unlike the Shakura-Sunyaev solution, the

disc – so called ‘slim disc’ – is now geometrically thick, with disc height comparable to the radius. Also the rotation of the gas in the disc may be substantially sub-Keplerian, with higher inflow velocity.

The radiation spectrum of a slim disc is more difficult to calculate than in the case of optically thick discs at low accretion rates. If the (a priori unknown) viscosity parameter is $\alpha_v \ll 0.1$, then the spectrum is expected to be blackbody, at a higher temperature than that in the Shakura-Sunyaev disc. However, when $\alpha_v \gtrsim 0.3$, the disc overheats (i.e. the gas temperature exceeds the effective temperature) and the spectrum becomes harder than blackbody emission (Beloborodov 1998).

The behaviour of accretion discs at accretion rates significantly (by a factor of ten or so) exceeding the Eddington rate is still poorly known. It is expected that due to high radiation pressure an outflow may form in the disc.

1.3.3 Optically thin accretion flows

The Shakura-Sunyaev disc is clearly unable of reproducing the hard spectra extending to hundreds of keV and beyond, observed from BHBs and AGNs at moderate accretion rates. For that, the presence of hot ($T_e \sim 10^9$ K), optically thin plasma is required.

Cooling-dominated hot flows

Historically, the first accretion disc model with high-temperature plasma was put forward by Shapiro, Lightman & Eardley (1976). They assumed that the disc was optically thin and allowed for different electron and ion temperatures. The electron temperature was then found to be lower than the temperature of ions, T_i , which remained close to the virial one. This resulted from electron cooling being much more effective than the cooling of ions. Consequently, due to high pressure maintained by hot ions, the disc remained geometrically thick.

Because the disc is optically thin, the electron temperature has to be much higher than in the Shakura-Sunyaev disc, so that equation (1.6) could be satisfied and the equilibrium temperature was found to be $T_e \sim 10^9$ K. At this temperature, absorption optical depth $\tau \ll 1$, and optical depth to scattering [see equation (1.15)] $\tau_T \lesssim 1$, the spectrum is dominated by unsaturated Comptonization and extends to energies beyond ~ 100 keV (we describe Comptonization in more detail in Section 1.4.2), which is what we indeed observe.

Then, if both the hot and cold disc co-existed in an accretion flow, it would in general account for the observed spectra in accreting black holes – both the soft X-ray disc emission and the hard X- and γ -ray power-law spectrum. We present such a geometry in Figure 1.1. An outer cold disc could both provide seed photons for

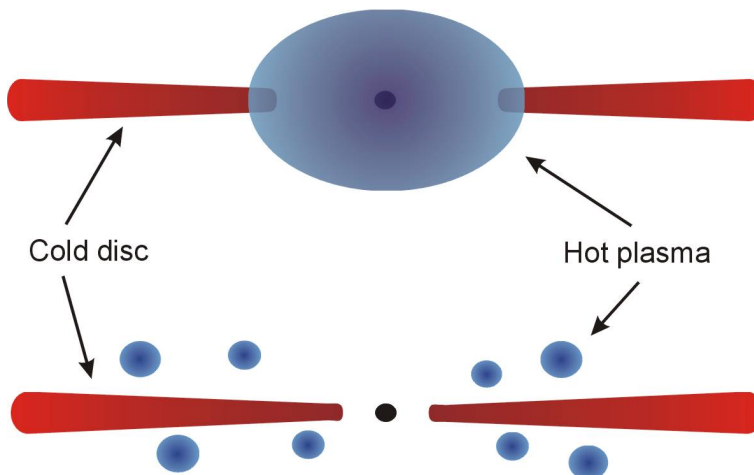


Figure 1.1: Two hypothetical geometries of an accretion flow onto a black hole. The upper figure corresponds to a cold disc disrupted at a distance from a black hole and replaced by a hot, optically thin flow at smaller radii. In the lower figure a cold disc extending down to the marginally stable orbit is shown, while hot, optically thin plasma exists in small active regions above the disc (see Sections 1.3.3 and 1.5.1).

Comptonization (though see remarks in Section 1.5.3) and be the source of X-ray reflection observed in the spectrum. Varying inner radius of the disc could then explain the difference between the soft state (when the cold disc approaches the black hole at the expense of the hot disc) and the hard one, when the cold disc is disrupted far away from the black hole to form the hot flow (Esin, McClintock & Narayan 1997, though they considered advection-dominated flows, see below). This mechanism would also control the amount of reflection and the relativistic effects seen in the spectrum.

The solution of Shapiro et al. (1976) was found by Pringle (1976) to be thermally unstable. This is because with increasing T_i the disc expands, which results in decreased rate of cooling of protons by Coulomb interactions with electrons and leads to thermal runaway.

Advection-dominated hot flows

It was noticed by Ichimaru (1997) that the hot, optically thin accretion flow can be also stabilized by advection, as in the case of slim discs. Here, however, the mechanism of advection is different and requires that all the dissipated energy be delivered to protons, not electrons.

Advection then appears at sufficiently low accretion rates,

$$\dot{m} < 10\alpha_v^2, \quad (1.9)$$

when the Coulomb cooling time scale of protons becomes longer, than the time scale of accretion. Then, only a fraction of the dissipated energy is transferred to electrons and radiated away ($Q_{\text{rad}}/Q_{\text{diss}} \lesssim 1$ for the maximum allowed accretion rates and this ratio becomes orders of magnitude smaller for lower accretion rates). An approximate analytical description of the process was given by Narayan & Yi (1994), and then more detailed analyses of the model followed (e.g. Abramowicz et al. 1996; Chen, Abramowicz & Lasota 1997).

It has to be noted, however, that the validity of the assumption that only protons are heated in the flow has been criticized. Though heating of electrons by adiabatic compression can be usually neglected, electrons may be directly accelerated by e.g. MHD instabilities or magnetic field reconnection (Bisnovatyi-Kogan & Lovelace 1997; Quataert & Gruzinov 1999; see also a discussion in Section 1.5.2). ADAFs can be also convectively unstable (see below).

Originally, advection-dominated flows were introduced to explain the low luminosity of the Galactic centre, Sgr A* and other low-luminosity AGNs, where at the predicted accretion rates (which are however subject to large uncertainties) the luminosity of the standard accretion flow should be orders of magnitude larger than that observed. In the case of Sgr A* recent *Chandra* high spatial resolution observations showed that its actual luminosity was two orders of magnitude lower than that estimated earlier by other missions (Baganoff et al. 2001a) and used as a support for ADAF models. On the other hand, Sgr A* luminosity was found to increase by a factor of ~ 100 during an X-ray outburst (Baganoff et al. 2001b), the time scale of which was consistent with the dynamical time scale close to the central black hole. It would be therefore possible to explain the behaviour of Sgr A* in terms of an accretion rate much smaller than that estimated and highly variable.

ADAF solutions were also used for explaining emission from transient BHBs in the quiescent state (Narayan, McClintock & Yi 1996). In this case, the advantage of ADAFs, with respect to the hot disc solution of Shapiro et al. (1976) is their stability. In general, from the point of view of radiative processes, an optically thin ADAF resembles the cooling-dominated solution of Shapiro et al. (1976), with the main difference that the maximum luminosity is now constrained by the criterion (1.9). Thus, provided that $\alpha_v \gtrsim 0.3$, advective discs could be used also for modelling emission of accreting black holes in their hard states.

Coronal models

Soon after models of hot, optically thin discs were developed, it has been proposed that the hard X-ray emission of accreting black holes can be produced not in a hot accretion flow, but instead in a hot corona above a cold disc (e.g. Bisnovatyi-Kogan & Blinnikov 1977). Its physical parameters would be similar to those of the hot flow

solutions presented above. The corona could be formed e.g. by evaporation of the cold disc. The energy required to heat the coronal plasma would be then delivered by reconnection of magnetic field loops (Galeev, Rosner & Vaiana 1979; Haardt, Maraschi & Ghisellini 1994).

In the coronal model the disc may extend down to the innermost stable orbit and the difference between the soft and hard state is explained by most of the energy being dissipated in the disc or the corona, respectively. The amount of reflection is controlled by the covering factor of the disc by the corona and the disc ionization (see also a discussion in Section 1.5.1). We present the coronal geometry of an accretion flow in Figure 1.1

It has been also proposed (Witt, Czerny & Życki 1997) that the corona itself can be accreting and thus radiate internally dissipated energy, which solution is similar to the hot flow. The transition from the cold disc to the accreting corona (and/or the hot flow) would be controlled by the cold disc evaporation (Róžańska & Czerny 2000).

Outflows

Narayan & Yi (1994) noticed that the Bernoulli constant of gas in an accretion flow may be positive, so that gas particles are not bound to the black hole and outflows are possible. This is in fact a consequence of the viscous angular momentum transport, when the energy is transported outwards before it gets dissipated, which was already found in the Shakura-Sunyaev flow.

In an accretion disc with an outflow, even in the stationary state, \dot{M} will be no longer constant along the radius, but it will decrease with decreasing radius. As a result, the luminosity of an accretion disc can be substantially lower than that predicted from the value of \dot{M} at the outer radius, which effect is similar to the one produced by advection. This possibility was explored in detail by Blandford & Begelman (1999) who called their solutions with outflows ADIOS, i.e. Advection Dominated Inflow-Outflow Solutions.⁴

A similar conclusion was reached by Igumenshchev & Abramowicz (1999) who found ADAFs to be convectively unstable under certain conditions. In a Convection Dominated Accretion Flow (CDAF) the local accretion rate is also decreasing with decreasing radius as a result of outflows. Recently Abramowicz et al. (2002) found that an ADAF is expected to form in the inner part of the accretion flow, while the outer part would correspond to the CDAF solution. The transition radius for black holes of typical hard-state luminosities would be at tens R_g , while it would increase to thousands R_g for low-luminosity sources, which is in agreement with observations.

⁴This was of course supposed to mean ‘Adios ADAFs’.

In fact, outflows appear to be a common feature of accretion flows, e.g. during star formation most of the accreting matter is ejected. Also the broad emission lines in optical spectra of AGNs are attributed to the presence of a wind from the accretion disc. Another phenomenon likely to be related to outflows are collimated, relativistic jets observed both in BHBs and AGNs.

1.4 Radiative processes

Having introduced in the two previous Sections observational properties of black holes and main features of the accretion flow models, we now present in more detail appropriate radiative processes in the frame of the results presented above. We review here the optically thick disc emission, Compton scattering and X-ray reflection. Synchrotron emission is not discussed here, since this process is investigated in detail throughout the Thesis.

1.4.1 Optically thick disc emission

As it was mentioned above, the spectrum of a Shakura-Sunyaev disc is, in the first approximation, a superposition of blackbody spectra of different temperatures and is often referred to as multicolour disc spectrum. The local effective temperature is, from equation (1.7) and Wien's law:

$$T_{\text{eff}}(R) = \left[\frac{3GM\dot{M}}{8\pi a R^3} \left(1 - \sqrt{\frac{6R_g}{R}} \right) \right]^{1/4} \text{ K}, \quad (1.10)$$

where a is Stefan-Boltzmann's constant. Note that at the constant dimensionless \dot{m} and constant radius expressed in R_g , the mass dependence is roughly $T_{\text{eff}} \propto M^{-1/4}$, since then both R_g and \dot{M} scale linearly with M .

As a result, the spectrum has the Rayleigh-Jeans form in the region corresponding to emission from the outer parts of the disc. At higher frequencies the spectrum of a Shakura-Sunyaev disc is a power-law $\sim \nu^{1/3}$ (where ν is the emission frequency), and is produced by peaks of blackbody spectra of different temperatures. Finally there is a cut-off in the spectrum corresponding to the cut-off in the Planck spectrum produced at the inner disc boundary.

The true spectrum of the disc can be modified in a number of ways. First, the dissipation rate as a function of radius can be different than that assumed in the Shakura-Sunyaev model and also the disc is most likely irradiated, which will result in different emissivity and temperature profile. These effects will primarily change the $\nu^{1/3}$ shape of the spectrum.

Second, relativistic effects can modify the spectrum in two ways (e.g. Gierliński 2000). At high inclinations (i.e. when the disc is observed edge-on), the disc spectrum will become softer due to relativistic bending effects. Besides, if the black hole is rapidly rotating, the inner disc radius will decrease which is expected to result in higher temperature and thus higher energy of the cut-off.

The original disc spectrum could be also modified because of Comptonization effects in a boundary layer between the disc and the corona (e.g. Di Salvo et al. 2001). We check this effect in our spectral fits in Section 2.3.1.

1.4.2 Comptonization

Basic concepts

Electrons and photons can exchange energy in the process of Compton scattering. Let m_e be the mass of the electron, γ – its Lorentz factor, ν – photon frequency, and h – Planck’s constant. Then, as long as the photon energy in the electron rest frame is much smaller than the rest mass of the latter, i.e.

$$\gamma h\nu \ll m_e c^2, \quad (1.11)$$

the scattering is elastic, i.e. photon energy does not change in the electron rest frame during interaction. Such a process is called Thomson scattering and can be described classically, as an interaction of an electromagnetic wave with a massive charge.

On the other hand, when the above condition is not fulfilled, the scattering is no longer elastic (since electron recoil becomes important) and also quantum effects have to be taken into account, which case is named the Klein-Nishina regime of Compton scattering. Precise modelling of accreting black holes spectra requires accounting for these effects, as those spectra extend to hundreds of keV at the electron temperature $\lesssim 100$ keV, when the condition (1.11) is violated. However, we can introduce the main ideas and intuitions here, using approximations appropriate for the Thomson regime.

The cross-section for the Thomson scattering is (e.g. Rybicki & Lightman 1979)

$$\sigma_T = \frac{8\pi}{3} r_e^2, \quad r_e = \frac{e^2}{m_e c^2}, \quad (1.12)$$

where r_e is the electron classical radius and e represents the charge of the electron.

Though the scattering is elastic, in the observer’s frame the energies of both particles change, because of Doppler effect. Depending on ν , γ and the angle between photon and electron velocities, either of the particles can gain energy at the expense of the other.

Thermal Comptonization

Before we move on to the more interesting (from the point of view of investigations of accreting black holes spectra) case of energy gain by photons, let us consider one particularly interesting case when photons can lose energy. For a thermal, non-relativistic electron plasma and an isotropic radiation field, F_ν , the equilibrium temperature at which there is no net energy exchange between electrons and photons is called the Compton temperature and is calculated to be

$$T_C = \frac{\int h\nu F_\nu d\nu}{4k \int F_\nu d\nu} \quad \text{K}, \quad (1.13)$$

and is thus related to the mean energy of photons in the spectrum. In particular the fact that the Compton temperature corresponding to cold accretion disc emission is at most $\sim 10^7$ K, while the observed spectra indicate the hot plasma temperature of $\sim 10^9$ K, shows that some form of energy dissipation must take place in the optically thin plasma where Compton spectra in accreting black holes are produced.

If the plasma temperature is larger than the Compton one, photons will, on average, gain energy.⁵ E.g. when a photon collides with a relativistic electron, so that $\gamma^2 - 1 \gg h\nu/m_e c^2$, then, on average, the photon energy will be multiplied by a factor of $\sim \gamma^2$ in the observer's frame. In particular in a thermal plasma, the mean amplification factor (i.e. averaged over angle and electron distribution) of a photon energy is

$$A = \begin{cases} 1 + \frac{4kT_e}{m_e c^2}, & \frac{kT_e}{m_e c^2} \ll 1; \\ 1 + \left(\frac{16kT_e}{m_e c^2}\right)^2, & \frac{kT_e}{m_e c^2} \gg 1, \end{cases} \quad (1.14)$$

provided that the initial photon energy is much smaller than kT_e . Below in our discussion we assume that photons undergoing Comptonization always gain energy from electrons.

The spectrum that forms in an electron plasma cloud in the process of Compton scattering depends not only on the initial spectrum of photons and on the temperature of electrons. An important factor is the typical number of scatterings a photon encounters before escaping from the source. This value depends on the Thomson optical depth,

$$\tau_T = n_e \sigma_T R, \quad (1.15)$$

where n_e is the electron number density and R represents the typical source size. For a plasma optically thin to Compton scatterings (i.e. $\tau_T \lesssim 1$) the number of scatterings is $\approx \tau_T$, while it is $\approx \tau_T^2$ for $\tau_T > 1$ and in estimates it is often approximated

⁵This particular case is sometimes named the inverse Compton effect, as opposed to the Compton scatterings in which photons lose their energy.

as $\tau_T + \tau_T^2$. It is then convenient to introduce the Compton parameter, defined with the above approximation as

$$y = (A - 1)(\tau_T + \tau_T^2). \quad (1.16)$$

Then, for $y \ll 1$ the primary spectrum remains almost unaffected by Compton processes. For semi-relativistic temperatures, $y \ll 1$ requires $\tau_T \ll 1$, so that a relatively small fraction ($\sim \tau_T$) of photons undergoes scatterings and it can be assumed that photons undergo scattering only once before escaping from the plasma cloud.

On the other hand, when $y \gg 1$ the Comptonization process saturates and photons enter equilibrium with electrons, which corresponds to the formation of a Wien spectrum. Then, the emerging spectrum depends basically on electron temperature only.

From our point of view the most important case is the one we encounter in the hard X-ray emitting plasmas in luminous accretion flows, i.e. $y \sim 1$. This case is named unsaturated Comptonization. The corresponding spectrum depends both on temperature and optical depth of the plasma, while it is typically only weakly influenced by the shape of the primary spectrum.

In this intermediate case the Comptonization spectrum is a superposition of spectra from subsequent scatterings. If the optical depth is significantly smaller than unity and the temperature is sufficiently high, we should be able to distinguish those profiles in the spectrum – this is the case of predicted spectra from hot, optically thin flows at low luminosities (e.g. ADAFs). On the other hand, when optical depth is sufficiently high ($\tau_T \sim 1$) and the temperature sufficiently low (so that profiles are close to each other), a power-law spectrum is formed, which we in fact observe in luminous accretion flows. The energy index of the power law spectrum, α , (which corresponds to the energy spectrum being proportional to $\nu^{-\alpha}$) decreases with increasing optical depth and plasma temperature. Such a spectrum extends only up to energies corresponding to the thermal energy of electrons, above which photons cannot gain energy any more and a cut-off in the spectrum is formed (the shape of the spectrum is shown in Figure 4.5).

An important effect that can be in principle observed in Comptonization spectra is anisotropy break. If sources of photons undergoing Comptonization are not distributed uniformly throughout the Comptonizing plasma, but are located e.g. at the basis of the disc corona, then photons in the first scattering are directed mostly backwards and, as a result, a dip in the spectrum is formed at the energy corresponding to the first scattering.

We present an analytical approximation to the Comptonization spectrum and luminosity, in the case when a power-law is formed, in Section 3.2.1.

Non-thermal Comptonization

So far we have considered the case of thermal plasma. However, also purely non-thermal electron distributions (typically approximated with power-law distributions, see Section 4.1) can be of interest for astrophysicists. In this case the resulting spectrum depends on the optical depth and on the form of the distribution. We discuss two extreme cases here.

First, if the Thomson optical depth of the plasma is sufficiently large ($\tau_T \gtrsim 1$), then there is little difference between the spectrum resulting from thermal Comptonization and that produced by multiple scatterings off power-law distribution of electrons, provided the mean energy of electrons in both distributions is the same (Ghisellini, Haardt & Fabian 1993). Thus, also in this case a cut-off power law spectrum is formed.

On the other hand, if the electron distribution function is a power-law, but the optical depth of the non-thermal distribution is very small, the Comptonization spectrum is formed by single scatterings of photons. Then, the spectral shape depends on the energy index p of the power-law distribution, and a power-law spectrum is produced with the spectral index

$$\alpha = \frac{p - 1}{2}. \quad (1.17)$$

The latter case is of particular interest for us, as in this Thesis we consider Comptonization in hybrid plasmas (containing both thermal and non-thermal electrons), where optical depth of thermal electrons is ~ 1 , but the one of non-thermal electrons is $\ll 1$ (Section 4.3.1).

1.4.3 X-ray reflection and relativistic effects

As we mentioned in Section 1.2, a Compton reflection component is observed in both BHBs and AGNs. It originates as a result of multiple downscatterings of incident photons (produced in the hot plasma by Compton upscattering of soft photons) in a cold medium, most likely the underlying cold accretion disc (Lightman & White 1988). Though X-ray reflection processes are not investigated in this Thesis, for consistency we present here in short main properties of this phenomenon, since spectral models including reflection are used in Chapter 2.

The reflection produces a hump in the spectrum, observable in the range from ~ 10 to ~ 100 keV. It is cut off at lower energies as a result of atomic absorption and at the high energy end due to energy loss by electrons during scatterings. A prominent dip in the reflected spectrum, at ~ 7 keV, is produced by iron K-shell absorption (see Figure 2.1).

The shape of the reflected spectrum depends in particular on the slope of the incident spectrum and on the ionization state of the reflecting matter. The ionization of the disc is a result of irradiation and it is conveniently measured by the ionization parameter, defined as:

$$\xi = \frac{4\pi F_{\text{ion}}}{n_e} \quad \text{erg s}^{-1} \text{ cm}, \quad (1.18)$$

where F_{ion} is the incident flux in the range from 5 eV to 20 keV and n_e is the electron density in the part of the disc where scattering occurs (Done et al. 1992). In general, the higher ionization, the less prominent reflection features, and at $\xi \gtrsim 10^4 \text{ erg s}^{-1} \text{ cm}$ the reflected spectrum is identical with the incident one (Życki & Czerny 1994).

Accompanying reflection is the fluorescent iron $K\alpha$ line, which equivalent width and energy also depend on the ionization state.⁶ In particular, the energy of the line ranges from 6.4 keV for neutral iron to 7 keV for hydrogen-like iron ions.

If the reflection occurs in a rotating accretion disc close to the black hole, as it is expected, then relativistic effects will influence the reflection spectrum. Specifically, the iron K edge will be smeared and thus less pronounced and the iron line profile will broaden significantly (extending down to $\lesssim 4 \text{ keV}$) and may acquire a characteristic two-peak profile. The basic calculations were performed by Cunningham (1975), see also e.g. Fabian et al. (1989) for calculations of the line profile for a Schwarzschild black hole. The iron $K\alpha$ line observed in a Seyfert galaxy MCG 6-30-15 by the *ASCA* satellite (Tanaka et al. 1995) has been interpreted as relativistically broadened. Wilms et al. (2001) who analyzed data from an *XMM-Newton* observation suggested that the line profile indicated a rapidly rotating black hole, though this results seems doubtful (see also a discussion in Section 1.5.5).

1.5 Unresolved issues

The picture of accretion flows onto black holes, as reviewed in short above, appears to be generally correct. Nevertheless, there is still a number of fundamental questions to be addressed. Below we present the most important of them, paying particular attention to those most relevant to the subject of the Thesis. Unless stated otherwise, we concentrate here on the problems concerning black holes at moderate accretion rates.

⁶Other X-ray iron lines as well as lines from other elements are of little importance, since they are only marginally detected by present instruments.

1.5.1 Geometry of the flow

In spite of a lot of theoretical work, the issue of the geometry of the accretion flow still remains unsolved. This is mainly because obtaining information on the relative position and interaction between the cold and the hot phase requires simultaneous spectral and variability studies, which only recently started to develop, e.g. in the form of Fourier-resolved spectroscopy (e.g. Gilfanov, Churazov & Revnivtsev 2000 and other works by this group). Its applicability is however still limited to the most luminous sources.

Some constraints can be nevertheless obtained from spectral analysis alone, however they are not definite and usually dependent on the model. E.g. simple energy balance calculations show that given the observed spectra, the corona cannot cover the whole disc (Haardt, Maraschi & Ghisellini 1994) which conclusion seems to favour (within the framework of coronal models) the model of small, active regions where reconnection occurs over the model of an accreting corona. However, Rózańska & Czerny (2000) showed that in some cases the accreting corona develops only over a small range of radii which then should not violate the energy balance.

In a Galactic black hole candidate GX 339–4 (observations of which source we analyze in Chapter 2) the original model of active coronal regions can be rejected basing on the observed correlation between the spectral index and reflection strength (Zdziarski et al. 1998; Zdziarski, Lubiński & Smith 1999), while it is well explained by the configuration with the inner hot flow. The coronal model would agree with the observed correlation, if we assumed a moderate vertical motion of the corona (Beloborodov 1999), which might be related to an outflow. However, also the lack of the anisotropy break in the Comptonization spectra poses a problem for coronal models, which was found e.g. by Gierliński et al. (1997) for Cygnus X-1 and which is also the case for GX 339–4.

Also in this Thesis we conclude that coronal models with dissipation of magnetic field are probably unphysical (Section 5.2) while the hot flow model is compatible with our findings.

1.5.2 The role of magnetic fields

Since the accreting gas is highly ionized, we can expect the ambient magnetic field to be frozen in the plasma. It can be then amplified in the flow as a result of magneto-rotational instability, the theory of which was developed by Velikhov (1959) and Chandrasekhar (1960) and then applied to the case of accretion discs by Balbus and Hawley (1991). The same instability effect can transfer the angular momentum outwards, i.e. serve as the viscosity mechanism hidden under the α_v parameter in

the original Shakura & Sunyaev (1973) solution [equation (1.5)]. This mechanism is expected to work in optically thick flows as well as in optically thin ones.

Similarly to the case of the solar corona, as soon as magnetic field pressure density becomes comparable to that in the disc, magnetic field lines are expected to be removed from the disc by buoyant forces. These field lines could then reconnect, dissipating their energy and heating the disc corona. This is the physical mechanism underlying models of small coronal regions we described in Section 1.3.3, though it has to be noted that the dynamo mechanism originally proposed by Galeev et al. (1979) for the amplification of magnetic fields would be too slow to amplify the magnetic field to sufficient strength. For that the magneto-rotational instability seems to be necessary.

On the other hand, Quataert & Gruzinov (1999) found that if magnetic field pressure in an optically thin ADAF were larger than 1 to 20 per cent of the gas pressure, electrons would be preferentially heated and then the ADAF solution would become unphysical (though this result may depend strongly on the model of particle heating assumed). We discuss the mechanisms of electron acceleration in some more detail in Section 4.1.

Thus, the presence of magnetic field seems crucial for the accretion process itself and is also important for the coronal models. So far, however, it was not possible to obtain any observational constraints on magnetic field strength close to a black hole. We present an observational method of obtaining an upper limit on the field strength in optically thin plasmas close to the black hole in Section 5.2.

1.5.3 The source of seed photons

Comptonization in hot, optically thin plasmas is responsible for most of the hard X-ray and γ -ray emission of accreting black holes. Then, however, a question arises about the sources of photons undergoing Comptonization.

A natural candidate here is the multicolour disc emission, which we do see in the soft state of accreting black holes. However, in the hard state we either do not observe the disc component or it is very weak, which may be due to the disc being cut off further away from the black hole than in the soft state. Then its temperature would be lower and as result its emission would be hidden by interstellar absorption, which strongly suppresses the spectrum below 1 keV.

Nevertheless the aforementioned increasing of the reflection strength with the spectral index observed in many sources (Ueda, Ebisawa & Done 1994; Zdziarski et al. 1999; Gilfanov, Churazov & Revnivtsev 1999, 2001) indicates a connection between the cold and hot phase. The most natural interpretation here is that when the cold disc extends further towards the black hole, both the reflection increases (due to

increased reflecting surface) and also the plasma cooling will be more effective since more disc photons will be produced, which should result in softer Comptonization spectrum (i.e. larger spectral index). Thus also in the hard state the data indicate that the cold disc emission is the seed photon source. However, this interpretation of the observed correlation may be model-dependent, since other factors have to be taken into account, e.g. the relative dissipation rate in the cold and hot phases and possible outflows.

There is another factor that should not be overlooked when discussing the seed photon source, and this is magnetic fields. They have to be present in the hot accretion flow to provide viscosity and they are also required by coronal models. Then, synchrotron radiation will be inevitably produced and Comptonized. Most of this Thesis is devoted to the task of assessing the role of Comptonized synchrotron emission in accretion flows.

1.5.4 Electron distribution in the hot plasma

The spectra of accreting black holes in the hard state are produced by Comptonization in a plasma of the Thomson optical depth $\tau_T \gtrsim 1$. In this case, as we stated in Section 1.4.2, under certain conditions it may be difficult to distinguish observationally between the thermal and non-thermal electron distribution.

On the theoretical ground it is expected that when a non-thermal distribution is created (e.g. by acceleration of electrons by plasma instabilities in the flow or reconnection events) it should be rapidly thermalized, in the first place by synchrotron and Compton processes and only a non-thermal tail beyond the thermal distribution peak will persist (see Ghisellini, Haardt & Svensson 1998 and references therein), which distribution we describe as hybrid in this Thesis. We discuss these mechanisms in more detail in Section 4.1.

The observed γ -ray spectra revealed the presence of non-thermal tails in the hard state of Cygnus X-1 (Section 5.2) and we also speculate on such a possibility in GX 339-4 (Section 2.3.1), though the present quality of data does not allow for precise determination of the electron distribution function. We note that in the soft state we certainly observe a non-thermal component in the plasma distribution.

Obtaining definite answer to the question of to what extent the plasma is thermal in the hard state will require instruments of much higher sensitivity than COMPTEL and OSSE, which provided us with presently available constraints. Solving this problem will not only deepen our understanding of dissipation processes of accretion flows. Distinguishing between thermal and hybrid distributions can also more directly influence the models of accretion flows, due to the strong dependence

of synchrotron emission on the shape of the distribution, which we investigate in Chapter 4.

1.5.5 Other issues

For completeness, we mention here two other questions of primary importance concerning accreting black holes which should be addressed but are not directly connected with the subject of this Thesis.

Jets

Astrophysicists are still lacking of a definite model explaining the production of outflows and in particular their collimation to form ultra-relativistic jets. The primary question is whether these phenomena are connected with the spinning black hole or with the accretion flow. If the former is the case, then the candidate mechanism is the Blandford-Znajek process (Blandford & Znajek 1977) of extraction energy from the black hole through magnetic fields. On the other hand until recently models assuming jet production in the disc required rather unrealistic poloidal magnetic field configurations (Blandford & Payne 1982) but it was proposed that tangled magnetic field in the disc can be responsible for this phenomenon (Heinz & Begelman 2000).

Relativistic effects

The information about relativistic effects in accretion flows comes first from the shape of the iron $K\alpha$ line and in particular there were attempts to estimate the black hole spin from the line profile (e.g. Iwasawa et al. 1996). However, since line emission comes from a range of radii (of different physical conditions), and the exact shape of the underlying continuum is not known precisely enough, these results are far from being reliable. Reverberation techniques, investigating the disc reflection response to X-ray flares (Reynolds et al. 1999), may bring more definite answers, as soon as better data are provided by future missions.

The problem of $K\alpha$ line profile is particularly interesting not only as one of the most direct potential evidences for the existence of black holes. Since the line shape depends also on the spin of the black hole, the simultaneous presence (or the lack of it) of relativistic jets and a line profile indicative of a rapidly spinning black hole might answer the question if the spin of the black hole is responsible for jet production.

Chapter 2

GX 339–4 observations

In the previous Chapter the main theoretical and observational results concerning accreting black holes have been sketched and we paid particular attention to the results describing the hard state of Galactic black holes. Below a specific case of a black hole candidate in a low-mass X-ray binary and in its hard state, GX 339–4, is investigated. We use X- and γ -ray observations of this source to constrain the parameters of the radiating plasma in the accretion flow. We also analyze energy-dependent short-time variability of the source. These results allow us for drawing conclusions on the nature of the flow and then are used in Chapter 5 for obtaining constraints on the synchrotron emission and its Comptonization.

2.1 The black hole candidate GX 339–4

GX 339–4 is an X-ray source, discovered by the *OSO-7* satellite (Markert et al. 1973). It exhibits state transitions typical for accreting black holes in X-ray binaries.

Detailed spectral analyses can be found in e.g. Ueda et al. (1994), Zdziarski et al. (1998), Wilms et al. (1999) and Kong et al. (2000). X-ray variability studies were done by e.g. Maejima et al. (1984), Smith & Liang (1999) and Revnivtsev, Gilfanov & Churazov (2001). Also γ -ray observations by OSSE (Grabelsky 1995; Zdziarski et al. 1998; Smith et al. 1999) and SIGMA (Bouchet et al. 1993; Trudolyubov et al. 1998) were taken.

The source has been also observed in the radio band (Fender et al. 1999 and references therein) when an extended emission from a jet-like elongated structure was reported (Fender et al. 1997). Optical observations (e.g. Grindlay 1979; Motch et al. 1982, 1983; Soria, Wu & Johnston 1999) did not constrain the nature of the companion star. Most likely the observed optical radiation is produced in the accretion flow or in an outflow and not in the star. This is supported by the weakening of the optical emission during a transition from hard to soft X-ray state (Motch et

al. 1983, Makishima et al. 1986). A similar weakening during transition to the soft state has been observed in γ -rays and in the radio emission, see Corbel et al. (2000).

GX 339–4 is most likely an accreting black hole. It is suggested by its PDS having the same characteristics as those of other black hole candidates (Sunyaev & Revnivtsev 2000; see Section 1.2.1). Also, GX 339–4 energy spectra are remarkably similar to those of a widely studied X-ray binary with a black hole, Cygnus X-1 (e.g. Tanaka & Lewin 1995). It is also worth mentioning that the hard state spectrum of GX 339–4 closely resembles that of an AGN, NGC 4151 (Zdziarski et al. 1998). Besides, the relation between X-ray and optical variability is similar to that in an accreting black hole J1118+480 (Section 5.3). However, no reliable measurements of the mass of the compact object exist.

GX 339–4 is a prototypical black hole candidate in an X-ray binary system, investigations of which may provide insight into nature of other similar sources. The uniqueness of this object lies in the optical emission, which most likely originates in the accretion flow, unlike other X-ray binaries, where the star dominates in the optical range (the only other object like that is the aforementioned accreting black hole J1118+480). This allows for studying the relation between the X-ray (Comptonization) and optical (possibly synchrotron) spectrum, which we perform in Section 5.3 further in this Thesis.

2.2 Data selection and reduction

We analyzed five observations of GX 339–4 by *Ginga* and *RXTE* satellites, which were simultaneous (or almost simultaneous) with γ -ray observations by OSSE detector onboard *CGRO*. This provided us with data in the useful range from a few keV to a few hundred keV. During four observations the source was found to be in its hard state, while in the fifth one it exhibited behaviour typical for the off state of this source.

The first two of our datasets are identical with those used by Zdziarski et al. (1998). They consist of *Ginga* data from September 11 and 12, 1991 (see Table 2.1), with useful range of energies of 1.2–29 keV and simultaneous OSSE data in the range 50 – 1000 keV. We added 1 per cent systematic error to the *Ginga* data. This value results from fits to Crab nebula spectrum, which is expected to have no features and should be satisfactorily fitted with a power-law model (K. Ebisawa, private communication). We also added energy-dependent systematic errors, corresponding to an uncertainty in the detector effective area, to the OSSE data in all datasets. These errors amount to ~ 3 per cent at 50 keV and decrease to ~ 0.3 per cent at energies $\gtrsim 150$ keV.

Table 2.1: A summary of observational data we use. The (background subtracted) count rates for LAC, PCA, HEXTE and OSSE instruments are for 1.2–29, 3–30, 30–100 and 50–1000 keV energy ranges, respectively.

No.	Satellite	Date	Instrument	Exposure [s]	Counts [s^{-1}]	References
1	<i>Ginga</i>	1991 Sept. 11	LAC	2.0×10^3	1720	Ueda et al. (1994), Grabelsky et al. (1995)
	<i>CGRO</i>	1991 Sept. 11	OSSE	4.8×10^3	15	Zdziarski et al. (1998)
2	<i>Ginga</i>	1991 Sept. 12	LAC	3.8×10^2	1700	Ueda et al. (1994), Grabelsky et al. (1995)
	<i>CGRO</i>	1991 Sept. 12	OSSE	2.5×10^3	15	Zdziarski et al. (1998)
3	<i>RXTE</i>	1996 Jul. 26	PCA	5.2×10^3	271	Böttcher, Liang & Smith (1998),
			HEXTE	1.7×10^3	29	Smith & Liang (1999), Smith et al. (1999)
	<i>CGRO</i>	1996 Jul. 9–23	OSSE	5.4×10^5	6.5	
4	<i>RXTE</i>	1997 Feb. 14	PCA	2.1×10^4	217	Revnivtsev et al. (2001)
			HEXTE	6.6×10^3	26	
	<i>CGRO</i>	1997 Feb. 11–19	OSSE	3.4×10^5	7.0	
5	<i>RXTE</i>	1999 Jul 7	PCA	1.2×10^4	1.5	
	<i>CGRO</i>	1999 Jul 6–13	OSSE	1.1×10^5	0.2	

In the third dataset we used a relatively short *RXTE* observation from July 26, 1996 which was performed after a two-week long OSSE observation of the source, lasting from July 9 to 23. The latter spans thus a much larger amount of time than the *RXTE* observation. This is, however, necessary so as to obtain the signal-to-noise ratio good enough for precise measurement of the plasma temperature.

We extracted *RXTE* data from the Proportional Counter Array (PCA) instrument, units 0 and 1, as the two detectors are expected to have the best calibration (C. Done, private communication). We used data from Layer 1 only, which provides the highest signal-to-noise ratio. A systematic error of 0.5 per cent has been added to PCA data, again based on the fits to Crab spectra, see a discussion in Wilson & Done (2001). We used the PCA data in the range 3 – 30 keV, which is a rather conservative choice of energies. Also data from the HEXTE detector (cluster 0) were used, in the range 30 – 100 keV. Finally, for the OSSE data we use the energy range of 50 – 1000 keV.

The fourth dataset consists of an *RXTE* observation from February 14, 1997 and an OSSE observation which lasted from February 11 to 19, 1997. These data have the best statistics among all the observations we analyze. The data reduction procedures were identical as above.

Finally, in the fifth dataset an *RXTE* observation from July 7, 1999 is used along with a two-week OSSE observation, which lasted from July 6 to 13. In the PCA range, the source was by two orders of magnitude fainter than in other datasets. Thus, in order to obtain the best signal to noise ratio, in the PCA data analysis we used Layer-1 counts from all detector units available during this observation, i.e. 0, 2 and 3. In this case 1 per cent systematic error has been added. Again, OSSE data have been used, in the range 50 – 1000 keV. We did not use HEXTE data here because of poor statistics.

2.3 Spectral models

All our fits below are performed with the *XSPEC* package (Arnaud 1996) version 11.0.1. The confidence ranges for model parameters below are given for a 90 per cent confidence interval, i.e. $\Delta\chi^2 = 2.7$ (e.g. Press et al. 1992). The plotted vertical error bars are 1σ , while the upper limits are 2σ . The data in the plots have been rebinned for clarity of the display.

We fit the data with the *CompPS* model of Poutanen & Svensson (1996), which calculates iteratively the spectrum resulting from Comptonization of soft photons in an optically thin hybrid plasma and its reflection from an ionized, optically thick medium, presumably a cold accretion disk. We also take into account the effect of

absorption. The abundances of the reflector and the interstellar medium are from Anders & Ebihara (1982).

The model thus reproduces three distinctive components of the spectrum. The first one is the spectrum of seed photons undergoing Comptonization, which can be either of the form of a blackbody spectrum (which we choose) or multicolour disc blackbody (see Section 1.4.1).

The second one is the Comptonization continuum, produced by scattering of the soft photons off electrons in optically thin plasmas (main features of Comptonization are discussed in Section 1.4.2, while an analytical approximation to the shape of Comptonization spectrum and its luminosity is introduced in Section 3.2.1).

Finally, the third component in the model represents X-ray reflection of the Comptonization spectrum off cold ($T_e \sim 10^6$ K), optically thick matter. Main features of the reflection from accretion disc were reviewed in Section 1.4.3.

The model of the *thermal* Comptonized emission is parameterized by plasma Thomson optical depth, τ_T , its temperature, kT_e , and the temperature of blackbody soft photons entering Comptonization, kT_{seed} . We also consider Comptonization by a hybrid electron distribution, which consists of a Maxwellian part up to an electron Lorentz factor γ_{nth} and above of a power-law of energy index p , which is cut off at the Lorentz factor γ_f (physical mechanisms leading to formation of such a distribution are discussed in Section 4.1).

The reflection is parameterized by the ratio $\Omega/2\pi$, where Ω is the angle subtended by the reflector, relative to an isotropic source of X-rays located above the reflector. In particular, $\Omega/2\pi = 1$ would correspond to a point-like isotropic source above an infinite disc. This is a conventional method of normalizing the strength of reflection relative to the observed Comptonization continuum and in general, values of $\Omega/2\pi > 1$ are possible (e.g. when the source of primary Comptonization spectrum is obscured or the irradiating flux is not isotropic).

In our fits we allow for free ionization parameter of the reflector, ξ [defined in equation (1.18)] and free iron abundance relative to solar, A_{Fe} . Gravitational effects on the shape of the reflected continuum and the profile of the iron $K\alpha$ line have been taken into account self-consistently, assuming a Schwarzschild black hole. The general relativistic correction for the reflected component was calculated within the *CompPS* model while for the line we used the *diskline* model (Fabian et al. 1989), both of which were parameterized by the inner disc radius, r_{in} , expressed in the units of R_g .

We assume neutral hydrogen column density $N_{\text{H}} = 6 \times 10^{21} \text{ cm}^{-2}$. This value was derived from $E(B - V)$ measurements and remains consistent with results of other methods, see Zdziarski et al. (1998) and references therein. Also following Zdziarski et al. (1998) we assume the distance to the source $d = 4 \text{ kpc}$ (which is a

kinematic one and agrees with extinction measurements) and the inclination of the binary $i = 45^\circ$, which value is however unconstrained.

2.3.1 Hard state observations

The source flux (extrapolated to the range 1–1000 keV) in datasets 1 to 4 is of the order of 10^{-9} erg cm $^{-2}$ s $^{-1}$, which, at the assumed distance, corresponds to the source luminosity (again in the range 1–1000 keV) of $L \sim 1 - 3 \times 10^{37}$ erg s $^{-1}$. For a stellar-mass black hole this corresponds to a few per cent of the Eddington luminosity.

Thermal fits to *Ginga*/OSSE data

We first fitted *Ginga* and OSSE data, i.e. datasets 1 and 2 (fits 1 and 2, respectively, in Table 2.2). The data in the former set have much better statistic and we hereafter confine our discussion to that set, unless stated otherwise. The plasma was assumed to be purely thermal. As was shown by Zdziarski (1998, see a discussion in their section 5.1), spectral fits to the *Ginga* and OSSE data do not allow for constraining the geometry of the Comptonizing cloud and soft photon sources. Thus, we assumed tentatively the geometry of a spherical plasma cloud with soft photon sources distributed uniformly. We also introduced the soft excess in the form of a blackbody of the same temperature as that of the seed photons (see below).

For all fits presented in Section 2.3.1 below we additionally calculated values of the power-law spectral index, α , of the primary Comptonization continuum. We obtained these values in a manner consistent with the results of *CompPS* fits – namely, they were obtained by fitting a power-law model to 4 – 20 keV data, which had been artificially generated from our *CompPS* fits with reflection, iron line and soft excess components suppressed.

We found that the best fit for dataset 1 was good, with $\chi^2 = 46$ for 80 degrees of freedom (hereafter d.o.f.). The reduced χ^2 , 46/80, is much lower than unity here which results from relatively large systematic errors. Figure 2.1 shows separate components of the fitted spectrum, while spectra from different datasets are compared in Figure 2.2. The fit parameters are very similar to those obtained by Zdziarski et al. (1998) and indicative of a typical hard state spectrum (this is also the case for the fit to dataset 2). The main difference from the results presented by Zdziarski et al. (1998) in their table 2 is the plasma temperature, which we fit at $kT_e = 46$ keV, while Zdziarski et al. (1998) obtained $kT_e = 57$ keV. This discrepancy results from the fact that the model we use, *CompPS*, more precisely determines the shape of the thermal cut-off than the *thComp* model used by Zdziarski et al. (1998). See

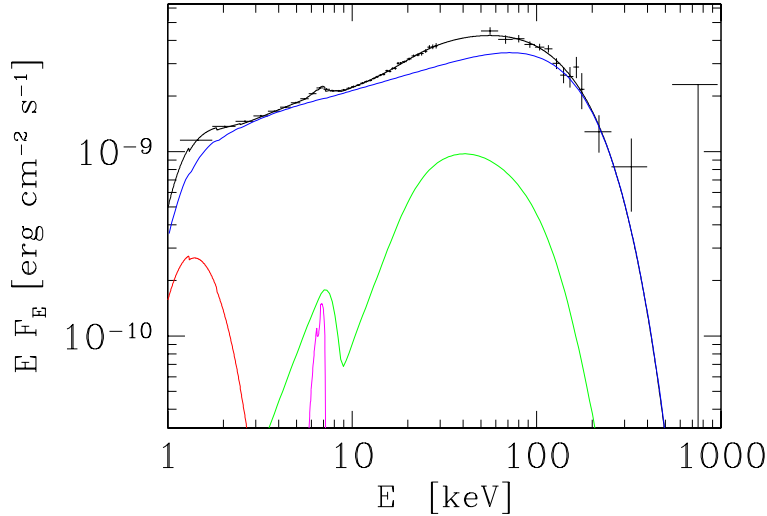


Figure 2.1: Spectrum of the *Ginga* and OSSE observation (dataset 1). The fitted model is represented by the black curve. Also, the separate components of the model are shown: Comptonization of blackbody photons (blue), soft excess (red), reflection from a cold disc (green) and the iron line (magenta). At energies below a few keV the shape of the spectrum is affected by absorption.

also section 5.1 in Zdziarski et al. (1998) where the values of kT_e obtained from fits with the *CompPS* model are presented.

For both datasets the fitted relative normalization of OSSE to *Ginga* was close to unity (0.91 and 0.90 for datasets 1 and 2, respectively). For this and for all subsequent fits, in Table 2.2 we give the luminosities obtained from the OSSE data, since for hard state spectra most of the luminosity is produced in the OSSE energy range. Such a choice is also more appropriate for investigating the connection between luminosity and plasma temperature (see Section 2.3.3), since both are derived almost exclusively from OSSE data.

The main reason for the lack of solid constraints on the geometry of the Comptonizing plasma and the source of seed photons is the presence of the soft excess, i.e. excessive soft X-ray emission, compared to that necessary to produce the observed Comptonization spectrum. The excess was earlier observed by Ueda et al. (1994) and Zdziarski et al. (1998). In principle, constraints on the geometry can be obtained from the presence or absence of the anisotropy break, which is expected to appear in non-homogenous geometries, such as a corona above a disc (see Section 1.4.2). However, the energy range where the anisotropy break may be present coincides with that where soft excess is observed.

We checked that for the homogenous, spherical geometry (no anisotropy break) we assumed, the fit to the *Ginga* spectrum without a soft excess was significantly worse, with $\chi^2 = 75/80$ d.o.f. We also checked three other geometries – a sphere with central photon source, a slab and a hemisphere, both with the source of photons at the bottom surface (so that the anisotropy break should develop), where the fits without the excess were even worse. This supports our choice of a spherical geometry with uniform distribution of photons sources.

We also found that the soft excess can be modelled by thermal Comptonization of soft blackbody photons (of the same temperature as those entering Comptonization) in an optically thick plasma of $\tau_T = 6.1$ and $kT_e = 1.4$ keV (we used the model *CompTT* of Titarchuk 1994), which resulted in the value of $\chi^2 = 45/79$ d.o.f. This result is similar to the findings of Di Salvo et al. (2001), who found that the soft excess observed by *BeppoSAX* in the hard state of Cygnus X-1 can be explained by the same model with $kT_e \sim 3$ keV. Another possibility is that the soft excess is produced by Comptonization in an optically thin plasma, with $kT_e = 20$ keV and $\tau_T = 0.43$, which fit returned $\chi^2 = 45/79$ d.o.f. Such a model was applied to another observation of Cygnus X-1 in the hard state by Frontera et al. (2001). Though we confirm the presence of the soft excess independently of the source geometry assumed, the *Ginga* data do not allow for distinguishing between the approaches of Di Salvo et al. (2001) and Frontera et al. (2001).

Hybrid fits to *Ginga*/OSSE data

We have also tested the hypothesis that the Comptonizing plasma is hybrid, with a high-energy power-law tail in the electron distribution. The OSSE data do not allow for constraining the values of p and γ_f . Therefore we assumed $\gamma_f=1000$ and $p = 4$. The latter value is close to the index measured in Cygnus X-1, see Gierliński et al. (1999) and McConnell et al. (2000a) and also allows for direct comparisons with the results of our theoretical investigations of hybrid Comptonized synchrotron emission in Sections 4.2 and 4.3.

We found that adding a non-thermal component for dataset 1 only marginally decreased χ^2 of the best fit (by ~ 0.1), yielding an electron distribution with the ratio of energy carried by non-thermal and thermal electrons, $\delta = 0.03$ [see equation (4.2) where the δ parameter is defined]. The fit is weakly sensitive to the amount of non-thermal electrons and we found that χ^2 increases by 2.7 (which marks the 90 per cent confidence level) when $\delta = 0.34$.

We hereafter use a thermal fit for *Ginga* data but conclude that they are marginally consistent with the presence of a weak, non-thermal tail in the electron distribution. This is favoured by the findings of Zdziarski et al. (1998) who determined the presence of non-thermal electrons at $\delta = 0.05$ from fits to the entire OSSE obser-

Table 2.2: Results of fits to the data, see Section 2.3 for details. Fit numbers correspond to datasets numbers in Table 2.1 (fits 4a and 4b are, respectively, a thermal and a hybrid fit to dataset 4). Temperatures are expressed in keV, L (in the range 1 to 1000 keV) in erg s^{-1} , ξ in erg s^{-1} cm, iron line energy in keV and its equivalent width in eV.

Fit	kT_e	L	τ_T	α	$\Omega/2\pi$	ξ	A_{Fe}	kT_{seed}	E_{Fe}	W_{Fe}	r_{in}	$\chi^2/\text{d.o.f.}$
1	46_{-4}^{+6}	2.5×10^{37}	$2.9_{-0.3}^{+0.3}$	0.75	$0.36_{-0.07}^{+0.07}$	126_{-99}^{+112}	$2.9_{-0.9}^{+1.7}$	$0.25_{-0.03}^{+0.02}$	$6.58_{-0.32}^{+0.32}$	70	$36_{-30}^{+\infty}$	46/81
2	43_{-6}^{+8}	2.3×10^{37}	$2.7_{-0.3}^{+0.4}$	0.73	$0.21_{-0.09}^{+0.09}$	341_{-263}^{+1053}	$1.6_{-0.9}^{+3.6}$	$0.27_{-0.03}^{+0.03}$	$6.58_{-0.32}^{+0.30}$	61	$185_{-179}^{+\infty}$	63/81
3	58_{-3}^{+3}	8.8×10^{36}	$1.9_{-0.1}^{+0.1}$	0.79	$0.40_{-0.06}^{+0.06}$	110_{-37}^{+67}	$3.4_{-1.7}^{+1.0}$	$0.21_{-0.10}^{+0.06}$	$6.28_{-0.14}^{+0.14}$	88	6^{+65}	129/116
4a	75_{-5}^{+5}	1.2×10^{37}	$1.5_{-0.1}^{+0.1}$	0.79	$0.39_{-0.03}^{+0.04}$	92_{-26}^{+29}	$2.8_{-0.6}^{+0.8}$	$0.16_{-0.15}^{+0.05}$	$6.31_{-0.13}^{+0.12}$	60	33_{-27}^{+53}	122/124
4b	48_{-11}^{+10}	1.2×10^{37}	$2.1_{-0.3}^{+0.4}$	0.76	$0.29_{-0.08}^{+0.07}$	273_{-146}^{+417}	$2.4_{-0.7}^{+0.9}$	$0.33_{-0.06}^{+0.04}$	$6.25_{-0.11}^{+0.11}$	103	7_{-1}^{+26}	113/123

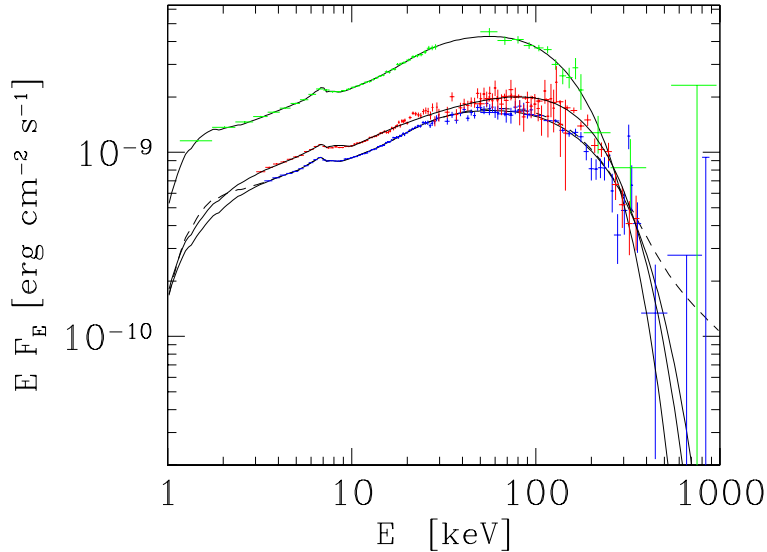


Figure 2.2: Spectra from the *Ginga* and OSSE (dataset 1, green) and *RXTE* and OSSE (dataset 3 — red, dataset 4 — blue) observations. Black, solid lines mark the best thermal fits to the data. The dashed line shows the best hybrid fit to dataset 4.

vation, encompassing much longer time than the *Ginga* data. This may be, however, an effect of the OSSE spectrum evolving in time. We discuss this issue below in this section.

Thermal fits to *RXTE*/OSSE data

For dataset 4 consisting of *RXTE* and OSSE data, we used the same model as for the *Ginga* data, with the exception of the soft excess, which as we have checked cannot be constrained by the *RXTE* data, with its useful range starting at 3 keV. The fit (No. 4a in Table 2.2) is satisfactory, at $\chi^2 = 122/124$ d.o.f. The relative normalization of models to HEXTE and PCA data was 0.76, which is a typical value. On the other hand the relative normalization of models to OSSE and PCA data was again close to unity, 0.99. We thus conclude that the *RXTE* and OSSE spectra match well each other, though the observing time was much longer for the latter instrument (but see a discussion below). The results of our fits are similar to those obtained by Wilms et al. (1999), who analyzed an *RXTE* observation that took place three days after ours.

The same model was applied to dataset 3 but produced a significantly worse fit, at $\chi^2 = 209/117$ d.o.f. However, both OSSE and All-Sky Monitor (ASM) onboard *RXTE* showed that not only the source was variable on time scale of days (which required, as in the case of the fourth dataset, free relative normalization of *RXTE*

and OSSE data) but also OSSE spectrum was becoming systematically softer and brighter during the two-week observation (Smith et al. 1999). Thus either the temperature or the optical depth of the plasma must have been decreasing, at the increasing flux. We accounted for this effect by allowing for different values of τ_T in the fits to *RXTE* and OSSE data. The temperature was kept the same for both instruments, since *RXTE* data alone do not allow for constraining the temperature precisely. We found the best-fit value of τ_T for the OSSE data to be $\tau_T = 2.4$ which is indeed larger than the value for the *RXTE* data, $\tau_T = 1.9$ (fit 3 in Table 2.2), and the overall fit quality was satisfactory, at $\chi^2 = 129/116$ d.o.f. The relative normalization of models to HEXTE and PCA data was 0.78, similar to that in the previous dataset. Normalizations of models to PCA and OSSE data could not be compared directly, because of different values of τ_T . However, the source luminosity, calculated from the model to OSSE data, is 0.67 of the luminosity obtained from the model to PCA data.

We note that because of the softening of the spectrum during the OSSE observation, any conclusions on connection between the temperature and luminosity (derived mostly from OSSE data) and other fit parameters (spectral index and reflection parameters, constrained mainly by *RXTE* data) for dataset 3 should be treated with caution.

Our results are significantly different from those of Smith et al. (1999), who analyzed the same data and concluded that the *RXTE* spectrum above 15 keV and the OSSE spectrum could be modelled with the same power-law component, while found a soft excess at energies $\lesssim 10$ keV (which they modelled by a power-law) and no reflection signatures. This most likely resulted from their fitting procedure in which they used two power-law components of different slopes, one for *RXTE* data below 15 keV and the other for *RXTE* data above 15 keV (where the spectrum hardens due to reflection) and OSSE data. Also Böttcher et al. (1999) reached conclusions similar to those of Smith et al. (1999), basing on the same observation, but using their model of emission from a disc–corona geometry. We are, however, unable to compare directly our results to theirs, because for the latter no fit parameters were given and the model was seemingly fitted by eye to the data unfolded (i.e. translated from observed photon counts to incident photon spectrum) through a power-law model. Such a procedure is incorrect, since in X-ray detectors the shape of the unfolded spectrum depends on the model used for unfolding, which is a consequence of quantum effects.

Hybrid fits to *RXTE*/OSSE data

From datasets 3 and 4 only the latter allows for a search for constraints on the non-thermal electron population. This is because the increasing hardness of the

OSSE spectrum in dataset 3 could mimic to some extent the effect of scattering off non-thermal electrons.

Thus, we fitted the dataset 4 with the same hybrid model as used for the *Ginga* data above. We found that the fit (No. 4b in Table 2.2) was significantly better than the thermal one, with $\chi^2 = 113/123$ d.o.f., at $\gamma_{\text{nth}} = 1.63_{-0.18}^{+0.23}$ and $kT_e = 48_{-10}^{+11}$ keV. This corresponds to the value of $\delta = 0.31_{-0.15}^{+0.23}$, where δ increases at decreasing kT_e and γ_{nth} . The relative normalizations of HEXTE and OSSE data relative to PCA were 0.74 and 0.93, respectively.

Since the OSSE data poorly constrain the non-thermal tail in the Comptonization spectrum for $h\nu \gg kT_e$, most of the information about the non-thermal electron population comes from the shape of the cut-off and potential hardening of the spectrum for $h\nu \lesssim kT_e$. The OSSE observation was much longer than the *RXTE* one. Thus, it is possible that the modification of the shape of the spectrum was due not to the presence of non-thermal electrons, but resulted from variations of the shape of the OSSE spectrum. It is also possible that contribution from regions of different temperatures and/or Thomson optical depths formed the shape of the spectrum deviating from a purely thermal cut-off.

We checked these possibilities. First, we allowed for different values of τ_T for *RXTE* and OSSE data. This, however, did not change the fit quality ($\chi^2 = 121/123$ d.o.f.) and the difference between the fitted values of τ_T was only 0.1. We also fitted two *CompPS* models, allowing for different values of τ_T and kT_e and keeping all other model parameters the same. This significantly improved the fit, compared to a single thermal *CompPS* model, resulting in $\chi^2 = 112/121$ d.o.f., only slightly worse than the hybrid fit. The fitted plasma parameters were $kT_e = 64$ keV and $\tau_T = 1.94$ for one of the *CompPS* models and $kT_e = 73$ keV and $\tau_T = 1.30$ for the other. In fact, plasmas in an accretion flow are expected, on average, to increase its temperature at the decreasing optical depth, as a result of less effective Compton cooling, a behaviour we observed in the two-*CompPS* model fit. Such a result is thus consistent with emission from regions of different temperatures.

We are therefore unable to distinguish between a hybrid electron distribution and a superposition of emission from regions of different temperatures. The former interpretation might be favoured by the fact that the value of δ we obtained is similar to the one derived from the hard state *COMPTEL* observation of Cygnus X-1 (McConnell 2000a), $\delta = 0.22$, see Section 5.2.2.

Reflection features

In all observations above the disc was found to be moderately ionized, with $\xi \gtrsim 100$ erg s⁻¹ cm. In *Ginga* data the iron K α line energy, E_{Fe} , was larger than 6.4 keV, which is expected when the disc is ionized. However in the *RXTE* data, where

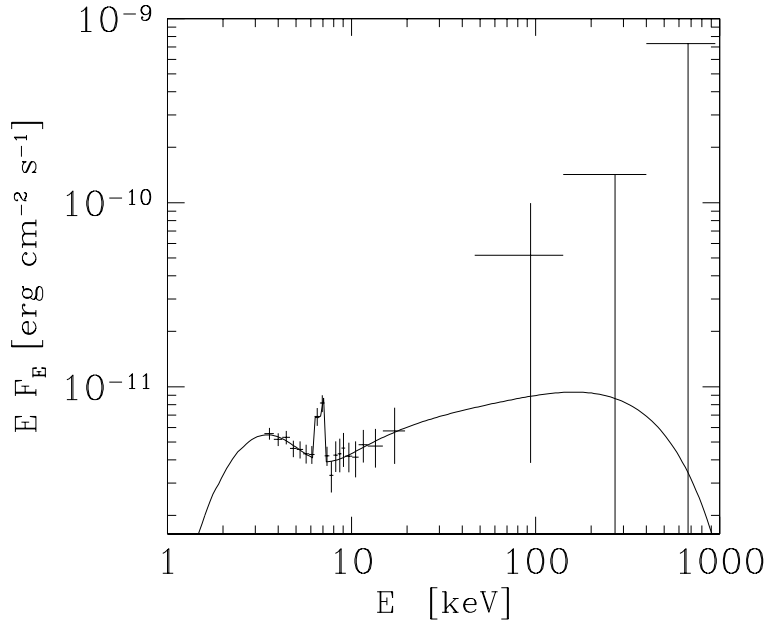


Figure 2.3: The data from dataset 5. The solid curve marks the best *CompPS* model fit to the data.

disc ionization was also high, the line energy dropped below 6.4 keV. Such an effect was also found in other observations of GX 339–4 performed by *RXTE* (Wilms et al. 1999, Feng et al. 2001) and this may indicate an instrumental problem. The equivalent width of the line, $W_{\text{Fe}} \lesssim 100$ eV, for datasets 1 – 4 remains in agreement with the amount of reflection observed.

In all the above fits we included effects of relativistic smearing of the line and reflection components. However, the quality of the *Ginga* data did not allow for constraining the value of the inner disc radius. The fit to dataset 1 produced $r_{\text{in}} = 36_{-30}^{+\infty}$, where the lower value is a constraint resulting from the model and corresponds to the marginally stable orbit around a Schwarzschild black hole. The *RXTE* data allowed for somehow better constraints, with r_{in} in the range from 6 to ~ 100 . This might suggest that relativistic effects are moderately important.

2.3.2 The off state spectrum

During the observation listed as dataset 5 in Table 2.1 the source was ~ 2 orders of magnitude fainter than during observations investigated in Section 2.3.1. At this flux level, GX 339–4 has been classified as being in the off state. For recent results and references see Kong et al. (2000).

We first fitted the data with the same thermal model as for datasets 3 and 4. Due to the low quality of the data we fixed the iron abundance at $A_{\text{Fe}} = 3$, in agreement with previous fits, ionization at $\xi = 0$ and relative normalizations of OSSE to PCA data at unity. We obtained a good fit, at $\chi^2 = 46/64$ d.o.f. It was however impossible to constrain the reflection strength and the plasma temperature – the best fit values were $\Omega/2\pi = 0$ (no error could be estimated) and $kT_e = 170_{-150}^{+230}$ keV. The seed photons temperature could be constrained only as $kT_{\text{seed}} \leq 0.9$ keV. The source luminosity estimated from the model was $L = 8 \times 10^{34}$ erg s $^{-1}$. The iron $K\alpha$ line was very strong in these data, with $E_{\text{Fe}} = 6.8_{-0.6}^{+0.3}$ keV and $W_{\text{Fe}} = 870$ eV, at the best-fit value of $r_{\text{in}} = 150$ (see Figure 2.3, where the spectrum and the fitted model are shown).

The unusually strong iron line has been already reported for the off state of this object by Feng et al. (2001). This result would pose a problem for accretion flow models, which predict that in the off state the cold disc (that could produce the iron line) should be either absent or disrupted very far away from the black hole, thus giving no rise to the iron $K\alpha$ line. Also Nowak, Wilms & Dove (2002) found that the line was too strong, with respect to the observed reflection strength, in the hard state when the luminosity decreased.

However, it has to be remembered that GX 339–4 lies almost in the Galactic plane and in the direction towards the Galactic centre. From the observations of Yamauchi & Koyama (1993) we estimated that the flux in the iron line produced by Galactic diffuse emission at the position of GX 339–4 should be $F \approx 3 \times 10^{-5}$ photons cm $^{-2}$ s $^{-1}$ deg $^{-2}$, while from our fits we obtained $F \approx 4.3 \times 10^{-5}$ photons cm $^{-2}$ s $^{-1}$ deg $^{-2}$. Though in our estimate we could not take into account local fluctuations of the Galactic diffuse emission, this result provides nevertheless a very strong argument that the line flux should be attributed to Galactic diffuse emission.

Apart from explaining the line strength in the off state spectrum, we estimated that taking into account the diffuse Galactic emission could also explain findings of Nowak et al. (2002), i.e. the observed excess in the line equivalent width at low luminosities of the source.

Another characteristic feature in the spectrum is a turnover in the spectrum at a few keV that can be noticed in the EF_E plot (Figure 2.3). Below the turnover the spectrum is soft, while above it hardens substantially. It has to be noted, however, that the hardening may be at least partially due to background subtraction uncertainties. In the discussion below we assume that the aforementioned effect is real.

In the model presented above, the soft spectrum below the turnover would be interpreted as declining blackbody emission at kT_{seed} , while the spectrum above as Comptonization one. However, a rather high energy of seed photons and hard

Comptonization spectrum is typical for very high states of accreting black holes and seems difficult to reproduce at such a low luminosity.

On the other hand, it is possible that we observe soft Comptonization spectrum below a few keV and bremsstrahlung emission above the turnover in the spectrum. In fact, in the frame of the hot flow model, the free-free emission is expected to dominate when the luminosity is substantially sub-Eddington, see Esin et al. (1997).

We checked this possibility with a simple model, consisting of a power-law (which reproduced the part of the spectrum below the turnover), a bremsstrahlung component and a gaussian for the iron line. We again obtained a good fit, at $\chi^2 = 45/64$ d.o.f. The slope of the power-law was $\alpha = 2_{-0.8}^{+1.5}$ while the iron line turned out to be narrow (with the gaussian width smaller than the instrument resolution) and strong ($W_{\text{Fe}} = 530$ eV) at $E_{\text{Fe}} = 6.8_{-0.4}^{+0.3}$ keV. The flux in the line was now $F \approx 3.2 \times 10^{-5}$ photons $\text{cm}^{-2} \text{s}^{-1} \text{deg}^{-2}$, even closer to the estimated contribution from the Galactic emission. The data did not allow for any constraints either on the temperature of the plasma or on possible reflection of bremsstrahlung emission from a cold medium. Consequently, also luminosity of the source (dominated by free-free emission) could not be estimated. If we assumed the plasma temperature $kT_e = 200$ keV, this would correspond to the total luminosity of $L \approx 10^{35}$ erg s^{-1} . This in turn could be produced e.g. in a plasma of $\tau_T \approx 0.35$ and the size of $R \approx 10^9$ cm (note that bremsstrahlung luminosity scales as $\propto T_e^{1/2} \tau_T^2 R$).

2.3.3 Temperature – luminosity relation

The four bright observations of GX 339–4 span a factor of ~ 3 in luminosity. The data were acquired in different years (except for datasets 1 and 2), so the conclusion we can derive concerns the long-term changes in the source.

An important issue is the relation between luminosity, which is dominated by Comptonization, and the temperature of the Comptonizing plasma. The difficulty in our case lies in the possible presence of non-thermal electrons. First, a purely thermal fit to a hybrid plasma would overestimate the true plasma temperature (compare fits 4a and 4b in Table 2.1). Second, if the non-thermal component is present then it should play an important role in establishing the equilibrium between heating and Compton cooling in the plasma. Then the temperature is no longer a good indicator of the state of the plasma.

In the case of mildly-relativistic plasmas with $\tau_T \sim 1$ the relative increase of the luminosity from Comptonization off non-thermal electrons is $\sim \tau_T \delta$ [see Figure 4.4 and equation (4.14)] while the mean electron energy in the distribution, $\langle E \rangle$, increases by a factor of $\sim \delta$. Thus, $\langle E \rangle$ seems to be a good diagnostic tool for the equilibrium state of the plasma.

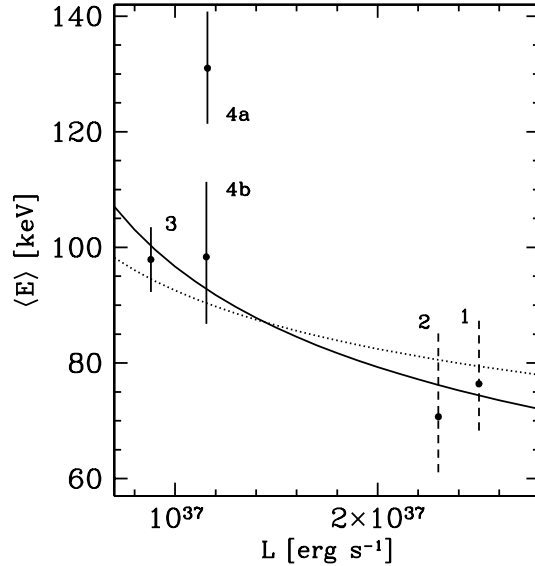


Figure 2.4: Relation between the luminosity and the mean electron energy in fits to datasets 1–4. Labels correspond to fit numbers from Table 2.2. Dashed lines mark *Ginga*/OSSE observations, while solid lines represent fits to *RXTE*/OSSE data. The fitted dependencies of $\langle E \rangle$ on L for the case of advection and cooling dominated flows are represented by solid and dotted curves, respectively (see Section 2.3.3 for model details).

We plotted the dependence of $\langle E \rangle$ on L for the hard state observations in Figure 2.4. The data suggest that the mean electron energy in the plasma found for datasets 3 and 4 is larger than that in fits to datasets 1 and 2, where the luminosity was higher. Such a result for this source, using thermal fits, was reported by Zdziarski (2000).

Interestingly, at the same time the spectral index remains approximately constant (see Table 2.2), i.e. the Compton parameter, y , is also constant while $\langle E \rangle$ varies. Since for semi-relativistic, optically thin thermal plasmas the Compton parameter is roughly $y \approx 4\tau_{\text{T}}kT_{\text{e}}/m_{\text{e}}c^2$ (see Section 1.4.2), for the hybrid case we can assume that approximately $y \propto \langle E \rangle \tau_{\text{T}}$.

The constant y implies basically constant ratio of the Comptonization luminosity to the luminosity in seed photons. Then $\langle E \rangle$ decreases with increasing τ_{T} , which, together with increasing L , would be naturally interpreted as a consequence of increasing accretion rate in a hot flow. This was calculated by Zdziarski (1998) for a hot, two-temperature flow model parameterized by the value of y . The dependence of $\langle E \rangle$ on L , calculated from this model and assuming constant y would be $\langle E \rangle \propto L^{-2/7}$ in an advection-dominated flow and $\langle E \rangle \propto L^{-1/6}$ in a cooling-dominated flow. We checked that the former seems to fit our $\langle E \rangle - L$ relation slightly better, but the

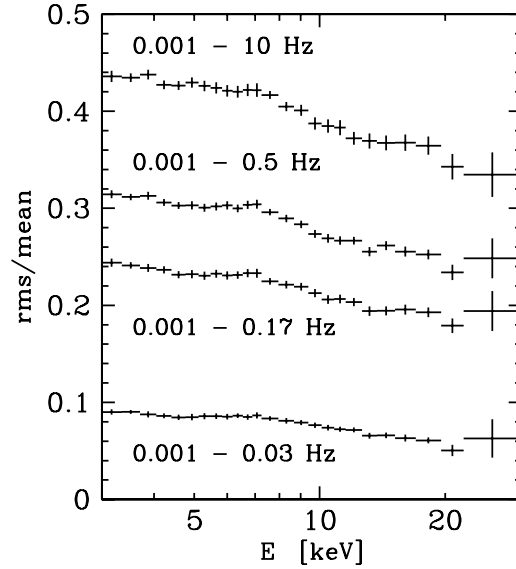


Figure 2.5: The X-ray variability of GX 339–4 in PCA data, dataset 4. A single point represents the ratio of the variance to the mean count rate (where the label marks the frequency range for which the variability was measured) in a light curve, the energy band of which is represented as the horizontal bar.

results are not conclusive (see Figure 2.4, where the fitted dependencies are shown). We note that assuming the black hole mass of $M \sim 10M_{\odot}$, GX 339–4 radiates at the luminosity close to the maximum one predicted by the model of Zdziarski (1998), which is $L \approx 9 \times 10^{36} y^{3/5} (\alpha_v/0.1)^{7/5} (M/10M_{\odot})$.

We can see that using the hybrid fit instead of the thermal one resolves the apparent discrepancy between the values of $\langle E \rangle$ in observations 3 and 4 (fit 4a), where luminosities were similar. If the temperature and luminosity in the hard state were well correlated on long time scales, this would constitute another argument in favour of the presence of non-thermal tails. We note that the lower temperature in fit 3 (compared to fit 4a) is not an artefact of our fits with different values of τ_T for *RXTE* and OSSE data, since the best fit to OSSE data alone (dataset 3) returns $kT_e = 57$ keV, very similar to the result of the fit to both *RXTE* and OSSE data.

2.4 X-ray variability

As it was shown by e.g. Maejima et al. (1984), Nowak, Wilms & Dove (1999) and Revnivtsev et al. (2001), the pattern of X-ray variability of GX 339–4 is different for different photon energies. Motivated by this result we investigated the energy-

dependence of the X-ray variability of GX 339–4 in the *RXTE* data from our dataset 4, which has the best statistics of all our *RXTE* observations.

For this purpose we used all layers in all available detectors (PCUs 0 to 4) in the PCA instrument, so as to obtain more counts and thus better statistics. Then we constructed light curves with different time bin sizes, ΔT , and in different energy bands. The width of the energy bins was chosen as a compromise between minimizing the error and maximizing the energy resolution. For each of the lightcurves we integrated the power density spectrum in the frequency range from 0.001 Hz up to $1/2\Delta T$, to obtain the variation divided by the mean count rate (rms/mean). From the latter value the white noise was subtracted and it was corrected for the background, which is rather strong in GX 339–4, especially at energies exceeding 20 keV.

The results are presented in Figure 2.5. A common feature for all the frequency ranges is a weak break at the energy of ~ 7 keV. Also, with increasing frequency, the ratio of rms/mean below 7 keV to that at energies $\gg 7$ keV decreases. A decrease of rms/mean with increasing energy was also found by Revnivtsev et al. (2000) for other black hole binaries.

For the hard state of GX 339–4 and for a set of observations encompassing our dataset 4, Revnivtsev et al. (2001) found that the reflection component is much less variable at high frequencies (~ 10 Hz), compared to its variability at lower frequencies ($\lesssim 0.1$ Hz), which should result in decreased rms/mean above ~ 10 keV where the reflected component becomes important (compare the relative strength of continuum and reflected components in Figure 2.1). The amount of decrease of the rms/mean we observe would agree with a scenario when the variability in the reflected component is suppressed, however the dependence of rms/mean on energy should have different patterns. Besides, if the observed rms/mean energy-dependence were a result of the reflection variability suppressed at high frequencies, the ratio of rms/mean at low energies to that at high energies should increase with frequency, and we observe an opposite behaviour.

It is thus more likely that we observe a change of the variability pattern in the Comptonization continuum itself. Namely, if the total Comptonization luminosity (likely to be equal to the power liberated in the hot, Comptonizing plasma) remained constant, but the flux in seed photons varied, this would result in pivoting of the spectrum. The pivot energy would in general depend on the spectral index and plasma and seed photons temperature. Because the part of the spectrum close to the pivot energy would be less variable than that further away, this could qualitatively reproduce the observed rms/mean energy-dependence, if the pivot took place at energies > 20 keV.

Then, we would observe declining rms/mean due to both reflection variability suppression and pivoting of the underlying continuum. If the latter effect were stronger, and the seed photon variability strength decreased with increasing frequency, this would qualitatively reproduce the observed frequency-dependence of the rms/mean.

We used a simple model (assuming a power-law spectrum from $\sim 4kT_{\text{seed}}$ to $\sim 3kT_e$, with varying seed photon flux) to check that values of $kT_{\text{seed}} > 0.1$ keV are required for the pivoting energy to be placed at > 20 keV, assuming the observed values of kT_e and variability of the seed photon flux by a factor of a few. This is consistent with the constraints on the temperature of the soft excess we obtained from *Ginga* data.

The above interpretation of the rms/mean energy- and frequency-dependence is, however, by no means unique. E.g. models of magnetic flare avalanches (Poutanen & Fabian 1999) also predict complicated patterns of variability, due to different time scales of the flares.

Chapter 3

Thermal synchrotron emission and its Comptonization

As we stated in Section 1.5.3, synchrotron emission should be taken into account as a source that provides seed photons for Comptonization in optically thin plasmas accreting onto black holes. Our goal is to estimate, to which extent the Comptonized synchrotron emission can contribute to the observed hard X-ray spectra of those objects.

In this Chapter we investigate synchrotron emission and its Comptonization from *purely thermal* plasmas of parameters typical for luminous BHBs in their hard states and Seyfert galaxies, i.e. semi-relativistic ($T_e \sim 10^9$ K) and optically thin ($\tau_T \sim 1$). We first review and clarify previous results of the synchrotron radiation theory as applied to the case of semi-relativistic thermal plasmas and present our approximations. Then an approximate, analytical model of thermal CS emission, based on the results of Zdziarski (1985), is introduced.

The model presented below is later modified and extended in Chapter 4 to account for the CS emission in plasmas with hybrid electron distributions.

3.1 Thermal synchrotron radiation

The theory of radiation of electric charges accelerated by magnetic fields was introduced in the beginning of the 20th century (Schott 1907, 1912) and developed in detail in subsequent decades (e.g. Ivanenko & Sokolov 1948; Schwinger 1949; Trubnikov 1958; Scheuer 1968). Excellent reviews of the subject along with references to the most important works can be found in Bekefi (1966), Pacholczyk (1970) and Jackson (1975).

Analytical description of the spectrum of electrons gyrating in a uniform magnetic field and its dependence on the angle between the field lines and the direction

to the observer is the easiest in the case of ultra-relativistic power-law electron distributions, which is also most often the case of interest for radio astronomy. Also analytical description of thermal synchrotron¹ radiation in the non-relativistic limit (see Chanmugam et al. 1989 for a review) and in the ultra-relativistic one is well developed.

The most difficult case is thermal synchrotron radiation of semi-relativistic electrons (of temperatures $T_e \sim 10^8 - 10^{10}$ K), which encompasses the range of interest for modelling emission from accreting black holes. A number of studies have been devoted to analytical description of this regime of synchrotron emission, e.g. Jones & Hardee (1979), Petrosian (1981), Takahara & Tsuruta (1982), Petrosian & McTiernan (1983), Robinson & Melrose (1984), Mahadevan, Narayan & Yi (1996). The results, however, are not entirely consistent.

3.1.1 Synchrotron emission coefficient in a thermal plasma

The emission spectrum of an accelerated charged particle can be calculated by means of the Lenard-Wiechert potentials. The power emitted by a particle is inversely proportional to its mass, and thus emission of an electron is much more efficient than that of an ion. When an electron spirals around magnetic field lines, the observer receives short pulses of radiation in regular time intervals. Fourier analysis of the electric field measured by the observer, $E(t)$, gives the frequency spectrum of the radiation.

Let us consider an electron moving in a uniform magnetic field, \mathbf{B} , at a velocity, $\boldsymbol{\beta} \equiv \mathbf{v}/c$. Let ζ be the angle between \mathbf{v} and \mathbf{B} , and ϑ be the angle between \mathbf{B} and the direction towards the observer (see Figure 3.1). The synchrotron emission coefficient of a single electron per unit frequency and unit solid angle in the observer's frame is then given (see e.g. Bekefi 1966) by the expression:

$$\eta_\nu(\vartheta, \zeta, \gamma) = \frac{2\pi e^2 \nu^2}{c} \sum_{n=1}^{\infty} \delta(y_n) \left[\left(\frac{\cos \vartheta - \beta \cos \zeta}{\sin \vartheta} \right)^2 J_n^2(z) + \sin^2 \zeta \beta^2 J_n'^2(z) \right], \quad (3.1)$$

where

$$y_n \equiv \frac{n\nu_c}{\gamma} - \nu(1 - \beta \cos \zeta \cos \vartheta), \quad z \equiv \frac{\nu\gamma\beta \sin \vartheta \sin \zeta}{\nu_c}. \quad (3.2)$$

Here, $\nu_c \equiv eB/2\pi m_e c$ is the cyclotron frequency, $\gamma = (1 - \beta^2)^{-1/2}$ is the Lorentz factor and J_n is a Bessel function of order n .

¹We use the term 'synchrotron radiation' independent of the electron energy, though conventionally synchrotron emission of low-energy electrons is called 'cyclotron radiation'.

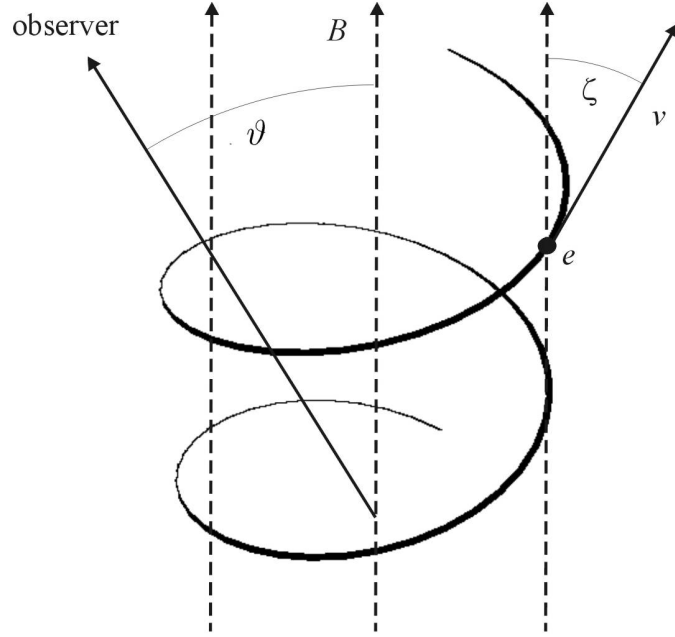


Figure 3.1: Motion of an electron in a uniform magnetic field.

Equation (3.1) shows that the spectrum consists of discrete harmonics at frequencies

$$\nu_n = \frac{n\nu_c}{\gamma(1 - \beta \cos \zeta \cos \vartheta)}. \quad (3.3)$$

The relative separation between harmonics decreases with increasing n , and thus the discrete synchrotron spectrum can be approximated by a continuum at sufficiently large n , which is the case of interest to us, since synchrotron emission in accretion flows is expected to be highly self-absorbed, which issue we discuss in Section 3.1.3.

The spectrum can be well approximated by a continuous one also when the frequency is small but $\gamma \gg 1$, i.e. for ultra-relativistic electrons. Then, there is a well known result that the power emitted by a single ultra-relativistic electron is proportional to (see e.g. Bekefi 1966)

$$\eta_\nu \propto \frac{\nu}{\nu_{\text{crit}}} \int_{\nu/\nu_{\text{crit}}}^{\infty} K_{5/3}(t) dt, \quad (3.4)$$

where $K_{5/3}$ is a Bessel function and $\nu_{\text{crit}} = (3/2)\nu_c\gamma^2$. The expression (3.4) has its maximum at $\nu/\nu_{\text{crit}} \approx 1$, so a single, relativistic electron emits most of the energy at the frequency

$$\nu \sim \gamma^2\nu_c. \quad (3.5)$$

This result has important consequences for synchrotron emission from hybrid plasmas, as we will see in Section 4.2.1.

In fact, an additional factor of $(1 - \beta\mu \cos\vartheta)^{-1}$ due to the Doppler effect should have appeared in the formal derivation of equation (3.1), as it was noticed about twenty years after the development of the synchrotron radiation theory (Epstein & Feldman 1967). However, Scheuer (1968) and Ginzburg & Syrovatskii (1969) showed that this term disappeared in the case of an electron moving chaotically, e.g. in isotropic plasmas, which case we assume throughout this work. For detailed discussion, see Scheuer (1968), Rybicki & Lightman (1979, section 6.7), Pacholczyk (1970, section 3) and references in these works.

The synchrotron emission coefficient, $j_\nu(\vartheta)$, of a thermal plasma in a uniform magnetic field can be obtained by integrating the rate of equation (3.1) over a relativistic, thermal Maxwellian electron distribution,

$$n_e^{\text{th}}(\Theta, \gamma) = \frac{n_e^{\text{th}}}{\Theta} \frac{\gamma(\gamma^2 - 1)^{1/2}}{K_2(1/\Theta)} \exp\left(-\frac{\gamma}{\Theta}\right). \quad (3.6)$$

In the equation above, n_e^{th} is the number density of thermal electrons and K_2 is a modified Bessel function. We also introduced a dimensionless temperature,

$$\Theta \equiv \frac{kT_e}{m_e c^2}. \quad (3.7)$$

The Bessel function can be well approximated by

$$K_2\left(\frac{1}{\Theta}\right) \approx \begin{cases} \left(\frac{\pi\Theta}{2}\right)^{1/2} \left(1 + \frac{15\Theta}{8} + \frac{105\Theta^2}{128} - 0.203\Theta^3\right) e^{-1/\Theta}, & \Theta \leq 0.65; \\ 2\Theta^2 - \frac{1}{2} + \frac{\ln(2\Theta)+3/4-\gamma_E}{8\Theta^2} + \frac{\ln(2\Theta)+0.95}{96\Theta^4}, & \Theta \geq 0.65, \end{cases} \quad (3.8)$$

where $\gamma_E \approx 0.5772$ is Euler's constant and the last coefficients in the series have been adjusted to achieve a relative error ≤ 0.0008 .

The integral for the emission coefficient is then,

$$j_\nu(\vartheta) = \int_1^\infty d\gamma \frac{1}{2} n_e^{\text{th}}(\Theta, \gamma) \int_{-1}^1 d\mu \eta_\nu(\vartheta, \mu, \gamma), \quad (3.9)$$

where $\mu = \cos\zeta$. This integration is relatively difficult to carry out due to the complicated form of the integrand and the presence of Bessel functions.

Petrosian (1981) obtained an approximate solution by replacing the summation over n by integration over ν in equation (3.1) and then using the principal term of an asymptotic expansion of $J_n(z)$, where $0 \leq z \leq n\beta < n$ [see equation (9.3.7) of Abramowitz & Stegun (1970)]. The region of validity of that approximation of J_n is given by $\gamma^2 \ll \nu/\nu_c$. The integration over μ and γ by the method of the steepest descent with some additional approximations yields

$$j_\nu(\vartheta) = \frac{2^{1/2} \pi e^2 n_e^{\text{th}} \nu}{3c K_2(1/\Theta)} \exp\left[-\left(\frac{9\kappa}{2 \sin\vartheta}\right)^{1/3}\right], \quad (3.10)$$

where we defined

$$\kappa \equiv \frac{\nu}{\nu_c \Theta^2}. \quad (3.11)$$

We see that the emission coefficient becomes very small both at large frequencies, and at viewing angles, ϑ , significantly different from $\pi/2$.

We note that equation (26) in Petrosian (1981), which corresponds to the formula (3.10), is too small by a factor of 2 due to the adopted normalization of the electron distribution [equation (23) in Petrosian (1981)] being also twice too small. On the other hand, Takahara & Tsuruta (1982) obtain a formula [equation (2.9) in their paper] for the absorption coefficient for the perpendicular polarization of synchrotron radiation, α_ν^\perp , which agrees with our expression (3.10) for the emission coefficient at $\vartheta = \pi/2$. (They also compute the coefficient for the parallel polarization, α_ν^\parallel , which, however, is negligibly small compared to the dominant coefficient of the perpendicular polarization.) The relation between the absorption and emission coefficients is given by Kirchhoff's law, which, in the case of polarized radiation, contains the source function for each polarization separately, i.e. $B_\nu^\parallel = B_\nu^\perp = B_\nu/2$, where B_ν is the Planck spectrum (see e.g. Chanmugam et al. 1989). The coefficients for polarized radiation are then related to the coefficients including both polarizations by $j_\nu = j_\nu^\parallel + j_\nu^\perp$, $\alpha_\nu = (\alpha_\nu^\parallel + \alpha_\nu^\perp)/2$. We also note that the emission coefficient computed by Jones & Hardee (1979) for $\Theta \gg 1$ is larger than the corresponding limit of equation (3.10) by a factor of $2^{1/2}$.

In our numerical calculations, we used an approximation of $J_n(z)$ in terms of the Airy function [equation (9.3.6) in Abramowitz & Stegun (1970)]. Its relative error reaches the maximum value ~ 0.08 at $n = 1$, $z = 0$, but it rapidly decreases for larger values of n , z . If the argument of the Airy function is < 2.25 , we approximate it by its power series [equation (10.4.3) in Abramowitz & Stegun (1970)] up to the 13th power. Otherwise, we use the approximation to J_n of Petrosian (1981) described above, in which case the maximum error is ~ 0.02 . Typical relative accuracy of the resulting approximation to J_n is then < 0.01 . The accuracy can be further increased by adding the first-order correction to the principal term of the asymptotic expansion of J_n , see equation (9.3.7) in Abramowitz & Stegun (1970). The derivative, J'_n , is calculated with the second expression in equation (9.1.30) of Abramowitz & Stegun (1970). Note that the above method is more accurate, but also more complicated, than a related method given by Wind & Hill (1971).

We have tested the accuracy of formula (3.10) compared to the results of numerical integration (which themselves are in a very good agreement with numerical results tabulated for $\Theta \lesssim 0.1$ by Chanmugam et al. 1989) of equation (3.9) at $\vartheta = \pi/2$ for $10 \leq \nu/\nu_c \leq 1000$ and $10^{-3} \leq \Theta \leq 10$. The ranges have been chosen so as to include parameters most relevant for compact sources (e.g. Takahara & Tsuruta 1982; Zdziarski 1986; Narayan & Yi 1995), and we hereafter use them while

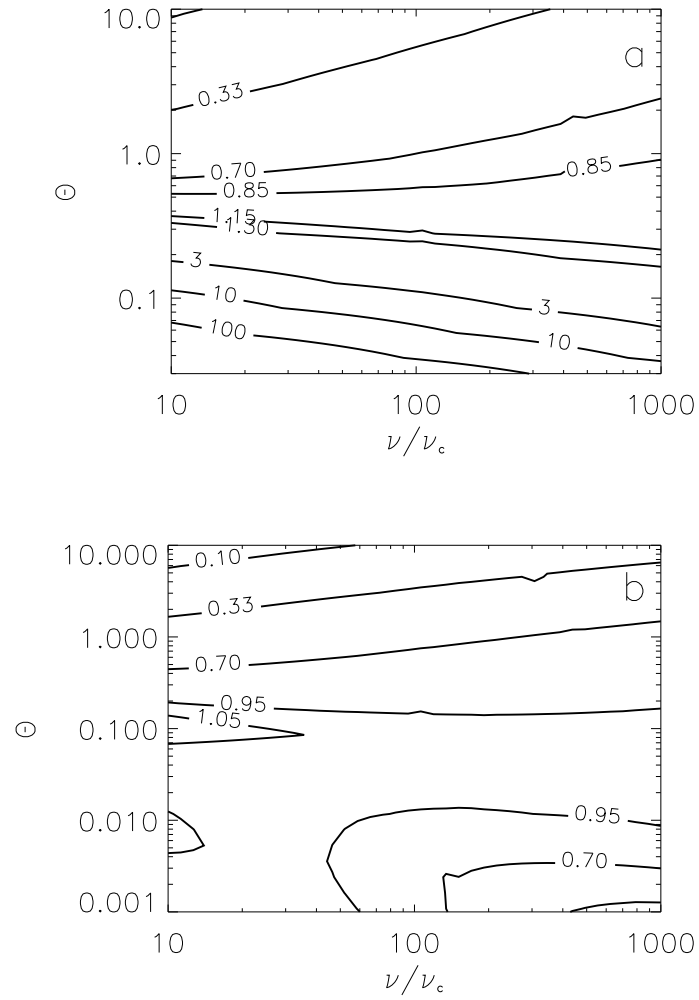


Figure 3.2: (a) Contour plots of the ratio of the approximated emission coefficient of equation (3.10) to the exact numerical value (at $\vartheta = \pi/2$). (b) The same for equations (3.12)–(3.15).

testing other synchrotron rates. Figure 3.2a shows the results for $\Theta > 0.02$. We see that equation (3.10) overestimates the actual value of j_ν by orders of magnitude at low values of Θ , and should not be used at all for $\Theta \lesssim 0.1$. The relative accuracy strongly depends on Θ (being the best at $\Theta \sim 0.4$) and it improves with increasing ν/ν_c . In the relativistic limit, $\Theta \gg 1$, the accuracy of formula (3.10) depends on κ only.

We thus see that the accuracy of the emission coefficient (3.10) is not satisfactory for detailed modelling of astrophysical plasmas, as also found by Mahadevan et al. (1996). We found that a significantly more accurate expression can be obtained by using equation (11) of Petrosian (1981) with additional approximations of equation (25) of Petrosian (1981) and equation (20) of Petrosian & McTiernan (1983),

$$j_\nu(\vartheta) = \frac{\pi e^2}{2c} (\nu\nu_c)^{1/2} \mathcal{X}(\gamma_0) n_e^{\text{th}}(\Theta, \gamma_0) \left(1 + 2\frac{\cot^2 \vartheta}{\gamma_0^2}\right) [1 - (1 - \gamma_0^{-2}) \cos^2 \vartheta]^{1/4} \mathcal{Z}(\vartheta, \gamma_0). \quad (3.12)$$

Here

$$\mathcal{Z}(\vartheta, \gamma) = \left[\frac{t \exp \left[(1 + t^2)^{-\frac{1}{2}} \right]}{1 + (1 + t^2)^{\frac{1}{2}}} \right]^{2n}, \quad t \equiv (\gamma^2 - 1)^{\frac{1}{2}} \sin \vartheta, \quad (3.13)$$

$$n \equiv \frac{\nu(1 + t^2)}{\nu_c \gamma}, \quad \mathcal{X}(\gamma) = \begin{cases} \left[\frac{2\Theta(\gamma^2 - 1)}{\gamma(3\gamma^2 - 1)} \right]^{1/2}, & \Theta \lesssim 0.08; \\ \left(\frac{2\Theta}{3\gamma} \right)^{1/2}, & \Theta \gtrsim 0.08, \end{cases} \quad (3.14)$$

and

$$\gamma_0 = \begin{cases} \left[1 + \left(\frac{2\nu\Theta}{\nu_c} \right) \left(1 + \frac{9\nu\Theta \sin^2 \vartheta}{2\nu_c} \right)^{-\frac{1}{3}} \right]^{\frac{1}{2}}, & \Theta \lesssim 0.08; \\ \left[1 + \left(\frac{4\nu\Theta}{3\nu_c \sin \vartheta} \right)^{\frac{2}{3}} \right]^{\frac{1}{2}}, & \Theta \gtrsim 0.08, \end{cases} \quad (3.15)$$

where γ_0 is the Lorentz factor of the saddle point of the integral (3.9) over γ , corresponding to the minimum of $n_e^{\text{th}}(\Theta, \gamma) \mathcal{Z}(\vartheta, \gamma)/\gamma$. The Lorentz factor γ_0 corresponds to these electrons in the Maxwellian distribution that contribute most to the emission at ν and should not be mistaken with the factor expressed by equation (3.5), which shows a similar relation for a *single* electron. We caution that approximations (3.14) and (3.15) have a small discontinuity at $\Theta \simeq 0.08$.

Figure 3.2b shows the relative accuracy of the approximation of equations (3.12)–(3.15). We see it is much more accurate than expression (3.10) throughout the test range, with the minimum relative error at $0.01 \lesssim \Theta \lesssim 0.2$. Also, the relative accuracy of this approximation varies with Θ and ν/ν_c much slower than that of

equation (3.10). At $\Theta \sim 10^{-3}$ the approximation (3.12)–(3.15) matches well the non-relativistic emission coefficient given by equations (14)–(15) of Trubnikov (1958).

We compared our expression (3.12)–(3.15) with that of Robinson & Melrose (1984), who have also used a method based on that of Petrosian (1981) with accuracy improved with respect to that paper. Their expression, in the form of Dulk (1985) and with the non-relativistic Maxwellian replaced by the relativistic one, is slightly more accurate than expression (3.12)–(3.15), but at the expense of increased complexity.

It has to be noted that a relativistic generalization of the results of Robinson & Melrose (1984) by Hartmann, Woosley & Arons (1988) appears incorrect. Namely, their expression (B1) should be multiplied by a factor $2\pi(\gamma_0^2 - 1)^{-1/2}$ (in their notation).

3.1.2 Angle-averaged emission coefficient

The emission coefficients derived above are appropriate for a plasma in a uniform magnetic field. However, in optically thin plasmas in accretion flows, we expect either to deal with emission from regions where magnetic fields are chaotic (due to complicated structure of the field lines in the accretion flow, see e.g. Balbus & Hawley 1998) or to observe radiation being a sum of contributions from a number of regions with different orientations of magnetic field. In both cases the appropriate quantity, describing the synchrotron emission, would be an emission coefficient averaged over magnetic field directions (or, equivalently, over the viewing angle), $\bar{j}_\nu = \epsilon_\nu/4\pi$, where ϵ_ν is the emitted power per unit volume and frequency, and

$$\bar{j}_\nu = \frac{1}{4\pi} \int j_\nu(\vartheta) d\Omega = \frac{1}{2} \int j_\nu(\vartheta) \sin \vartheta d\vartheta. \quad (3.16)$$

Since synchrotron emission of a single electron has a strong peak at $\vartheta = \pi/2$, we obtained an expression for \bar{j}_ν by integrating equation (3.12) over ϑ with the method of the steepest descent. For that purpose we treated \mathcal{Z} as the fast varying (with ϑ) part of the integrand (3.12). The resulting expression is,

$$\bar{j}_\nu = \frac{\pi^{3/2} e^2 (\nu \nu_c)^{1/2} n_e^{\text{th}}(\Theta, \gamma_0) \mathcal{Z}(\vartheta, \gamma_0) \mathcal{X}(\gamma_0)}{2^{3/2} c} \left| \frac{\partial^2 \ln \mathcal{Z}(\vartheta, \gamma_0)}{\partial \vartheta^2} \right|^{-1/2} \quad (3.17)$$

to be evaluated at $\vartheta = \pi/2$.

On the other hand, integration of the asymptotic emission coefficient (3.10) over ϑ , as done by Mahadevan et al. (1996), yields,

$$\bar{j}_\nu = \frac{2^{1/6} \pi^{3/2} e^2 n_e^{\text{th}} \nu}{3^{5/6} c K_2(1/\Theta) \kappa^{1/6}} a_{\text{corr}}(\Theta, \kappa) \exp \left[- \left(\frac{9\kappa}{2} \right)^{1/3} \right], \quad (3.18)$$

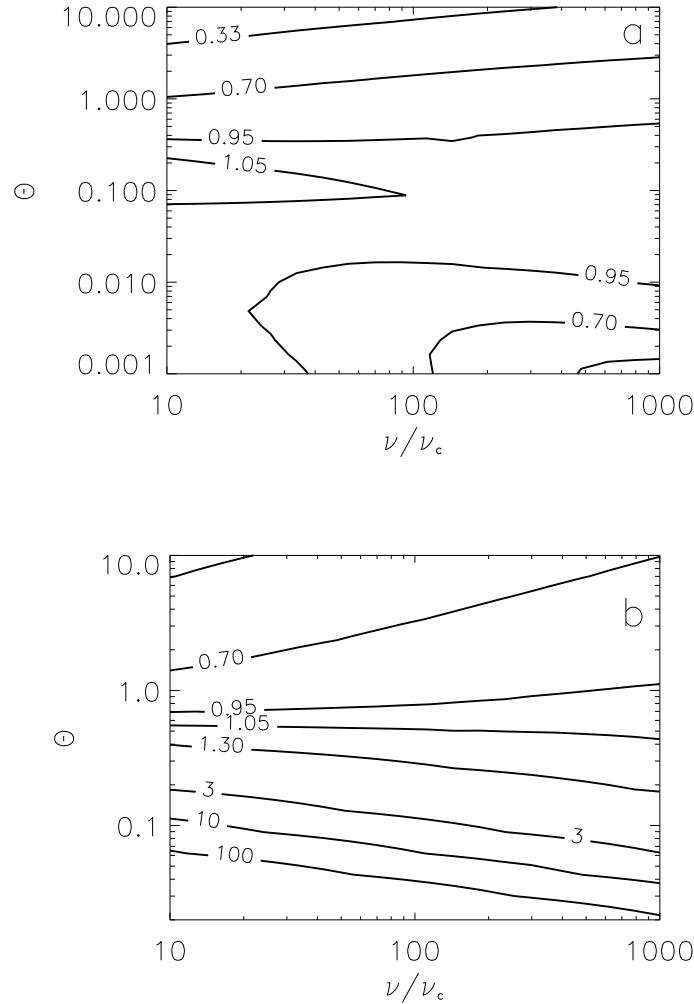


Figure 3.3: (a) Contour plots of the ratio of the approximated emission coefficient (3.17) to the correct numerical value. (b) The same for equation (3.18) with $a_{\text{corr}} \equiv 1$.

where the correction factor, a_{corr} , represents the ratio of the exact emission coefficient to that obtained by integration of equation (3.10). This factor can be calculated from the ratio of equations (33) to (31) in Mahadevan et al. (1996) with fitting coefficients of their Table 1.

We have tested the accuracy of the formulae (3.17) and (3.18), the latter both with and without the tabulated corrections, again in the range $10^{-3} \leq \Theta \leq 10$ and $10 \leq \nu/\nu_c \leq 1000$. Figure 3.3a shows the relative error of equation (3.17). We see that the relative error is typically $\lesssim 30$ per cent except for $\Theta > 1$ with the best accuracy at $0.02 \lesssim \Theta \lesssim 0.4$.

The expression (3.18) with the tabulated corrections of Mahadevan et al. (1996) matches very well the numerical results (the difference is less than a few per cent), with the exception of the case of $\Theta = 0.084$, where the corrections in Table 1 of Mahadevan et al. (1996) appear misprinted as the obtained values are a few times too small and the error increases with frequency, while an opposite behaviour would be expected from this approximation.

The accuracy of formula (3.18) with $a_{\text{corr}} \equiv 1$ is shown in Figure 3.3b. We see that it provides an estimate correct within a factor of ~ 3 or better only for $\Theta > 0.1$ and the best accuracy is obtained at $\Theta \sim 0.6$. This formula strongly overestimates the correct result for $\Theta \lesssim 0.1$. At relativistic temperatures, $\Theta \gg 1$, the relative accuracy of equation (3.18) with $a_{\text{corr}} \equiv 1$ depends on κ only. It underestimates somewhat the actual emission coefficient, and its integration over ν yields a value of the total emitted power too low by a factor of $3^{1/2}35\pi/2^8 \simeq 0.744$ with respect to the actual power,

$$\epsilon = 16\Theta^2 n_e^{\text{th}} \sigma_{\text{T}} c \frac{B^2}{8\pi}, \quad \Theta \gg 1. \quad (3.19)$$

Then, equation (3.18) with $a_{\text{corr}} \equiv 1$ and divided by 0.744 represents an approximation to the ultra-relativistic thermal synchrotron emission coefficient satisfying the total-power constraint (3.19).

3.1.3 Synchrotron self-absorption

The synchrotron radiation is self-absorbed by electrons up to the turnover frequency, ν_t , above which the plasma becomes optically thin to the synchrotron radiation, i.e.,

$$\tau = \alpha_{\nu_t} R = 1, \quad (3.20)$$

where R is the characteristic size of the plasma. Below ν_t , the observed spectrum has the blackbody form, while above ν_t the spectrum is produced by optically thin synchrotron emission.

This stems from the fact that in the case of thermal synchrotron emission the absorption scattering coefficient decreases very fast with increasing frequency. Also, in the cases we consider, $\tau_{\text{T}} \sim 1$. As a result, just below ν_t we have $\tau \gg 1$ and $\tau \gg \tau_{\text{T}}$ while just above ν_t these relations are $\tau \ll 1$ and $\tau \ll \tau_{\text{T}}$. In general, the transition region (from optically thick to optically thin emission) in the spectrum takes a much more complicated form, see e.g. Felten & Rees (1972).

Since in the range of frequencies we consider, the self-absorbed synchrotron emission is approximated by the Rayleigh-Jeans spectrum, from equation (3.20) and Kirchoff's law we have:

$$\frac{\bar{j}_{\nu_t}}{2\nu_t^2 m_e \Theta} R = 1. \quad (3.21)$$

This equation, in general, has to be solved numerically. However, Zdziarski et al. (1998) proposed an approximate solution using equation (3.18),

$$\frac{\nu_t}{\Theta^2 \nu_c} = \frac{343}{36} \ln^3 \frac{C}{\ln \frac{C}{\dots}}, \quad C = \frac{3}{7\Theta} \left[\frac{\pi \tau_T a_{\text{corr}} \exp(1/\Theta)}{3\alpha_f x_c} \right]^{\frac{2}{7}}, \quad (3.22)$$

where $x_c \equiv h\nu_c/m_e c^2$ is a dimensionless cyclotron frequency and α_f is the fine-structure constant. We see that ν_t depends on n_e^{th} and R only through their product, or equivalently, τ_T , i.e. the turnover frequency is independent of the source size. This is also true for the exact numerical solution. Typically, the correction factor, a_{corr} , is a slowly-varying function of frequency [Mahadevan et al. (1996)] so that equation (3.22) for ν_t is explicit.

The dependence of ν_t on a_{corr} is only logarithmic, and thus moderate inaccuracies of determining the synchrotron emission coefficient only slightly affect the value of the turnover frequency (e.g. for typical values of plasma parameters and the emission coefficient overestimated by a factor of 2, the turnover frequency would be overestimated by ~ 10 per cent). This results from very steep dependence of the absorption coefficient on frequency.

Mahadevan (1997) used a slightly different method of determining ν_t . Namely, he equated the total flux of the Rayleigh-Jeans emission to that in the optically-thin synchrotron one. This corresponds to setting the right-hand side of equation (3.21) to 3/4 instead of 1, which changes weakly the resulting value of ν_t as compared to equation (3.22).

We have compared the approximate formula (3.22) with $a_{\text{corr}} \equiv 1$ with results of numerical calculations. It turns out that the error of equation (3.22) is almost independent of the values of the parameters other than Θ . Figure 3.4 compares the results of the two methods in the temperature range $0.03 \leq \Theta \leq 1$ for a source with $\tau_T = 1$, $R = 10^7$ cm and $B = 10^6$ G. We see that for $0.1 \lesssim \Theta \lesssim 1$ the discrepancy does not exceed 20 per cent but grows rapidly for lower temperatures.

We have also found empirically from exact numerical calculations a useful power-law approximation for ν_t as

$$\nu_t \approx 3.2 \times 10^{14} \left(\frac{\Theta}{0.2} \right)^{0.95} \tau_T^{0.05} \left(\frac{B}{10^6 \text{ G}} \right)^{0.91} \text{ Hz}, \quad (3.23)$$

which is accurate to $\lesssim 30$ per cent for $0.05 \lesssim \Theta \lesssim 0.4$, $0.3 \lesssim \tau_T \lesssim 3$, $10 \text{ G} \lesssim B \lesssim 10^8$ G and provided the absorption due to bremsstrahlung can be neglected, see Section 3.1.4 below. It is therefore of sufficient accuracy for rough analytical estimates of the role of synchrotron emission in both BHBs and AGNs where the plasma temperature has been measured.

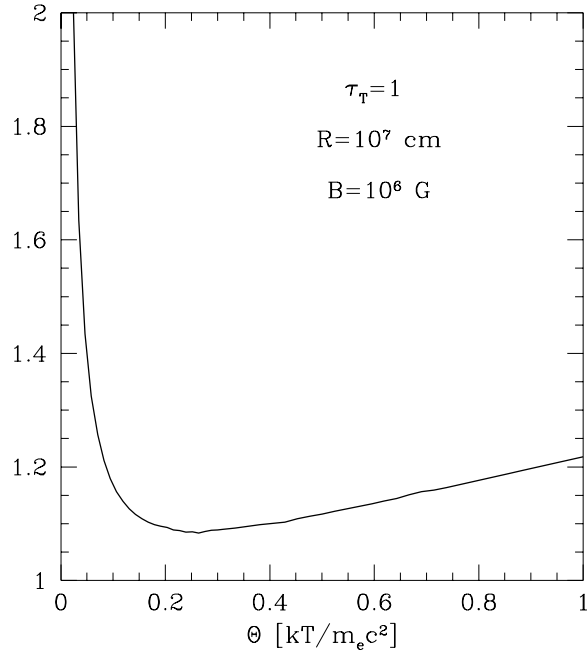


Figure 3.4: The ratio of the turnover frequency calculated from equation (3.22) with $a_{\text{corr}} \equiv 1$ to the accurate numerical result as a function of temperature.

Typical values of ν_t/ν_c expected in accretion flows, assuming equipartition magnetic fields, are from tens to hundreds, the former value typical for BHs and the latter for AGNs (the difference results from different magnetic field strengths). We see from equation (3.5) that this corresponds to rather large electron Lorentz factors of the order of a few or more. Therefore, highly self-absorbed emission from semi-relativistic thermal plasmas, which peaks at ν_t , is produced mainly by high-energy electrons from the tail of the Maxwellian distribution and is therefore very sensitive to the presence of non-thermal tails in the electron distribution. We investigate this issue in detail in Chapter 4.

3.1.4 Effect of bremsstrahlung on the turnover frequency

The formulae for the turnover frequency derived above did not take into account bremsstrahlung emission and absorption. However, for the magnetic field weak enough, bremsstrahlung emission will be comparable to or stronger than the synchrotron one and then the turnover frequency determined neglecting bremsstrahlung will be incorrect. Then, the absorption coefficient, α_ν , should include a contribution

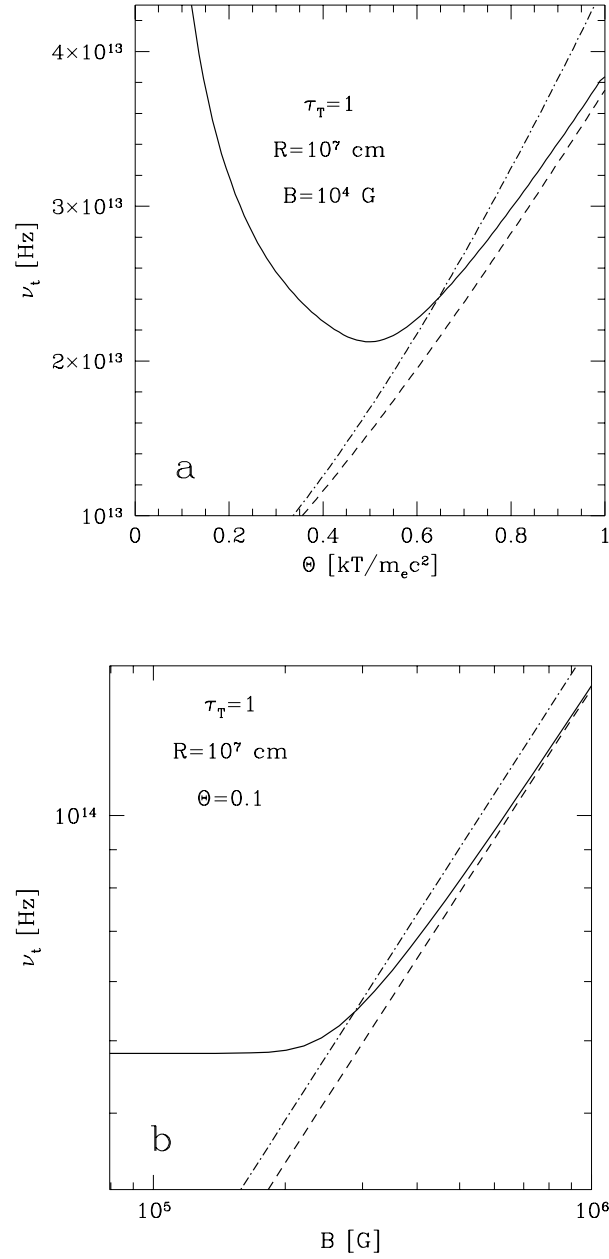


Figure 3.5: Example dependences of the turnover frequency on (a) temperature and (b) magnetic field strength. The dot-dashed and dashed curves give ν_t calculated with the analytic approximation of equation (3.22), and numerically using equation (3.21), respectively, with bremsstrahlung neglected in both cases. The solid curves give the numerical results with bremsstrahlung taken into account.

from bremsstrahlung, α_ν^{ff} . In this case, since $\alpha_\nu^{\text{ff}} \propto n_e^2 R$, the turnover frequency is no more solely a function of τ_T whenever bremsstrahlung is important.

The effect of bremsstrahlung on the turnover frequency can be checked by computing ν_t without taking into account bremsstrahlung, and then computing the emission coefficient, \bar{j}_{ν_t} , including both processes. As long as $\bar{j}_{\nu_t} \gg j_{\nu_t}^{\text{ff}}$, equations in Section 3.1.3 can be used.

We have calculated the turnover frequency as a function of Θ and B for the remaining parameters fixed, see Figures 3.5a, b, respectively. In these calculation we employed formulae for the free-free emission coefficient of Svensson (1984). As expected, ν_t is determined mostly by bremsstrahlung at low temperatures and weak magnetic fields.

3.2 Comptonization of synchrotron photons

3.2.1 The Comptonization spectrum

Synchrotron photons will in general undergo Compton scattering in the same plasma where they have been produced. As we have seen, in the case of a thermal plasma in an accretion flow, the synchrotron spectrum is usually self-absorbed up to a high value of ν/ν_c (see Section 3.1.3). Then the self-absorbed synchrotron spectrum consists of a hard Rayleigh-Jeans spectrum at $\nu \lesssim \nu_t$ and a fast-declining tail of the optically-thin synchrotron spectrum at $\nu \gtrsim \nu_t \gg \nu_c$ (see Figure 4.2 in Chapter 4). It is thus rather narrow and for the purpose of Comptonization models it can be approximated as a monochromatic source of seed photons at ν_t [see e.g. Monte Carlo simulations in Zdziarski (1986)], as long as we are interested in the shape of the Comptonization spectrum for $\nu \gg \nu_t$ only.

For the hot plasma parameters expected in accretion flows we have $h\nu_t \ll kT_e$, and thus photons at $\nu \sim \nu_t$ gain energy in the scattering process. In fact, most of the scatterings a photon of initial energy $\sim h\nu_t$ undergoes in a semi-relativistic plasma takes place in the Thomson regime.

We treat thermal Comptonization with an approximate analytical method developed by Zdziarski (1985) and applied to thermal synchrotron sources in Zdziarski (1986). This method is further modified in Chapter 4 so as to describe hybrid synchrotron self-Comptonization.

We consider a homogeneous and isotropic source characterized by τ_T , Θ and B . The flux in the Comptonization spectrum is approximated by a sum of a cut-off power law and a Wien component,

$$F_C(x) = N_P \left(\frac{x}{\Theta}\right)^{-\alpha} e^{-x/\Theta} + N_W \left(\frac{x}{\Theta}\right)^3 e^{-x/\Theta}, \quad (3.24)$$

where $x \equiv h\nu/m_e c^2$ is a dimensionless photon energy. N_P and N_W are normalizations of the power-law and Wien components, respectively. The shape of such a spectrum is shown in Figure 3.6.

For $\tau_T \lesssim 2$, the spectral index can be approximately given by (e.g. Rybicki & Lightman 1979),

$$\alpha = -\frac{\ln P_{sc}}{\ln A}, \quad A \approx 1 + 4\Theta + 16\Theta^2, \quad (3.25)$$

where A is the average photon energy amplification per scattering and has been already introduced in Section 1.4.2. P_{sc} represents the scattering probability averaged over the source volume. In spherical geometry (Osterbrock 1974),

$$P_{sc} = 1 - \frac{3}{8\tau_T^3} [2\tau_T^2 - 1 + e^{-2\tau_T}(2\tau_T + 1)] \quad \rightarrow \quad \begin{cases} \frac{3\tau_T}{4}, & \tau_T \ll 1; \\ 1 - \frac{3}{4\tau_T}, & \tau_T \gg 1, \end{cases} \quad (3.26)$$

where τ_T is interpreted as the Thomson optical depth along the radius.

For an infinite slab geometry the corresponding expression for the scattering probability takes the form:

$$P_{sc} = 1 - \tau_T \text{Ei}(-2\tau_T) - \frac{1}{4\tau_T} [1 + e^{-2\tau_T}(2\tau_T - 1)] \quad \rightarrow \quad \begin{cases} -\tau_T \ln 2\tau_T, & \tau_T \ll 1; \\ 1 - \frac{1}{4\tau_T}, & \tau_T \gg 1, \end{cases} \quad (3.27)$$

where Ei is the exponential integral function and τ_T corresponds now to the half-thickness of the slab [see also Zdziarski et al. (1994) for another formulation].

We have found an empirical power-law approximation to $\alpha(\tau_T, \Theta)$ in the spherical geometry, valid at $0.5 \lesssim \tau_T \lesssim 2$ and $\Theta \lesssim 0.4$,

$$\alpha \approx \frac{3}{19} \frac{1}{\tau_T^{4/5} \Theta}. \quad (3.28)$$

Since the expressions for the synchrotron luminosity we derive in this Section are parameterized not by the optical depth but by the spectral index, in general different prescriptions for $\alpha(\tau, \Theta)$ can be used, e.g. in order to account for a different geometry or to increase the accuracy.

As we already stated in Section 1.4.2, when the optical depth is small (i.e. $\tau_T \ll 1$), profiles corresponding to subsequent scatterings are visible in the Compton spectrum, and a power law is no longer a good approximation to the shape of the spectrum below the cut-off. Still, the power-law description presented here gives the shape averaged over the scattering orders, and an integral over that approximate form gives a fair approximation to the total luminosity [see, e.g., Monte Carlo simulations in Zdziarski (1986)].

On the other hand, at $\tau_T \gtrsim 2$, Comptonization can be described by means of a kinetic, Fokker-Planck, equation (Sunyaev & Titarchuk 1980; see e.g. Lightman & Zdziarski 1987 for relativistic and low- τ_T corrections). The two solutions can be matched at $\tau_T \sim 2$ (Zdziarski 1985). The remaining results presented in this Section can still be used at $\tau_T \gtrsim 2-3$, except for a different prescription for α . In particular, the ratio of N_W/N_P given by Zdziarski (1985),

$$\frac{N_W}{N_P} = \frac{\Gamma(\alpha)}{\Gamma(2\alpha + 3)} P_{sc}, \quad (3.29)$$

where Γ is Euler's gamma function, and which uses a result of Sunyev & Titarchuk (1980), is a good approximation in both the optically-thin and optically-thick regimes.

3.2.2 Synchrotron radiation as a source of soft photons

Having modelled the shape of the Comptonization spectrum, we need to normalize its flux, $F_C(x)$, with respect to that in the Rayleigh-Jeans spectrum, $F_{RJ}(x)$. In general, the self-absorbed synchrotron spectrum at its peak around x_t (hereafter all indices of x correspond to those of ν , i.e. $x_t \equiv h\nu_t/m_e c^2$) is somewhat above an extrapolation of the power-law component of the Compton spectrum, $F_C(x)$. So as to find the relative normalization of the two fluxes at x_t we use a phenomenological relation found by Zdziarski (1986),

$$F_C(x_t) = \varphi F_{RJ}(x_t) \quad (3.30)$$

where

$$\varphi(\Theta) \approx \frac{1 + (2\Theta)^2}{1 + 10(2\Theta)^2}. \quad (3.31)$$

This is valid for $x_t \ll \Theta$, which condition we assume hereafter and it is always fulfilled in accretion flows. The flux of the Rayleigh-Jeans spectrum is given by

$$F_{RJ}(x) = \pi I_{RJ}(x), \quad (3.32)$$

where

$$I_{RJ}(x) = \frac{2m_e c^3 \Theta}{\lambda_C^3} x^2 \quad (3.33)$$

is the specific intensity and λ_C is the electron Compton wavelength. Then, from equations (3.24) and (3.30) we have

$$N_P = \pi \varphi I_{RJ}(x_t) (x_t/\Theta)^\alpha. \quad (3.34)$$

The luminosity due to the CS emission is then given by

$$L_{CS}^{\text{th}} = L_S^{\text{th}} + L_C^{\text{th}} = \mathcal{A} \left[\int_0^{x_t} dx F_{RJ}(x) + \int_{x_t}^{\infty} dx F_C(x) \right]. \quad (3.35)$$

where L_S^{th} and L_C^{th} are luminosities in the synchrotron and Compton spectra, respectively, and \mathcal{A} is the source area. This expression we integrate to

$$L_{\text{CS}}^{\text{th}} = \mathcal{A} \frac{2\pi m_e c^3 \Theta x_t^3}{3\lambda_C^3} \left\{ 1 + 3\varphi \left(\frac{x_t}{\Theta} \right)^{\alpha-1} \left[\Gamma \left(1 - \alpha, \frac{x_t}{\Theta} \right) + \frac{6\Gamma(\alpha)P_{\text{sc}}}{\Gamma(2\alpha + 3)} \right] \right\}, \quad (3.36)$$

where the incomplete gamma function is well approximated for $x_t \ll \Theta$ by,

$$\Gamma \left(1 - \alpha, \frac{x_t}{\Theta} \right) \simeq \begin{cases} \ln \frac{\Theta}{x_t} - \gamma_E, & |\alpha - 1| < 10^{-3}; \\ \frac{\Theta}{x_t} - \ln \frac{\Theta}{x_t} - 1 + \gamma_E, & |\alpha - 2| < 10^{-3}; \\ \frac{1}{\alpha-1} \left(\frac{\Theta}{x_t} \right)^{\alpha-1}, & \alpha > 2.99; \\ \Gamma(1 - \alpha) - \frac{(x_t/\Theta)^{1-\alpha}}{1-\alpha} + \frac{(x_t/\Theta)^{2-\alpha}}{2-\alpha}, & \text{otherwise.} \end{cases} \quad (3.37)$$

At $x_t/\Theta = 0.01$, the maximum relative error of this approximation of ~ 0.02 occurs around $\alpha \simeq 3$. The relative error declines rapidly at lower values of x_t/Θ and α ; e.g., it is < 0.001 at $x_t/\Theta = 0.01$ and $\alpha \leq 2.9$, and < 0.002 at $x_t/\Theta = 10^{-3}$ at any α .

In an astrophysically important case of $\alpha \sim 0.4$ – 0.9 (e.g. Gierliński et al. 1997; Zdziarski et al. 1999), the main contribution to the luminosity comes from the high-energy end of the spectrum, and the Wien component is relatively unimportant. Then, we obtain an approximation valid within a factor of $\lesssim 2$ at $x_t/\Theta \lesssim 10^{-5}$,

$$L_{\text{CS}}^{\text{th}} \approx \frac{8\pi^2 m_e c^3 R^2}{(1 - \alpha)\lambda_C^3} x_t^{2+\alpha} \varphi \Theta^{2-\alpha}, \quad (3.38)$$

where we assumed a spherical geometry. On the other hand, for soft spectra, with $\alpha \gtrsim 1.1$, we get an approximation valid within ~ 30 per cent,

$$L_{\text{CS}}^{\text{th}} \approx \frac{8\pi^2 m_e c^3 R^2}{3\lambda_C^3} \left(1 + \frac{3\varphi}{\alpha - 1} \right) x_t^3 \Theta. \quad (3.39)$$

We can then substitute x_t of equation (3.23) in equations (3.38)–(3.39). This provides us with an approximate dependence of the CS luminosity on the source parameters, $L_{\text{CS}}^{\text{th}} \propto R^2 \Theta^{3.78-0.11\alpha} B^{1.82+0.91\alpha}$ and $\propto R^2 \Theta^{3.66} B^{2.73}$ for $0.4 \lesssim \alpha \lesssim 0.9$ and $\alpha \gtrsim 1.1$, respectively.

The advantage of the above approach is that the shape of the Comptonization spectrum and its luminosity are calculated self-consistently. This method reproduces relatively accurately the total power in the scattered spectrum [see comparison with Monte Carlo results in Zdziarski (1986)]. On the other hand, it gives a relatively inaccurate shape of the high-energy cut-off of the scattered spectrum (see, e.g., Poutanen & Svensson 1996).

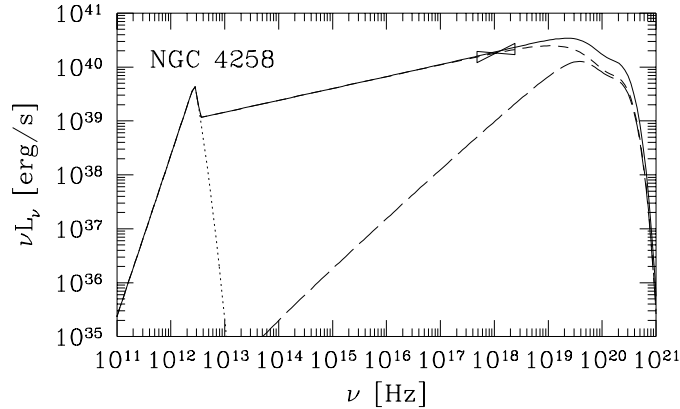


Figure 3.6: An example of the spectrum of a magnetized plasma, for $R = 9 \times 10^{13}$ cm, $B = 2.2 \times 10^3$ G, $\tau_T = 0.47$ and $\Theta = 0.4$. The dotted, short-dashed and long-dashed curves represent spectra due to synchrotron emission, its Comptonization and Comptonized bremsstrahlung, respectively. The solid curve represents the sum of those components. This spectrum also represents a model of a hot accretion flow fitted to the X-ray data for NGC 4258 (bow-tie, Makishima et al. 1994), see Section 5.1.1.

We caution, however, that the relation between optical depth, temperature and spectral index depends in general both on the geometry of the source and on the distribution of soft photon sources in the Comptonizing plasma cloud. Given the observed values of α and Θ , one can derive an approximate value of τ_T from relation (3.25). On the other hand, due to the uncertainties mentioned above, one cannot use τ_T as the primary model parameter so as to determine α and then compare it against specific observations. This is why α , as an observable quantity, is the main parameter in our model, instead of τ_T .

Figure 3.6 shows an example of the CS spectrum for parameters typical to low-luminosity AGNs. The spectrum has the Rayleigh-Jeans shape below the turnover frequency, it is a power law due to Comptonization above that frequency, and then it has a thermal high-energy cut-off. We also show the contribution due to Comptonized bremsstrahlung, which is moderately important for the chosen parameters. We have computed the latter spectrum by treating the spectrum of equation (3.24) as Green's function for Comptonization and then integrating over the seed spectrum of optically-thin bremsstrahlung. The spectrum is computed assuming spherical geometry. More examples of spectra from magnetized plasmas are given, e.g. in Zdziarski (1986).

For given Θ , the Rayleigh-Jeans part of the spectrum is independent of B , and its spectral luminosity is $L_{RJ}(\nu) \propto R^2$. On the other hand, the CS spectrum obeys $L_{CS}^{th}(\nu) \propto R^2 \nu_t^{2+\alpha}$ [equation (3.34)], i.e. its normalization increases quickly with in-

creasing B via the dependence of the turnover frequency on B . When self-absorption is dominated by the synchrotron process, ν_t is roughly $\propto B$ with no explicit dependence on R , see equation (3.23). The total luminosity, $L_{\text{CS}}^{\text{th}}$, follows the same dependence if $\alpha \lesssim 1$, see equation (3.38), while $L_{\text{CS}}^{\text{th}} \propto R^2 \nu_t^3$ for $\alpha \gtrsim 1$, see equation (3.39).

The bremsstrahlung luminosity can be constrained from below as

$$L_{\text{CB}} > 1.2 \times 10^{27} \Theta^{1/2} \tau_{\text{T}}^2 R \approx 1.2 \times 10^{25} \alpha^{-5/2} \Theta^{-2} R. \quad (3.40)$$

where we used a simple approximation to the bremsstrahlung luminosity, see Rybicki & Lightman (1979), neglecting Comptonization and relativistic corrections, which effects will increase the actual L_{CB} . The last expression uses the approximation of equation (3.28) to $\alpha(\tau_{\text{T}}, \Theta)$. We then see that the L_{CB} above represents a strict lower limit to the luminosity of a source where Comptonized synchrotron emission takes place, independent of the field strength, given the values of Θ , τ_{T} and R .

Figure 3.7 shows some example dependences of the total L on B at $\Theta = 0.05\text{--}0.4$ for $R = 4 \times 10^7$ cm and 4×10^{14} cm (corresponding to $\sim 30R_{\text{g}}$ for $10M_{\odot}$ and 10^8M_{\odot} black-hole mass, respectively). The flat parts at low values of B correspond to the dominant bremsstrahlung, with its relative importance increasing with decreasing Θ .

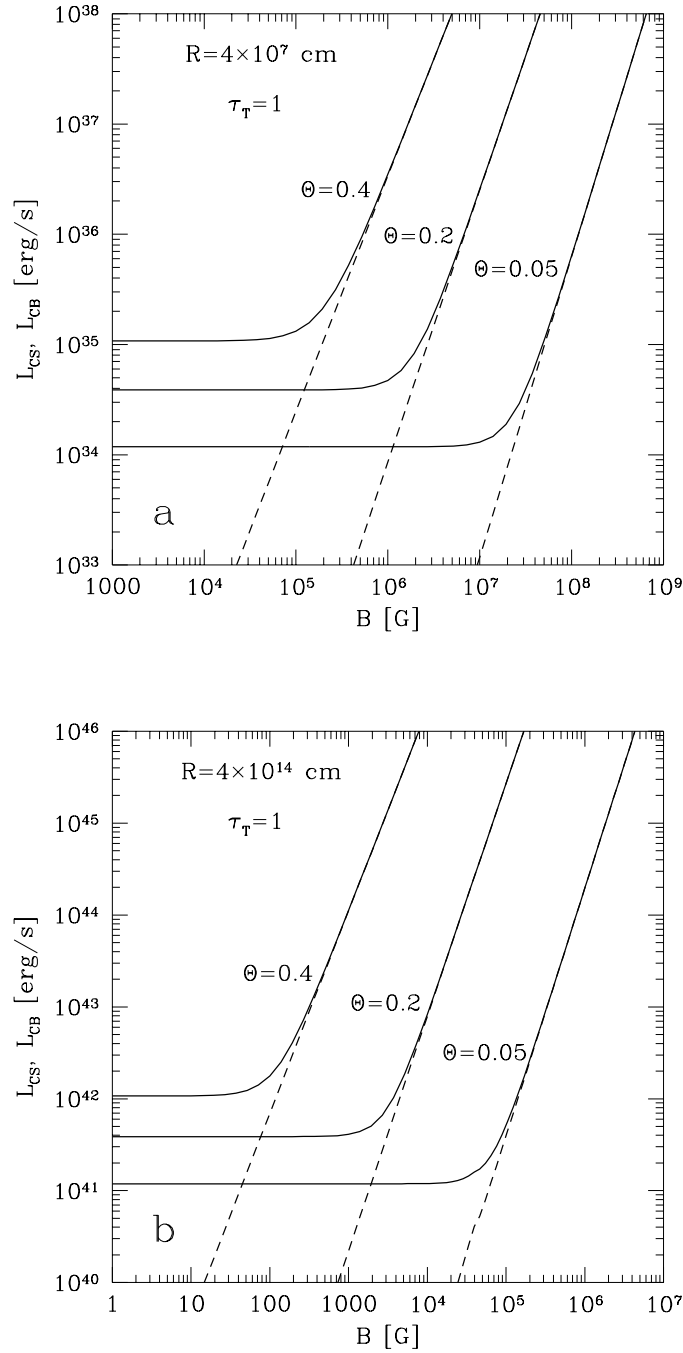


Figure 3.7: Example dependences of the plasma luminosity on B for (a) $R = 4 \times 10^7$ cm and (b) $R = 4 \times 10^{14}$ cm for three values of temperature. The flat parts correspond to dominant bremsstrahlung, and dashed curves give the luminosity in the CS component alone.

Chapter 4

Synchrotron emission and self-Comptonization in hybrid plasmas

As we have seen in Section 3.1.3, thermal synchrotron emission is heavily self-absorbed in an optically thin plasma accreting onto a black hole and therefore most of the luminosity is produced by high-energy electrons. Thus, the presence of a high-energy non-thermal tail in the electron distribution is expected to amplify significantly the synchrotron emission.

Such a tail above ~ 1 MeV has been detected in the spectrum of Cygnus X-1 in the hard state by the COMPTEL detector aboard *CGRO* (McConnell et al. 1994, 2000a, 2002) and we also found hints for its presence in GX 339-4 (Section 2.3.1). In other BHBs and in Seyferts, the existing upper limits are compatible with the presence of weak non-thermal tails (e.g. Gondek et al. 1996; Johnson et al. 1997).

Below we discuss the presence of plasmas with hybrid electron distributions in accretion flows and then develop a model of CS emission in such plasmas. The model is based on the model for thermal CS processes we introduced in the previous Chapter.

4.1 Hybrid electron distributions

In accretion flows, hybrid electron distributions can be produced e.g. by stochastic acceleration of thermal electrons by interaction with plasma instabilities, e.g. with whistlers via gyroresonance (as applied to the case of Cygnus X-1 by Li, Kusunose & Liang 1996) or with fast-mode Alfvén waves via transit-time damping (Li & Miller 1997). Such process can result from dissipation of magnetic field in an accretion

disc corona or in an optically thin accretion flow (see Section 1.5.2), provided a significant fraction of the released energy generates turbulence.

Li & Miller (1997) considered parameters typical for a plasma in an accretion disc corona in a BHB. They have shown, by solving the Fokker-Planck equation for the electron distribution, that electrons can be effectively accelerated from the thermal background to relativistic energies. As a result, when the stationary state is reached, a non-thermal tail of a power-law-like shape develops above certain Lorentz gamma factor $\gamma_{\text{nth}} \sim 2$ (the value of γ_{nth} is in general determined by the efficiency of thermalization processes relative to the acceleration) and the power-law index, p , depends strongly on the plasma optical depth. The non-thermal component is cut off at a $\gamma_f \sim 10$ due to radiative losses overcoming acceleration. Dermer, Miller & Li (1996) predicted somewhat larger cut-off energies in the case of electron acceleration by whistlers and in a plasma with parameters relevant for AGNs.

Similar shape of steady-state electron distribution is also predicted from thermalization by synchrotron self-absorption and Coulomb interactions of an injected power-law electron distribution (produced by any acceleration mechanism), as shown by Ghisellini, Guilbert & Svensson (1988).

The exact shape of the non-thermal tail depends strongly on the plasma parameters and the mechanism of magnetic field dissipation and electron acceleration and thermalization, which is still uncertain. We therefore consider a rather generic electron distribution function of the form qualitatively reproducing that predicted by detailed modelling of electron acceleration, namely

$$n_e(\gamma) = \begin{cases} n_e^{\text{th}}(\Theta, \gamma), & \gamma \leq \gamma_{\text{nth}}; \\ n_e^{\text{th}}(\Theta, \gamma_{\text{nth}}) \left(\frac{\gamma}{\gamma_{\text{nth}}}\right)^{-p} \exp\left(\frac{\gamma - \gamma_{\text{nth}}}{\gamma_f}\right), & \gamma > \gamma_{\text{nth}}. \end{cases} \quad (4.1)$$

Here, the electron distribution is normalized by the relation, $n_e = \int_1^\infty n_e(\gamma) d\gamma$, where n_e is the *total* electron density. This hybrid electron distribution consists thus of a thermal part below γ_{nth} and an e-folded power-law above it.

It has to be noted that the cases $p \lesssim 3$ and $p > 3$ are qualitatively different. In the former, most of the non-thermal synchrotron luminosity is produced by electrons with $\gamma \lesssim \gamma_f$ and the non-thermal synchrotron spectrum is hard. Then, the value of γ_f is an important parameter influencing the spectrum of emission from the plasma. When $p > 3$, the luminosity is produced mostly by low-energy electrons, $\gamma \sim \gamma_{\text{nth}}$, and the spectrum is soft. Consequently, as long as $\gamma_f \gg \gamma_{\text{nth}}$, its value negligibly influences the radiative processes. COMPTEL observations of Cygnus X-1 suggest that $p > 3$.

We consider both the cases, assuming $p \geq 3$, though for simplicity all analytical approximations below are presented for the more likely case $p > 3$, when the exponential cut-off can be neglected in calculations.

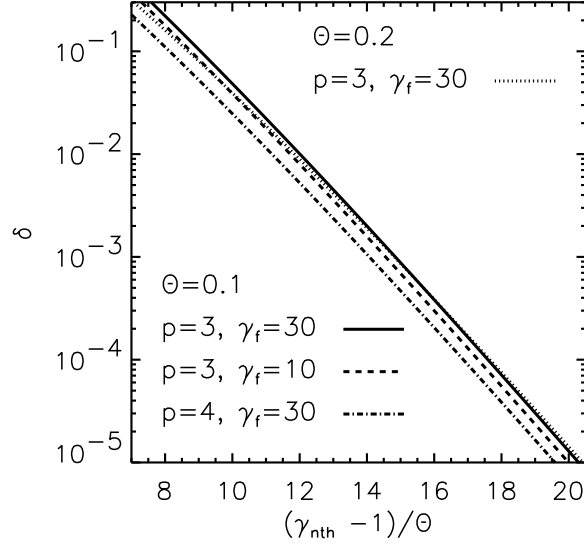


Figure 4.1: The relation between γ_{nth} and δ for different plasma parameters.

The degree to which a hybrid distribution is non-thermal can be measured by the quantity, $(\gamma_{\text{nth}} - 1)/\Theta$, which shows how far in the Maxwellian tail the non-thermal power law starts.

Another such quantity is the ratio of the energy densities in the non-thermal and thermal parts of the electron distribution, δ . For mildly relativistic temperatures and $\gamma_{\text{nth}} - 1 \gg \Theta$, this ratio can be approximated as

$$\delta \approx \frac{\int_{\gamma_{\text{nth}}}^{\infty} (\gamma - 1)n_e(\gamma)d\gamma}{\frac{6+15\Theta}{4+5\Theta}\Theta n_e} \approx \frac{4 + 5\Theta}{6 + 15\Theta} \frac{(\gamma_{\text{nth}}^2 - 1)^{1/2}}{\Theta^2 K_2\left(\frac{1}{\Theta}\right)} \left(\frac{\gamma_{\text{nth}}^3}{p-2} - \frac{\gamma_{\text{nth}}^2}{p-1} \right) e^{-\frac{\gamma_{\text{nth}}}{\Theta}}, \quad (4.2)$$

where we employed an approximation for the thermal energy density from Gammie & Popham (1998). Typical relations between δ and $(\gamma_{\text{nth}} - 1)/\Theta$ are shown in Figure 4.1.

Since the exponential term in equation (4.2) varies fastest, we have an approximate dependence,

$$\gamma_{\text{nth}} \approx C - \Theta \ln \delta, \quad (4.3)$$

where $C \sim 1$ is a function slowly increasing with increasing Θ and γ_{nth} . We then see that $(\gamma_{\text{nth}} - 1)/\Theta$ only weakly depends on Θ and the shape of the tail for a given δ , see again Figure 4.1.

4.2 Synchrotron emission from hybrid plasmas

4.2.1 Comparison of spectra from thermal and hybrid plasmas

If we assume that magnetic field strength in an accretion flow is of the order of the value corresponding to equipartition with gas internal energy, then the predicted values of the turnover frequency for a thermal plasma are $\nu_t \sim 10^{15}$ Hz for black hole binaries (where $B \sim 10^7$ G) and $\nu_t \sim 10^{12}$ Hz for AGNs (where $B \sim 10^3$ G), see Section 5.1 for accretion flow model details and Section 3.1.3 for turnover frequency calculations.

These values correspond to ν_t/ν_c from tens to hundreds. The ratio, ν_t/ν_c , is larger in AGNs, which results from their magnetic field being weaker than that in BHBs, see equation (3.23). Then, the Lorentz factor, γ_t , of the electrons that emit most of their synchrotron radiation at ν_t is of the order of $\gamma_t \sim (\nu_t/\nu_c)^{1/2}$, see equation (3.5). The value of γ_t is therefore of the order of a few, again larger in AGNs than in BHBs.

In order to analyze qualitatively the influence of non-thermal tails on synchrotron spectrum, let us consider first a homogenous cloud of thermal plasma. The self-absorbed spectrum below the thermal turnover frequency, ν_t^{th} , is a Rayleigh-Jeans spectrum. Above ν_t^{th} , the synchrotron emission drops rapidly and then Comptonized emission dominates.

Now, let us assume that the electron distribution is given by equation (4.1). If $\gamma_{\text{nth}} < \gamma_t$, the number of electrons with $\gamma \sim \gamma_t$ will increase (compared to the thermal case). In consequence, the absorption coefficient will be larger and therefore the new turnover frequency, ν_t^{nth} , will increase too. Also the shape of the synchrotron spectrum is modified in this case. At low frequencies both emission and absorption are dominated by thermal electrons so that the optically thick spectrum is still the Rayleigh-Jeans one. However, at higher frequencies the emission of non-thermal electrons starts to dominate, while absorption is still dominated by thermal electrons [which is a consequence of the thermal distribution falling off much more steeply than the non-thermal one, see equation (4.4)], and the optically-thick spectrum quickly increases. This leads to the regime in which both the non-thermal emission and absorption dominate (over thermal emission and absorption), in which case the spectrum is proportional to the source function of non-thermal electrons. Finally, the spectrum becomes optically thin ($\propto \nu^{-(p-1)/2}$), turning over above ν_t^{nth} .

This behaviour is shown in Figure 4.2 where the resulting synchrotron spectra are calculated for two different energy contents of the non-thermal tail and, as a reference, for the purely thermal case. We see that the non-thermal tail has to be

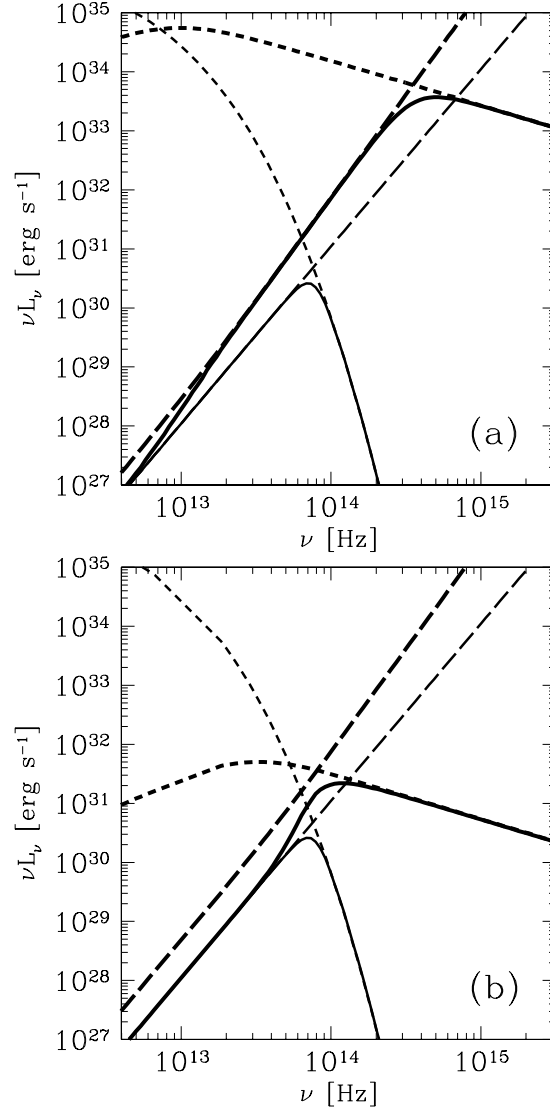


Figure 4.2: Synchrotron spectra from a spherical source with the relative energy content of the non-thermal tail of (a) $\delta = 0.19$, (b) $\delta = 10^{-4}$, and other plasma parameters as in the model of CS emission from Cygnus X-1, which we present in Section 5.2.2. The heavy short-dashed curve shows the optically-thin emission of the non-thermal electrons alone, $(4/3)\pi R^3(4\pi j_\nu^{\text{pl}})$, where j_ν^{pl} is their emission coefficient. The heavy long-dashed curve shows the self-absorbed emission of the non-thermal electrons, $4\pi^2 R^2 S_\nu^{\text{pl}}$, where S_ν^{pl} is their source function. The thin short-dashed and long-dashed curves show the thermal ($\delta = 0$) optically-thin and optically-thick emission, respectively. The heavy and thin solid curves give the corresponding emergent spectra, which change from optically thick to optically thin around the turnover frequency.

sufficiently strong for the optically thick spectrum to reach the non-thermal source function before it turns over. Note that these figures show synchrotron spectra, neglecting the Comptonized component that will inevitably develop.

We see that the presence of non-thermal electrons strongly amplifies the synchrotron emission. Not only the self-absorbed part of the spectrum becomes more prominent but also optically thin emission may contribute significantly to the synchrotron luminosity, provided the power-law tail in the electron distribution is sufficiently hard.

However, strong synchrotron self-absorption acts as a thermalization mechanism for electrons of $\gamma \lesssim \gamma_t$, i.e. in the regime of optically thick emission. Then a question arises whether it will allow for an electron distribution deviating substantially from a pure Maxwellian for $\gamma \sim \gamma_t$. This issue was addressed by Ghisellini et al. (1988), who have shown that an initial power-law distribution of injected electrons will develop (after the thermalization time scale equal to a few synchrotron cooling time scales, t_c^{syn} , defined for the mean energy of the electrons radiating in the optically thick range of the spectrum) into a Maxwellian stationary distribution for $\gamma < \gamma_t$, provided the synchrotron cooling dominates and $t_c^{\text{syn}} \ll t_{\text{esc}}$ (where t_{esc} is the electron escape time from the source). Assuming equipartition of magnetic field pressure with gas pressure, we find the latter criterion to be always fulfilled in accretion flows onto black holes, independent of the form of the injected distribution.

However, when the inverse Compton process is dominant as a cooling mechanism, both γ_{nth} and kT_e diminish and a power-law tail starting below γ_t is formed, see Ghisellini & Svensson (1990). A sufficient condition for the dominance of Compton cooling is $\alpha < 1$, which is typically fulfilled in astrophysical accreting black holes. Even when $\alpha > 1$, Comptonization of external soft photons (e.g. from a cold accretion disk) can dominate electron cooling (see, e.g., Ghisellini et al. 1998). Thus, $\gamma_{\text{nth}} < \gamma_t$ is a likely condition in those sources.

4.2.2 Turnover frequency

Let $\bar{\eta}_\nu(\gamma)$ be the synchrotron emission coefficient of a single electron averaged both over the electron velocity direction and the direction of emission [compare with equation (3.1), where angle-dependent emission coefficient was introduced]. Then, the absorption coefficient for an isotropic distribution of electrons in a chaotic magnetic field is (e.g. Ghisellini & Svensson 1991)

$$\alpha_\nu = \frac{-1}{2m_e\nu^2} \int_1^\infty \gamma (\gamma^2 - 1)^{\frac{1}{2}} \bar{\eta}_\nu(\gamma) \frac{d}{d\gamma} \left[\frac{n_e(\gamma)}{\gamma(\gamma^2 - 1)^{\frac{1}{2}}} \right] d\gamma. \quad (4.4)$$

Let us assume a homogenous spherical source of the radius R and the Thomson optical depth τ_T . We can numerically calculate the absorption coefficient with equation (4.4) for the distribution of equation (4.1) and then solve equation (3.20) for the turnover frequency, ν_t^{nth} . This, in general, involves numerical calculations. We can, however, obtain an analytical estimate, ν_t^{pl} , of the turnover frequency for the hybrid electron distribution by considering a purely power-law electron distribution normalized to match the Maxwellian at γ_{nth} . For that purpose we use the synchrotron absorption coefficient for power-law distribution of relativistic electrons (Rybicki & Lightman 1979),

$$\alpha_\nu^{\text{pl}} = 3^{\frac{1+p}{2}} 8^{-1} \pi^{\frac{1}{2}} G_1 r_e c n_e (\gamma_{\text{nth}}) \gamma_{\text{nth}}^p \nu_c^{\frac{2+p}{2}} \nu^{-\frac{p+4}{2}}, \quad (4.5)$$

where

$$G_1 = \frac{\Gamma(\frac{6+p}{4}) \Gamma(\frac{2+3p}{12}) \Gamma(\frac{22+3p}{12})}{\Gamma(\frac{8+p}{4})} \simeq 1. \quad (4.6)$$

Employing equation (3.20) we obtain:

$$\nu_t^{\text{pl}} = 3^{\frac{1+p}{4+p}} 2^{-\frac{6}{4+p}} \pi^{\frac{1}{4+p}} \nu_c^{\frac{2+p}{4+p}} [G_1 R r_e c n_e (\gamma_{\text{nth}}) \gamma_{\text{nth}}^p]^{\frac{2}{4+p}}, \quad (4.7)$$

which, with equation (4.2), leads to

$$\nu_t^{\text{pl}} \simeq 3^{\frac{1+p}{4+p}} 2^{-\frac{6}{4+p}} \pi^{\frac{1}{4+p}} \nu_c^{\frac{2+p}{4+p}} \left(\frac{\gamma_{\text{nth}}}{p-2} - \frac{1}{p-1} \right)^{-\frac{2}{4+p}} \left(\frac{6 + 15\Theta G_1 r_e c \tau_T \delta \Theta \gamma_{\text{nth}}^{p-1}}{4 + 5\Theta \sigma_T} \right)^{\frac{2}{4+p}}. \quad (4.8)$$

Provided $p \gtrsim 3$ (so that the effect of γ_f is negligible) and emission at ν_t^{nth} is dominated by non-thermal electrons (i.e. $\gamma_f > \gamma_t > \gamma_{\text{nth}}$, which condition can be checked a posteriori by comparing the source function of power-law electrons to the Rayleigh-Jeans intensity), we have $\nu_t^{\text{nth}} \simeq \nu_t^{\text{pl}}$. On the other hand, $\nu_t^{\text{pl}} < \nu_t^{\text{th}}$ when emission from thermal electrons is significant at ν_t^{nth} and, in general,

$$\nu_t^{\text{nth}} \simeq \max(\nu_t^{\text{th}}, \nu_t^{\text{pl}}). \quad (4.9)$$

The accuracy of this approximation is typically $\lesssim 10$ per cent (provided $\gamma_t < \gamma_f$ and $p \gtrsim 3$). The accuracy of approximations to the thermal turnover frequency was discussed in Section 3.1.3.

We can obtain the dependences of $\nu_t^{\text{nth}}/\nu_t^{\text{th}}$ on the plasma parameters by considering the ratio $\nu_t^{\text{pl}}/\nu_t^{\text{th}}$ [given by approximations (4.7) and (3.23)]. First, at constant δ , this ratio decreases with increasing Θ since then γ_{nth} increases with Θ [see equation (4.3)]. The dependence on τ_T is stronger for ν_t^{pl} than for ν_t^{th} as a result of much steeper optically thin synchrotron spectrum in the latter case. This leads to $\nu_t^{\text{pl}}/\nu_t^{\text{th}} \propto \tau_T^{2/(4+p)-0.05}$, i.e. the larger the optical depth, the larger the ratio $\nu_t^{\text{pl}}/\nu_t^{\text{th}}$.

In a hot accretion flow or a corona we generally expect τ_T increasing and Θ decreasing with increasing luminosity, so the effect of a non-thermal tail (of a given form) on the value of the turnover frequency can be expected to be the largest for the most luminous sources.

Since $\nu_t^{\text{pl}}/\nu_t^{\text{th}} \propto \nu_c^{(2+p)/(4+p)-0.91}$, the non-thermal increase of the turnover frequency grows with decreasing ν_c . This effect is due to the increase of γ_t with decreasing ν_c [as a result of increasing ν_t^{th}/ν_c , see equation (3.23)], which leads to a much larger ratio of the number of non-thermal to thermal electrons at γ_t for a given γ_{nth} . Thus, the effect of a non-thermal tail of a given form will be much stronger in AGNs than in BHBs (due to much weaker magnetic field, i.e. smaller ν_c , in the former objects).

Figure 4.3 shows the values of $\nu_t^{\text{nth}}/\nu_t^{\text{th}}$ as a function of $(\gamma_{\text{nth}} - 1)/\Theta$ for three sets of thermal plasma parameters. In the first and second set, we assume parameters relevant for luminous BHBs, $\tau_T=1$, $R = 3 \times 10^7$ cm, $B = 10^7$ G, and $\Theta = 0.1$ and 0.2 , respectively. In the third set, we assume parameters relevant to AGNs, $\tau_T=1$, $R = 3 \times 10^{14}$ cm, $B = 10^3$ G and $\Theta = 0.1$. For each set, we consider two different slopes of the non-thermal tail, $p = 3$ and 4 and $\gamma_f = 30$. Additionally, we consider the cases of $\gamma_f = 10$ and 100 for $p = 3$ (for $p > 3$ the influence of the cut-off is much weaker). We see that even a weak non-thermal component, with $(\gamma_{\text{nth}} - 1)/\Theta \sim 12$ (which corresponds to only ~ 1 per cent of the total energy density of the electrons in the non-thermal tail) can lead to an increase of the turnover frequency by a factor of ~ 1.5 – 2 for BHBs and ~ 10 for AGNs.

The dependence of the relative increase of the turnover frequency on p and γ_f is relatively weak. This reflects the fact that the turnover frequency depends mostly on the number of electrons at γ_t and since for small values of δ , γ_t is only slightly larger than γ_{nth} , $n_e(\gamma_t)$ depends weakly on either p or γ_f . This suggests that the degree of the dependence on p and γ_f should increase with increasing $\nu_t^{\text{nth}}/\nu_t^{\text{th}}$, in agreement with our results. It is important to note that weak dependence of $\nu_t^{\text{nth}}/\nu_t^{\text{th}}$ on the shape of the non-thermal tail implies that our predictions are weakly dependent on details of the acceleration mechanism.

4.3 Hybrid synchrotron self-Comptonization

With the presence of non-thermal electrons in the plasma, the process of Comptonization will be modified with respect to the thermal case in two ways.

First, Compton scattering itself will involve thermal electrons as well as non-thermal ones. The effect of non-thermal electrons on Comptonization will be most prominent at energies $x \gg \Theta$, where a high-energy tail (above the thermal cut-off) will develop. Second, the seed-photon flux will be much higher (see Figure

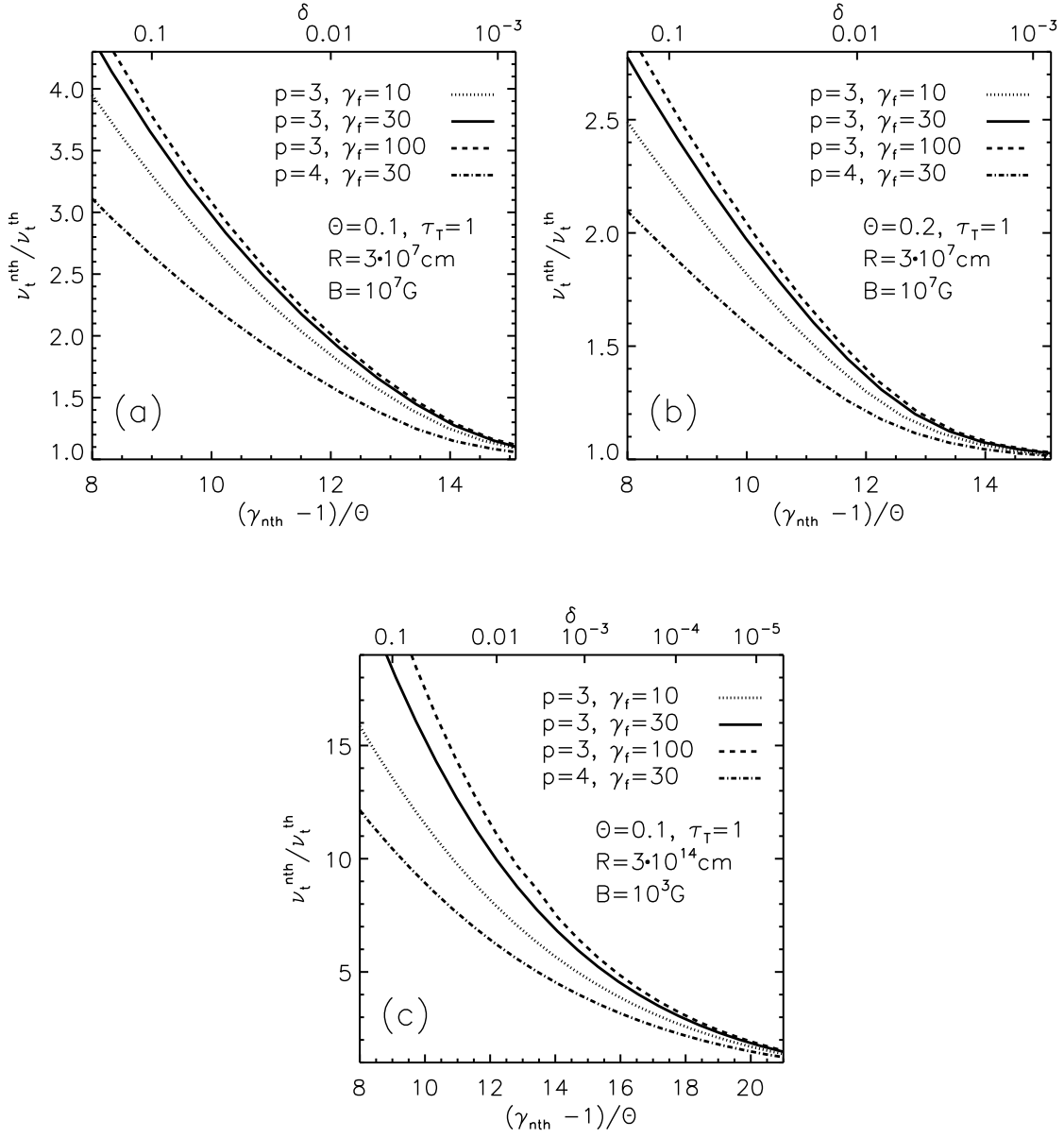


Figure 4.3: The increase of ν_t as a function of the electron energy where the non-thermal tail starts for various plasma parameters and forms of the tail. The upper axis shows the values of δ for $p = 3$ and $\gamma_f = 30$. Note that the relation between $(\gamma_{\text{nth}} - 1)/\Theta$ and δ is slightly different for the curves with different values of p and γ_f , see Figure 4.1.

4.2), so that the luminosity in the thermal Comptonization spectrum will increase correspondingly. As we have seen, even if a tiny fraction of the total electron energy is carried by non-thermal electrons, which only weakly modifies the shape of the Comptonization spectrum, the seed photon flux can be increased by a large factor. The second effect is thus much stronger for the cases we consider.

We investigate the above two effects separately, first by calculating the luminosity from Comptonization by a hybrid electron distribution in the general case (without specifying the soft photons source) and then by determining the amplification of the CS luminosity due to the increase of the luminosity of hybrid synchrotron emission, compared to the thermal case.

4.3.1 Comptonization by a hybrid electron distribution

In Section 3.2 we presented an analytical model describing the thermal Comptonization spectrum. Below we extend those results so as to calculate the Comptonization luminosity in the hybrid case. We now denote the thermal-Compton luminosity of a uniform, spherical source as [compare to equation (3.36)]

$$L_C^{\text{th}}(\mathcal{C}) \simeq 4\pi R^2 \mathcal{C} \Theta \left[\Gamma \left(1 - \alpha, \frac{x_{\text{inj}}}{\Theta} \right) + \frac{6\Gamma(\alpha)P_{\text{sc}}}{\Gamma(2\alpha + 3)} \right], \quad (4.10)$$

where \mathcal{C} is a constant depending on the flux of the injected seed photons. For now we do not put any constraints on the seed photon flux.

For the electron distributions we consider (i.e. $\tau_T \sim 1$ and $\delta \ll 1$) the Thomson optical depth for scattering off non-thermal electrons is much smaller than unity and thus the resulting spectrum can be approximated as a convolution of the thermal Comptonization spectrum with a spectrum resulting from single scattering of photons off non-thermal electrons. Therefore, for $x \lesssim \Theta$, the Comptonization spectrum becomes harder, while for $x \gg \Theta$, above the thermal cut-off, a power-law tail in the spectrum develops. As a result, the overall luminosity produced by Comptonization increases.

In calculations of the luminosity from Comptonization by non-thermal electrons, L_C^{pl} , where the Klein-Nishina effect has to be taken into account, we use the approximation for the rate of energy change, $d\gamma/dt$, of a single electron via Compton interaction with isotropic photons of energy density, U_{ph} , and mean energy, $\langle x \rangle$,

$$\frac{d\gamma}{dt} = -\frac{4}{3} \frac{\sigma_T (\gamma^2 - 1) U_{\text{ph}}}{m_e c} \left[1 - \frac{63}{10} \frac{\gamma \langle x^2 \rangle}{\langle x \rangle} \right], \quad (4.11)$$

where the Klein-Nishina cross-section was approximated using the first-order correction to the Thomson-limit cross-section (Rybicki & Lightman 1979). We assume

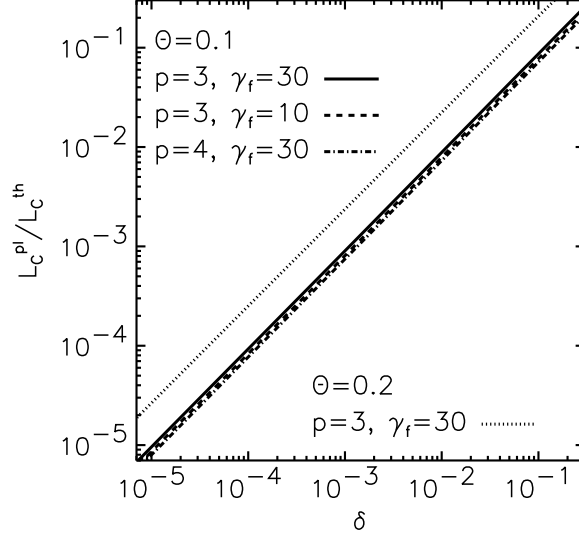


Figure 4.4: The relation between the fraction of energy carried by non-thermal electrons and the ratio of $L_C^{\text{pl}}/L_C^{\text{th}}$ for different plasma parameters and spectral index $\alpha = 0.7$.

that the photons undergoing scattering off non-thermal electrons are those from the thermal Comptonization spectrum above x_{inj} . Then

$$U_{\text{ph}}(x) = \frac{3 (dL_C^{\text{th}}/dx) (3/4 + \tau_{\text{T}}/5)}{4\pi c R^2}, \quad (4.12)$$

where the factor $(3/4 + \tau_{\text{T}}/5)$ accounts for the change of the escape time due to scatterings in the source and is a matching formula between the optically thin case (where the escape time is $3R/4c$) and the optically thick one ($\tau_{\text{T}}R/5c$, Sunyaev & Titarchuk 1980). We can further simplify the calculations assuming that the spectrum of photons undergoing non-thermal Comptonization is a pure power-law and then neglect scatterings in the Klein-Nishina limit (see below).

Now, for each γ we calculate U_{ph} , $\langle x \rangle$ and $\langle x^2 \rangle$ as an integral over the power-law spectrum from x_{inj} up to the energy, x_{max} , which is the limit of the Klein-Nishina regime and which we obtain from the condition of $1 - 63/(10\gamma x_{\text{max}}) = 0$, where the numerical coefficient is chosen for consistency with equation (4.11).

Then the formula (4.11) is integrated over $n_e(\gamma)$, from γ_{nth} to infinity, which leads to

$$L_C^{\text{pl}}(\mathcal{C}) = \frac{16\pi}{3} \left(\frac{10}{63}\right)^{1-\alpha} \frac{6 + 15\Theta}{4 + 5\Theta} \left(\frac{3}{4} + \frac{\tau_{\text{T}}}{5}\right) \frac{R^2 \mathcal{C} \delta \tau_{\text{T}} \Theta^{\alpha+1}}{(1-\alpha)(2-\alpha)} \\ \times \left(\frac{\gamma_{\text{nth}}}{p-2} - \frac{1}{p-1}\right)^{-1} \left(\frac{\gamma_{\text{nth}}^{\alpha+1}}{p-\alpha-2} - \frac{\gamma_{\text{nth}}^{\alpha-1}}{p-\alpha}\right), \quad (4.13)$$

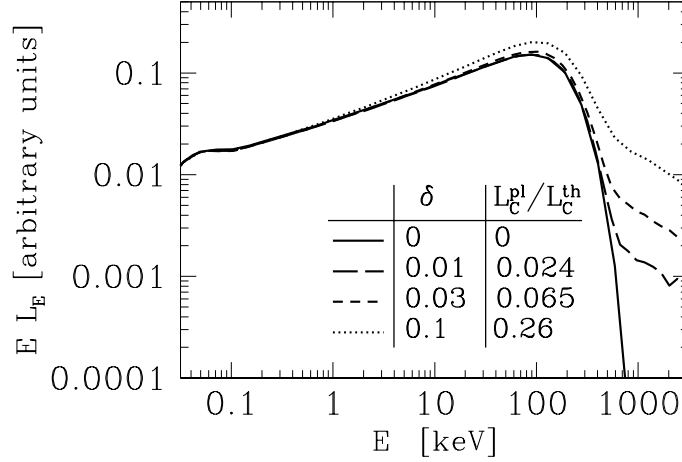


Figure 4.5: Monte Carlo Comptonization spectra of 10-eV blackbody photons in a plasma of $\Theta = 0.1$, $\tau_T = 2.4$. The solid line represents the thermal spectrum, while the other lines correspond to the cases of power-law tails in the electron distribution of $p = 3$, $\gamma_f = 30$ and different values of δ .

where equation (4.2) has been employed.

The total luminosity, $L_C^{\text{th}} = L_C^{\text{th}} + L_C^{\text{pl}}$, as well as the ratio $L_C^{\text{pl}}/L_C^{\text{th}}$ can now be directly obtained from expressions (4.10) and (4.13). In the range of $0.4 \lesssim \alpha \lesssim 0.9$, the high-energy part of the power law component dominates the luminosity while the Wien component can still be neglected. Then, we obtain

$$\begin{aligned} \frac{L_C^{\text{pl}}}{L_C^{\text{th}}} &\approx \frac{4}{3} \left(\frac{10}{63} \right)^{1-\alpha} \frac{6 + 15\Theta}{4 + 5\Theta} \left(\frac{3}{4} + \frac{\tau_T}{5} \right) \frac{\delta \tau_T \Theta^\alpha}{2 - \alpha} \\ &\times \left(\frac{\gamma_{\text{nth}}}{p-2} - \frac{1}{p-1} \right)^{-1} \left(\frac{\gamma_{\text{nth}}^{\alpha+1}}{p-\alpha-2} - \frac{\gamma_{\text{nth}}^{\alpha-1}}{p-\alpha} \right). \end{aligned} \quad (4.14)$$

From Monte Carlo simulations of Comptonization processes, produced with the code of Gierliński (2000), which we adapted for hybrid electron distributions, we found that the accuracy of this approximation is typically $\lesssim 30$ per cent. Figure 4.4 shows that while the ratio $L_C^{\text{pl}}/L_C^{\text{th}}$ depends strongly on δ , the dependence on the non-thermal tail shape is very weak. Thus, also the estimates of the hybrid Comptonization luminosity are weakly dependent on the details of the acceleration processes producing the hybrid distribution.

In Figure 4.5 we show as an example Comptonization spectra (of blackbody photons) from a homogenous plasma cloud, obtained from Monte Carlo simulations. We see that as long as $\delta < 0.1$ the Comptonization spectrum at $x \lesssim \Theta$ is hardly modified by the presence of non-thermal electrons and the onset of the power-law tail is no higher than an order of magnitude below the peak in the $xL(x)$ spectrum.

From the observational point of view, an important feature measuring the deviation from purely thermal Comptonization spectrum is the fraction of the luminosity radiated in the high-energy tail beyond the thermal spectrum. The ratio $L_C^{\text{pl}}/L_C^{\text{th}}$ is larger than this fraction as it incorporates also the non-thermal luminosity at energies below the tail. This effect is stronger for smaller δ , when a larger fraction of L_C^{pl} is hidden below the thermal peak. For example, in the spectra in Figure 4.5 corresponding to $\delta = 0.1$ and $\delta = 0.01$, the high-energy tail develops at ~ 300 and ~ 500 keV, respectively. Then $L_C^{\text{pl}}/L_C^{\text{th}}$ is larger than the fraction of the luminosity in the tail by factors 3 and 5, respectively. Thus, $L_C^{\text{pl}}/L_C^{\text{th}}$ provides only an upper limit to the fraction of the luminosity radiated in the high-energy tail.

4.3.2 Hybrid synchrotron emission as seed photons

As we have seen above (Figure 4.2), the presence of a non-thermal component in the thermal distribution of electrons in a plasma where synchrotron radiation is produced and then Comptonized, increases the flux of soft photons (compared to the thermal case) both from optically thick emission up to x_t^{nth} and from optically thin emission above x_t^{nth} .

In the case of purely thermal CS process, the normalization of the Comptonization spectrum can be assumed (Zdziarski 1985, 1986) to be proportional to the Rayleigh-Jeans flux at the turnover frequency [see equation (3.30)], so that the constant \mathcal{C} in the expression (4.10), which we now denote as \mathcal{C}^{th} , reads

$$\mathcal{C}^{\text{th}} = \frac{2\pi m_e c^3}{\lambda_C^3} \varphi \Theta^{1-\alpha} (x_t^{\text{th}})^{2+\alpha}. \quad (4.15)$$

The total luminosity from the CS process is then

$$L_{\text{CS}}^{\text{th}} = L_S^{\text{th}} + L_C^{\text{th}}(\mathcal{C}^{\text{th}}), \quad (4.16)$$

which expression corresponds to equation (3.35).

In general, the total luminosity of the CS process in the hybrid case will be then

$$L_{\text{CS}}^{\text{nth}} = L_S^{\text{nth}} + L_C^{\text{th}}(\mathcal{C}^{\text{nth}}) + L_C^{\text{pl}}(\mathcal{C}^{\text{nth}}), \quad (4.17)$$

where L_S^{nth} is the hybrid synchrotron luminosity and \mathcal{C}^{nth} is the normalization constant for seed photons produced by hybrid synchrotron emission.

The amplification of the CS luminosity will depend significantly on which of the terms on the right-hand-side of equation (4.16) dominates. First let us consider the case of a soft spectrum, when $L_S^{\text{th}} \gtrsim L_C^{\text{th}}$, which corresponds to the spectral index $\alpha > 1$, i.e. to small value of τ_T in our case. The luminosity from the first-order Compton scattering is proportional to the synchrotron emission, while contribution

to the luminosity from higher-order scatterings is much smaller. Therefore the ratio of CS luminosities can be well approximated by the ratio of synchrotron luminosities, i.e.

$$\frac{L_{\text{CS}}^{\text{nth}}}{L_{\text{CS}}^{\text{th}}} \approx \frac{L_{\text{S}}^{\text{nth}}}{L_{\text{S}}^{\text{th}}}. \quad (4.18)$$

To calculate the ratio (4.18) we assume the optically thick hybrid synchrotron emission below $x_{\text{t}}^{\text{nth}}$ to be proportional to S_x^{pl} , the source function of power-law electrons,

$$S_x^{\text{pl}} = \frac{1}{2} \frac{G_2}{3^{1/2}} \frac{m_e c^3}{G_1 \lambda_{\text{C}}^3} x_c^{-\frac{1}{2}} x^{\frac{5}{2}}, \quad (4.19)$$

where

$$G_2 = \frac{\Gamma(\frac{5+p}{4})\Gamma(\frac{3p+19}{12})\Gamma(\frac{3p-1}{12})}{\Gamma(\frac{7+p}{4})} \simeq 1. \quad (4.20)$$

The emission above $x_{\text{t}}^{\text{nth}}$ is $\propto x^{-(p-1)/2}$ and then we have

$$\frac{L_{\text{S}}^{\text{nth}}}{L_{\text{S}}^{\text{th}}} = \frac{3^{\frac{1}{2}}(p+4)G_2 (x_{\text{t}}^{\text{nth}}/x_c)^{7/2}}{14(p-3)G_1\Theta (x_{\text{t}}^{\text{th}}/x_c)^3}. \quad (4.21)$$

Then, with the use of equation (4.18) we would have approximately:

$$\frac{L_{\text{CS}}^{\text{nth}}}{L_{\text{CS}}^{\text{th}}} \approx \frac{3^{\frac{1}{2}}(p+4) (x_{\text{t}}^{\text{nth}}/x_c)^{7/2}}{14(p-3)\Theta (x_{\text{t}}^{\text{th}}/x_c)^3}. \quad (4.22)$$

Now let us assume $\alpha \leq 1$. In this case most of the luminosity is produced in the Comptonization spectrum, by higher-order scatterings, and the synchrotron luminosity itself is negligible, i.e. $L_{\text{S}}^{\text{th}} \ll L_{\text{C}}^{\text{th}}$.

If the seed photons for Comptonization were monoenergetic, the normalization of the Comptonization spectrum, and thus its luminosity, would be simply proportional to the total number density of soft photons. The same would hold approximately if the soft photons were not monoenergetic, but their spectrum had a sharp peak, as in the case of self-absorbed synchrotron emission. However, for hybrid synchrotron emission, not only the soft photon luminosity becomes larger than in the thermal case, but also typical photon energy increases from x_{t}^{th} to $x_{\text{t}}^{\text{nth}}$. This shifts the Comptonization spectrum, which affects its normalization in a way dependent on the spectral index. Having taken this into account we find that the ratio of normalization constants of Comptonization spectra reads

$$\frac{\mathcal{C}^{\text{nth}}}{\mathcal{C}^{\text{th}}} = \frac{N_{\text{S}}^{\text{nth}}}{N_{\text{S}}^{\text{th}}} \left(\frac{x_{\text{t}}^{\text{nth}}}{x_{\text{t}}^{\text{th}}} \right)^{\alpha}, \quad (4.23)$$

where $N_{\text{S}}^{\text{nth}}$ and N_{S}^{th} are photon densities integrated over hybrid and thermal synchrotron spectra, respectively.

We calculated this ratio using the same approximations as above, obtaining

$$\frac{\mathcal{C}^{\text{nth}}}{\mathcal{C}^{\text{th}}} = \frac{G_2(p+4) (x_t^{\text{nth}}/x_c)^{5/2+\alpha}}{5 \cdot 3^{1/2} G_1(p-1) \Theta (x_t^{\text{th}}/x_c)^{2+\alpha}}. \quad (4.24)$$

Since we can neglect the contribution of synchrotron luminosity to the total CS luminosity in this case, we have

$$\frac{L_{\text{CS}}^{\text{nth}}}{L_{\text{CS}}^{\text{th}}} = \frac{\mathcal{C}^{\text{nth}}}{\mathcal{C}^{\text{th}}} \left[1 + \frac{L_{\text{C}}^{\text{pl}}(\mathcal{C}^{\text{th}})}{L_{\text{C}}^{\text{th}}(\mathcal{C}^{\text{th}})} \right], \quad (4.25)$$

and if δ is sufficiently small, in which case $L_{\text{C}}^{\text{pl}}(\mathcal{C}^{\text{th}}) \ll L_{\text{C}}^{\text{th}}(\mathcal{C}^{\text{th}})$, we can neglect the last term in the square brackets. Then, the ratio of hybrid and thermal CS luminosities would be approximately

$$\frac{L_{\text{CS}}^{\text{nth}}}{L_{\text{CS}}^{\text{th}}} \approx \frac{(p+4) (x_t^{\text{nth}}/x_c)^{5/2+\alpha}}{5 \cdot 3^{1/2} (p-1) \Theta (x_t^{\text{th}}/x_c)^{2+\alpha}}. \quad (4.26)$$

The above expressions were derived using the emission and absorption coefficients for power-law electrons (e.g. Rybicki & Lightman 1979). Since we neglected the cut-off in the electron distribution, the above approximations hold for $x_t^{\text{nth}}/x_c \ll \gamma_f^2$, i.e. when the contribution from electrons with $\gamma > \gamma_f$ to the emission at x_t^{nth} can be neglected.

We also note that these approximations do not have the correct thermal limit when $\gamma_{\text{nth}} \gg \gamma_t$, i.e. when $x_t^{\text{nth}} \approx x_t^{\text{th}}$ (see Figure 4.2b, where a synchrotron spectrum for such a case is shown). For harder power-law electron distributions ($p \lesssim 3$), for which our approximations do not hold (since seed photons cannot be approximated as monoenergetic), the amplification of CS luminosity will be even larger than that predicted above.

Chapter 5

Synchrotron self-Comptonization in accretion flows

In previous Chapters we developed a model of self-Comptonized synchrotron emission in thermal and hybrid semi-relativistic plasmas. We are now ready to apply our results to models of accretion flows.

At present the quality of observational data does not allow for definite discriminating between various accretion flow models, even for the most luminous objects. This concerns in particular hard X-ray and γ -ray data which are crucial for our estimates of the role of Comptonized synchrotron emission. Another reason for difficulties in discriminating between different models is our limited understanding of physical processes taking place in accretion flows, which we discussed in Chapter 1.

As a result, it is difficult to test observationally advanced theoretical models of accretion flows, while models that proved to be successful in reproducing observational results are often to some extent phenomenological.

Keeping this in mind, we introduce below two rather simplified accretion flow models (though they base on results of more advanced theoretical investigations), which however allow for direct comparisons of their predictions with the spectra of accreting black holes we have at our disposal. The two models are a two-temperature, optically thin hot accretion flow and a model of active regions above a cold disc, both of which were sketched in Section 1.3.3.

Following the logical scheme of the previous two Chapters, we first investigate the model predictions in the thermal case and test them against observations of four accreting black holes, Cygnus X-1, GX 339-4, NGC 4151 and NGC 4258. Then, we check how the results are modified in the hybrid case, taking into account observational constraints on the hybrid electron population obtained for Cygnus X-1 and GX 339-4. Finally, we present and discuss observational constraints on the

magnetic field strength for the two models and explore possible relation between the optical and X-ray emission in GX 339-4.

5.1 Thermal CS emission

5.1.1 Hot accretion flow model

Here, we consider CS emission from an optically thin, two-temperature accretion flow. For simplicity we assume spherical geometry, which is sufficient for our purposes. We use below dimensionless units of mass and radius, i.e. $m \equiv M/M_\odot$ and $r \equiv R/R_g$.

In inner parts of hot accretion flows, the ion temperature is typically much higher than the electron temperature (e.g. Shapiro et al. 1976; Narayan & Yi 1995), and the ion energy density is much higher than that of both electrons and radiation. Then, energy density equipartition between magnetic field and gas corresponds to

$$\frac{B^2}{8\pi} = \frac{3}{2} n_e \frac{\mu_e}{\mu_i} kT_i, \quad (5.1)$$

where $\mu_e = 2/(1 + X)$ is the mean electron molecular weight, $\mu_i = 4/(1 + 3X)$ is the mean ion molecular weight and $X (\approx 0.7)$ is the H mass fraction. We note that pressure equipartition, which is often assumed, would result in a slightly different condition.

Maximum possible ion temperatures are sub-virial, and detailed accretion flow models show

$$kT_i \approx \frac{\delta_M m_p c^2}{r}, \quad (5.2)$$

where m_p is the proton mass and $\delta_M \ll 1$ (Shapiro et al. 1976; Narayan & Yi 1995). In particular, δ_M constant with r and dependent on the flow parameters is obtained in the self-similar advection-dominated solution of Narayan & Yi (1995). Close to the maximum possible accretion rate of the hot flow, $\delta_M \sim 0.2$ is a typical value [see equation (2.16) in Narayan & Yi (1995)], which we adopt in numerical calculations below.

However, the self-similar solution breaks down in the inner flow, which results in values of T_i much lower than that given by the self-similar solution, e.g., by a factor of ~ 10 at $r = 6$ (Chen et al. 1997). Thus, we can obtain an upper limit on the equipartition magnetic field strength by assuming that it follows the self-similar solution above some radius, $r_0 \sim 20$, while it remains constant at $r < r_0$,

$$B \simeq 7.3 \times 10^8 \text{ G} \left(\frac{\delta_M \tau_T}{m} \right)^{1/2} \times \begin{cases} 1/r_0, & r \leq r_0; \\ 1/r, & r > r_0. \end{cases} \quad (5.3)$$

This typically gives $B \lesssim 10^7$ G in inner regions of accretion flows in BHs and $B \lesssim 10^4$ G in AGNs.

Then, the CS luminosity can be estimated as a sum of contributions from the inner region (assumed here to be spherical) within radius r_0 , and from the outer region, $r > r_0$, obtained here by radial integration from r_0 to infinity (for which we assumed a planar geometry). We note that the maximum of dissipation per logarithm of radius in the Schwarzschild metric occurs at $r \sim r_0 \sim 20$. We use here the value of B from equation (5.3) for $r \leq r_0$ and assume for simplicity α and Θ constant through the flow.

For $0.4 \lesssim \alpha \lesssim 0.9$, the resulting ratio of the CS luminosity to the Eddington one is

$$\frac{L_{\text{CS}}^{\text{th}}}{L_{\text{E}}} \approx \frac{43 \times 10^{-2.83\alpha} \delta_{\text{M}}^{0.91+0.46\alpha} \Theta^{2.64-0.68\alpha} \varphi}{(mr_0^2)^{0.46\alpha-0.09} (1-\alpha)\alpha^{0.63\alpha+1.26}} \times \begin{cases} 1 & \text{for inner region;} \\ (0.91\alpha - 0.18)^{-1} & \text{for outer region,} \end{cases} \quad (5.4)$$

where we used equations (3.28), (3.38), (5.3) and $\varphi \sim 0.5$. The total $L_{\text{CS}}^{\text{th}}$ corresponds to the sum of the contributions from the two regions. In the case of $\alpha \gtrsim 1.1$, we have correspondingly

$$\frac{L_{\text{CS}}^{\text{th}}}{L_{\text{E}}} \approx \frac{0.021 \delta_{\text{M}}^{1.37} \Theta^{1.96}}{m^{0.37} r_0^{0.73} \alpha^{1.89}} \left(1 + \frac{3\varphi}{\alpha - 1} \right) \times \begin{cases} 1 & \text{for inner region;} \\ 1.37 & \text{for outer region,} \end{cases} \quad (5.5)$$

which is based on equation (3.39).

It is important to note that with the above assumptions the presented expressions for $L_{\text{CS}}^{\text{th}}$ should be treated as upper limits on the available luminosity from the accretion flow. First of all because the assumed field strength is the maximum one. Also both τ_{T} and Θ will most likely decrease with r in an accretion flow. Therefore our correction for the emission from the outer part of the disc will overestimate the true value. This correction, however, is at most of the same order as the emission from within r_0 . Thus, the most important factors determining the available CS luminosity are temperature and spectral index (both values derived from observations) and the assumed magnetic field strength. We make use of this fact for obtaining constraints on the magnetic field strength in Section 5.2.

We see from equations (5.4)–(5.5) that the predicted Eddington ratio decreases with the mass. Then, if the thermal CS process dominated, the predicted X-ray spectra would harden with increasing M at a given $L_{\text{CS}}^{\text{th}}/L_{\text{E}}$. In fact, the *opposite* trend is observed; black-hole binaries have X-ray spectra harder on average than those of AGNs (e.g. Zdziarski et al. 1999), implying that either the CS process does not dominate the X-ray spectra of those objects or (less likely) the Eddington ratio is much lower on average in AGNs than in black-hole binaries.

Our calculations are in a good agreement with the dependences on m in the results of Mahadevan (1997) and are qualitatively different from a statement in Narayan & Yi (1995) that hot accretion flows with CS cooling are effectively mass-invariant, which conclusion appears erroneous.

We find that, under conditions typical to compact sources, the Comptonized bremsstrahlung luminosity, L_{CB} , is often comparable to or higher than L_{CS}^{th} . Figure 5.1 shows the results of numerical calculations of the Eddington ratio for both CS and bremsstrahlung radiation as a function of the spectral index of the CS radiation, α , for $m = 10$ and 10^8 . To enable direct comparison of those two components, we show the luminosity from the inner region (with constant B) only, assuming $r_0 = 20$ and $\delta_M = 0.2$. Thick and thin curves give L_{CS}^{th} and L_{CB} [see equation (3.40) with $r = r_0$], respectively. The relative importance of bremsstrahlung increases with increasing mass and size, e.g. $L_{CB}/L_{CS}^{\text{th}} \propto m^{0.46\alpha - 0.09} r_0^{0.91\alpha + 0.82}$ and $L_{CB}/L_{CS}^{\text{th}} \propto m^{0.37} r_0^{1.73}$ for $\alpha \lesssim 0.9$ and $\gtrsim 1.1$, respectively. Note that L_{CB} decreases with increasing Θ at a constant α , which is an effect of a strong dependence of L_{CB} on τ_T (increasing with decreasing Θ) and a weak dependence of L_{CB} on temperature. Also, an important conclusion from Figure 5.1 is that Eddington ratios $\gtrsim 0.01$ can be obtained from this process only for very hard spectra and high electron temperatures, with this constraint being significantly stronger in the case of AGNs.

Figure 5.2 compares the upper limits on L_{CS}^{th}/L_E with values of L/L_E inferred from observations for a number of objects and with the corresponding luminosity from bremsstrahlung. The shown values of L_{CS}^{th} include the contributions from both the inner and the outer region of the flow [equation (5.3)] for $r_0 = 20$ and $\delta_M = 0.2$. On the other hand, the shown values of L_{CB} are for emission from within r_0 only, and the expected actual L_{CB} will be by a factor of ~ 2 larger.

For Cygnus X-1 in the hard state, we used the brightest spectrum of Gierliński et al. (1997), with $\alpha = 0.6$, $\Theta = 0.2$, and $L \approx 3 \times 10^{37}$ erg s $^{-1}$ (assuming the distance of $D = 2$ kpc, Massey, Johnson & DeGioia-Eastwood 1995; Malysheva 1997) and $m = 10$.

The values we assumed for GX 339-4 in the hard state were $\alpha = 0.75$, $\Theta = 0.1$, $L \approx 3 \times 10^{37}$ erg s $^{-1}$, $D = 4$ kpc and $m = 10$ (though the mass is not constrained observationally), see Chapter 2.

In the case of NGC 4151, we used the brightest spectra observed by *Ginga* and *CGRO/OSSE* (Zdziarski, Johnson & Magdziarz 1996), for which $\alpha = 0.85$, $\Theta = 0.1$, and $L \approx 9 \times 10^{43}$ erg s $^{-1}$, assuming $D = 16.5$ Mpc (corresponding to $H_0 = 75$ km s $^{-1}$ Mpc $^{-1}$), and $m = 4 \times 10^7$ (Clavel et al. 1987).

For NGC 4258 we adopted $L = 2 \times 10^{41}$ erg s $^{-1}$ from an extrapolation of the 2–10 keV luminosity of $L_{2-10\text{keV}} = 3.1 \times 10^{40}$ erg s $^{-1}$ with $\alpha = 0.78$ (Makishima et al. 1994) up to 200 keV, $D = 6.4$ Mpc and $m = 3.6 \times 10^7$ (Miyoshi et al. 1995). Finally,

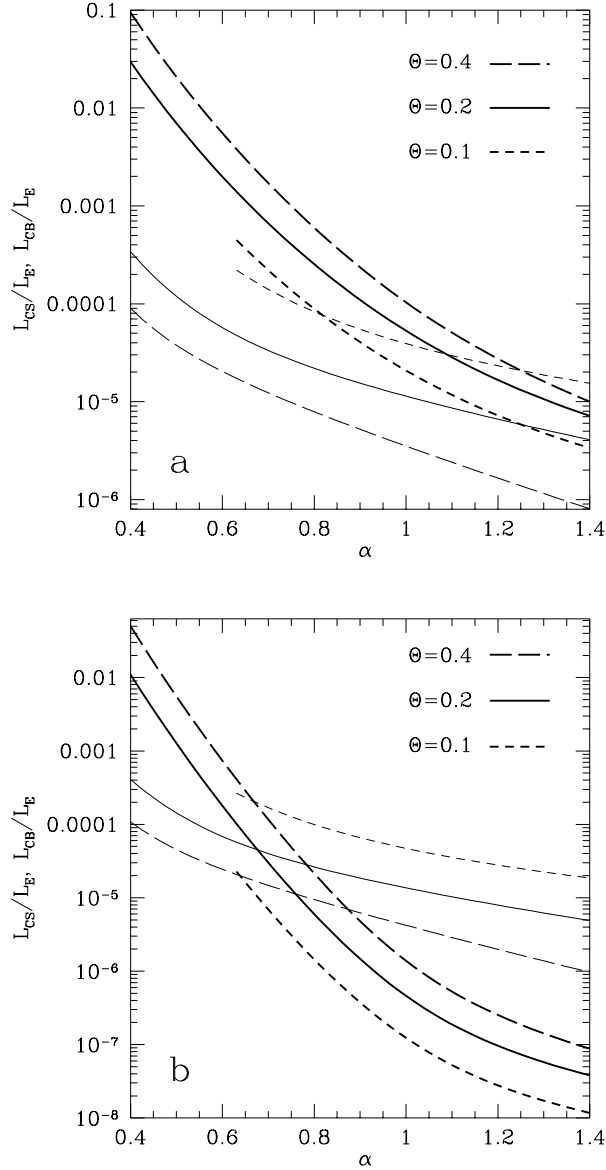


Figure 5.1: The Eddington ratio as a function of the spectral index of CS radiation for three values of electron temperature and for masses (a) $m = 10$, and (b) $m = 10^8$. The heavy and thin curves show the luminosity in the CS radiation and in Comptonized bremsstrahlung, respectively. See text for other assumptions. The curves are shown only for values of α corresponding to $\tau_{\text{T}} \leq 3$, as for larger τ_{T} our formulae for α (Section 3.2) break down.

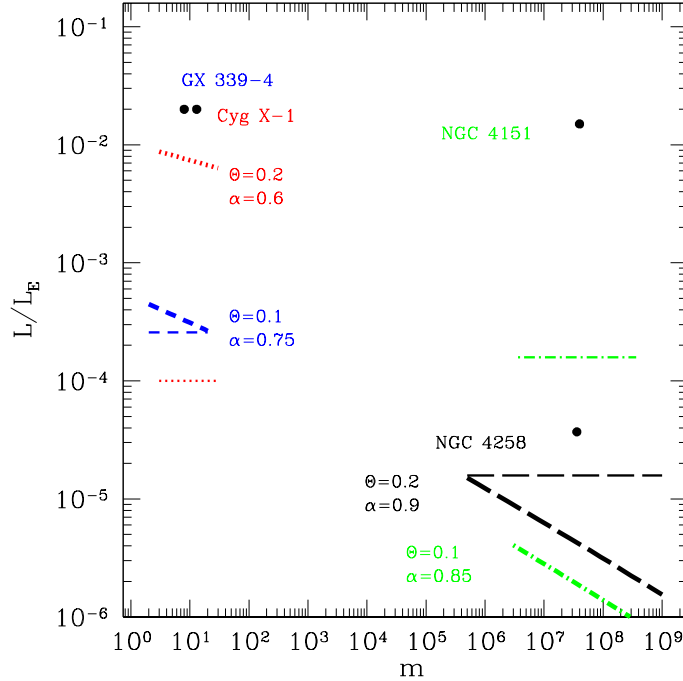


Figure 5.2: Comparison of Eddington ratios inferred from observations (black points; the ones corresponding to Cygnus X-1 and GX 339-4 are slightly displaced for clarity of the display) with the model upper limits from the CS emission (heavy curves labelled by values of Θ and α) for a range of black-hole masses. Curve colours correspond to specific objects, except for NGC 4258, for which no sufficient spectral data exist. Instead, the black model curves for $\Theta = 0.2$, $\alpha = 0.9$, corresponding to the average spectrum of Seyfert 1s, have no corresponding observational point. Thin horizontal lines show the Comptonized bremsstrahlung emission. The magnetic field energy density is in equipartition with ions in a hot accretion flow, see Section 5.1.1.

we show $L_{\text{CS}}^{\text{th}}$ for the average parameters of Seyfert-1 spectra, $\alpha = 0.9$, $\Theta = 0.2$ (e.g. Zdziarski 1999).

We see that only in the case of Cygnus X-1, with its relatively hard spectrum, the CS emission can contribute substantially, at $\lesssim 30$ per cent, to the total luminosity. Given uncertainties of our model, e.g. in the value of δ_{M} , it would be in principle possible that the CS process can account for most of the emission of Cygnus X-1. However, we have adopted here assumptions rather maximizing available synchrotron luminosity and it would be therefore more likely that the thermal CS process is negligible also in Cygnus X-1. Thus, we can conclude that thermal CS emission in the assumed hot-disc geometry is unlikely to be responsible for the observed X-ray spectra of luminous black-hole sources.

To explain those spectra, an additional source of seed photons is required. Such seed photons are naturally provided by blackbody emission of some cold medium (see Section 1.5.3), e.g. an optically-thick accretion disc or cold blobs, co-existing with the hot flow. However, another possibility, as we shall see in Section 5.2, is hybrid synchrotron emission.

On the other hand, the thermal CS process can clearly be important in weaker sources, e.g. NGC 4258. We have compared predictions of our model with the 2–10 keV spectral index and luminosity of this object. We have obtained a good fit to the data, assuming $\delta_M = 0.2$, $\Theta = 0.4$ and taking into account emission within $r_0 = 17$, as shown in Figure 3.6. This yields $L_{CS}^{\text{th}} = 1.8 \times 10^{41} \text{ erg s}^{-1}$ and $L_{CB} = 4 \times 10^{40} \text{ erg s}^{-1}$. A similar spectrum from an advection disc model was obtained by Lasota et al. (1996).

The relatively high temperature, $\Theta \simeq 0.4$, required in our model, is, in fact, consistent with predictions of hot accretion flow models (e.g. Narayan & Yi 1995). For a lower temperature, $\Theta \approx 0.2$ (typical for luminous sources), we could reproduce the $L_{2-10\text{keV}}$ of NGC 4258 as well, but then the 2–10 keV spectrum would be dominated by bremsstrahlung, i.e. much harder than the observed one.

Comptonized bremsstrahlung, with L_{CB}/L_E independent of M , provides the minimum possible luminosity of a plasma with given τ_T , Θ and r . This is shown by horizontal lines in Figure 5.2. Thus, sources with lower luminosities cannot have plasma parameters characteristic of luminous sources, which is indeed consistent with hot accretion flow models, in which τ_T quickly decreases with decreasing L (e.g. Narayan & Yi 1995). On the other hand, CS emission can still be important in a certain energy range above the turnover energy even if $L_{CB} > L_{CS}^{\text{th}}$.

5.1.2 Coronal model - equipartition with radiation energy density

In Section 1.3.3 we mentioned a model in which energy is released via magnetic field reconnection in localized active regions forming a patchy corona above an optically-thick accretion disc. Such a model was considered e.g. by Di Matteo, Celotti & Fabian (1997b) who assumed that the energy density of the magnetic field was in equipartition with that of the local radiation. This corresponds to

$$\frac{B^2}{8\pi} \approx \frac{9}{16\pi} \frac{L}{N(r_b R_g)^2 c}, \quad (5.6)$$

where $r_b R_g$ is the radius of an active blob and N is the average number of blobs. The right-hand-side of this equation represents the average photon density in an optically thin, uniformly-radiating, sphere. This expression yields values of B somewhat

larger than those of Di Matteo et al. (1997b), who used a numerical factor of $1/4\pi$ in their expression for B . Consequently, our estimates of $L_{\text{CS}}^{\text{th}}$ will be slightly higher than those obtained using the formalism of Di Matteo et al. (1997b). We note that in the case of an optically and geometrically thin slab-like reconnection region, the numerical factor above should be $9/12\pi$. Equation (5.6) can be rewritten as

$$B \approx 10^9 \frac{1}{r_{\text{b}}} \left(\frac{\eta}{Nm} \right)^{1/2} \text{G}, \quad (5.7)$$

where $\eta \equiv L/L_{\text{E}}$. We assume hereafter $N = 10$, since variability strength of BHBs suggests that at a given moment there should be ~ 10 active regions present. The characteristic size of a reconnection region has been estimated by Galeev et al. (1979) as

$$r_{\text{b}} \sim h_{\text{d}} \alpha_{\text{v}}^{-1/3}, \quad (5.8)$$

where $h_{\text{d}} R_{\text{g}}$ is the scale height of an underlying optically-thick disc. This typically yields a range of $0.01 \lesssim r_{\text{b}} \lesssim 5$, depending on the disc parameters and increasing with accretion rate (see e.g. Svensson & Zdziarski 1994). It has to be remembered, however, that the specific corona model of Galeev et al. (1979) can power only very weak coronae (Beloborodov 1999) and probably other mechanisms are responsible for formation of luminous coronae (Section 1.5.2). We simply assume $r_{\text{b}} = 2$ in numerical examples below, which value was also used by Di Matteo et al. (1997b).

With the above value of B , we can derive the ratio of the CS luminosity from the corona to the total coronal luminosity,

$$\frac{L_{\text{CS}}^{\text{th}}}{L} \approx \frac{650\varphi(\eta/Nmr_{\text{b}}^2)^{0.46\alpha-0.09}\Theta^{3.78-0.11\alpha}}{10^{2.24\alpha}\alpha^{0.13+0.06\alpha}(1-\alpha)} \quad (5.9)$$

for $0.4 \lesssim \alpha \lesssim 0.9$. The analogous formula for $\alpha \gtrsim 1.1$ is

$$\frac{L_{\text{CS}}^{\text{th}}}{L} \approx 1.25 \left(1 + \frac{3\varphi}{\alpha - 1} \right) \left(\frac{\eta}{Nmr_{\text{b}}^2} \right)^{0.37} \frac{\Theta^{3.66}}{\alpha^{0.19}}. \quad (5.10)$$

From equations (5.9)–(5.10) we find that in most cases the coronal model yields much lower values of $L_{\text{CS}}^{\text{th}}$ than the model of a hot accretion flow of Section 5.1.1. For the hard state of Cygnus X-1 with $\eta = 0.02$ and $m = 10$ (Section 5.1.1) we find $L_{\text{CS}}^{\text{th}}/L \approx 1.7 \times 10^{-2}$, which is ~ 20 times less than $L_{\text{CS}}^{\text{th}}/L$ obtained in the hot flow model. Only an extremely low and inconsistent with equation (5.8) value of $r_{\text{b}} \sim 10^{-5}$ would lead to $L_{\text{CS}}^{\text{th}} = L$ in this case. For objects with softer spectra, even lower values of $L_{\text{CS}}^{\text{th}}/L$ are obtained. For objects with low luminosities, Comptonized bremsstrahlung would dominate, see equation (3.40), which applies to all coronal models discussed here with $R = Nr_{\text{b}}R_{\text{g}}$.

Thus, thermal synchrotron radiation cannot be a substantial source of seed photons for Comptonization in active coronal regions with equipartition between magnetic field and radiation, even for weak sources. This finding can be explained by considering consequences of this equipartition in the presence of strong synchrotron self-absorption. With neither self-absorption nor additional sources of seed photons, equipartition between the energy densities in the field and in photons leads to the net Comptonization luminosity, L_C , roughly equal to the synchrotron luminosity, L_S , which then implies $\alpha \sim 1$. (An additional assumption here is the validity of the Thomson limit, e.g. Rybicki & Lightman 1979.) However, strong self-absorption in a thermal plasma with parameters relevant to compact sources dramatically reduces L_S , i.e., $L_S \ll L_C$. Then, a very hard Comptonization spectrum, with $\alpha \sim 0$, is required to upscatter the few synchrotron photons into a spectrum with luminosity of L_C . On the other hand, if $\alpha \sim 1$, as typical for compact cosmic sources, CS photons would give only a tiny contribution to the actual coronal luminosity, L , and other processes, e.g. Comptonization of blackbody photons from the underlying disc would have to dominate.

This conclusion differs from findings in Di Matteo et al. (1997b) as well as in Di Matteo, Celotti & Fabian (1999) that this process is often important under conditions typical to compact objects, in particular in GX 339–4. This discrepancy stems mostly from their assumption of $\eta = 1$ (i.e., $L = L_E$) for calculating the value of B in those papers (T. Di Matteo, private communication). This is inconsistent with observations (as we observe $L \ll L_E$ in this and other objects), unless only a small fraction of the dissipated power is radiated away.

They postulate that the remaining power is stored in magnetic fields (see section 2.2 in Di Matteo et al. 1997b). However, the supplied power has to be eventually either radiated away, transported away from the disc or advected to the black hole. In the first case, we would recover our result of $L_{CS}^{th} \ll L$. In the second, the power in magnetic fields should be converted to kinetic power of a strong outflow. Finally, the advection time scale of an optically-thick disc is probably much longer than the time scale for dissipation of coronal magnetic fields. Besides, $\eta = 1$ would often require accretion rates much higher than those estimated from the physical parameters of X-ray binaries (see, e.g., Zdziarski et al. 1998 for the case of GX 339–4).

In addition, the values of Θ assumed in Di Matteo et al. (1997b) and Di Matteo et al. (1999) for luminous states of black-hole sources are significantly higher than those used in the examples shown in this work (which were derived from the best currently-available data). Due to the strong dependence of L_{CS}^{th} on Θ [see eqs. (5.9)–(5.10)], this also results in higher values of L_{CS}^{th} .

We note that equation (5.9) can yield $L_{CS}^{th} \sim L$ for $\Theta \gtrsim 1$. This is partly explained by most of energy density in Comptonized photons being then in the

Klein-Nishina limit. Then, the energy density of photons in the Thomson limit is much smaller than the total energy density, and thus more comparable with energy density of self-absorbed synchrotron photons. Thus, the CS process is expected to play an important role in sources with $\Theta \gtrsim 1$. Note, however, that equations (5.9)–(5.10) break then down as the approximations of equations (3.23) and (3.28) become invalid and numerical calculations should be employed in that case.

5.1.3 Coronal model – dissipation of magnetic field

As discussed by, e.g., Di Matteo, Blackman & Fabian (1997a), the strength of the coronal magnetic field is expected to be higher than the equipartition value of equation (5.6). If an active region is powered by dissipation of magnetic field and the dissipation velocity is gv_A , where $g \leq 1$ and $v_A = B/(4\pi n_e m_p \mu_e/\mu_i)^{1/2}$ is the Alfvén speed, the energy density stored in the field will be c/gv_A times that in radiation (which escapes the source with the velocity c), and $h_b/r_b \sim g$, where $h_b R_g$ is the scale height of the active region (Longair 1992). Then, for a given $g = h_b/r_b$ and accounting for the dependence of the radiation density on geometry, we have,

$$\frac{B^2}{8\pi} \frac{gv_A}{c} \approx \frac{9}{4(3+g)\pi} \frac{L}{N(r_b R_g)^2 c}. \quad (5.11)$$

Using the approximation of equation (3.28), we have then

$$B \approx \frac{9.8 \times 10^8 \eta^{1/3}}{r_b^{5/6} m^{1/2} \alpha^{5/24} \Theta^{5/24} [g(3+g)N]^{1/3}} \text{G}. \quad (5.12)$$

The luminosity in the CS emission is then approximately given by

$$\frac{L_{\text{CS}}^{\text{th}}}{L} \approx \frac{312(1+g)}{10^{2.25\alpha} [g(3+g)]^{0.61+0.3\alpha}} \frac{\Theta^{3.4-0.3\alpha} r_b^{0.48-0.76\alpha} (N/\eta)^{0.39-0.3\alpha} \varphi}{m^{0.46\alpha-0.09} \alpha^{0.5+0.25\alpha} (1-\alpha)}, \quad (5.13)$$

for $0.4 \lesssim \alpha \lesssim 0.9$, and

$$\frac{L_{\text{CS}}^{\text{th}}}{L} \approx 0.59 \left(1 + \frac{3\varphi}{\alpha-1}\right) \frac{(1+g)\Theta^{3.09} (N/\eta)^{0.09}}{[g(3+g)]^{0.91} m^{0.37} r_b^{0.28} \alpha^{0.76}} \quad (5.14)$$

for $\alpha \gtrsim 1.1$, where we accounted for the dependence of the source area on g .

We note that Di Matteo et al. (1997a) adopted $g = h_b/r_b = 0.1$, whereas Di Matteo (1998) assumed $g = 1$ but $h_b/r_b = 0.1$, which values are inconsistent. We set $g = h_b/r_b = 0.1$ in our examples below.

The values of $L_{\text{CS}}^{\text{th}}$ in this model are much higher than those in the previous case, but still relatively low. For Cygnus X-1 for the same parameters as above ($\eta = 0.02$, $N = 10$, $r_b = 2$), we find $L_{\text{CS}}^{\text{th}}/L \sim 1$, i.e. this model can, in principle, account for

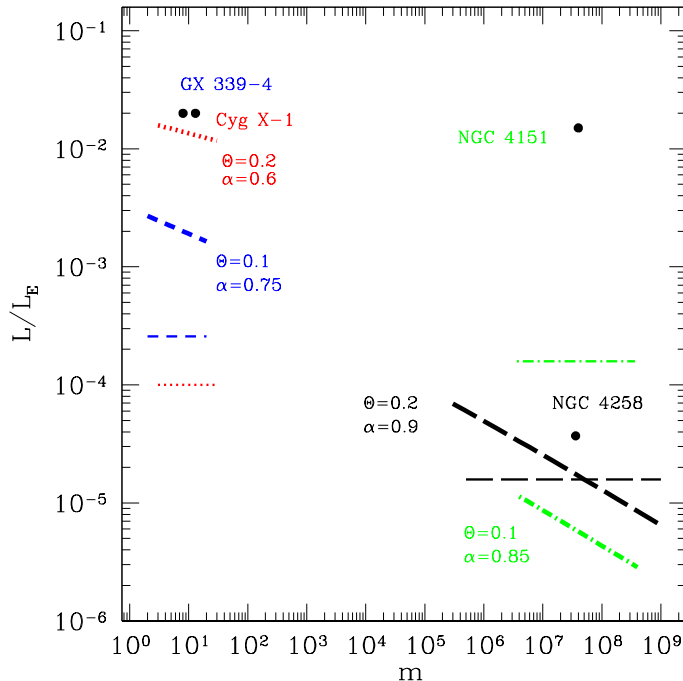


Figure 5.3: The same as Figure 5.2, but for the model of coronal dissipation of magnetic field, see Section 5.1.3.

the luminosity of this object. However, for objects with softer spectra, we obtain $L_{\text{CS}}^{\text{th}}/L \ll 1$, as shown in Figure 5.3 (which shows comparison with the same data as Figure 5.2, and $\eta = 0.01$ is assumed for the model curve corresponding to the average Seyfert-1 spectrum). We see that the predictions of this model for luminous sources, with $\eta \gtrsim 0.01$, are qualitatively similar to those of the hot flow model.

On the other hand, this model predicts values of $L_{\text{CS}}^{\text{th}}$ for weak objects much lower than those in the hot disc model. This can be seen by comparing the dependence on η in both cases. In the case of a hot flow, $L_{\text{CS}}^{\text{th}}$ does not depend on L , so formally $L_{\text{CS}}^{\text{th}}/L \propto \eta^{-1}$ (not including dependences of the plasma parameters on L). On the other hand, equations (5.13)–(5.14) yield roughly $L_{\text{CS}}^{\text{th}}/L \propto \eta^{-0.1}$ in the present case (which difference is mainly caused by the source area much smaller in the patchy corona model than in the hot flow model). Thus, decreasing L leads to only a marginal increase of $L_{\text{CS}}^{\text{th}}/L$. In contrast, the luminosity from Comptonized bremsstrahlung is about the same in the two models. Consequently, $L_{\text{CB}} \gg L_{\text{CS}}^{\text{th}}$ is typical of weak sources in the coronal models.

This is indeed the case for NGC 4258, where we have found it impossible to reproduce its 2–10 keV power-law index and luminosity even with $r_b \ll 1$, except for $\Theta > 1$. Although such a high temperature cannot be ruled out observationally at

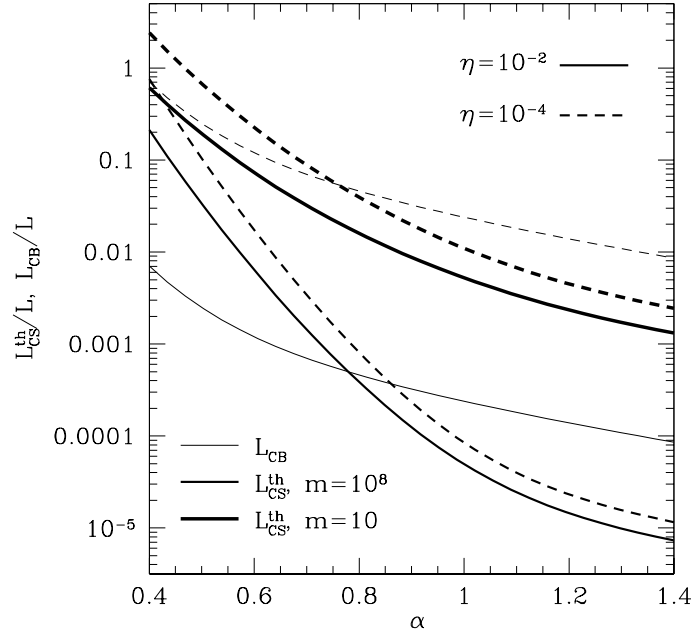


Figure 5.4: The fraction of the total coronal luminosity produced by the CS process (heavy and medium curves for $m = 10$ and $m = 10^8$, respectively) and by Comptonized bremsstrahlung (thin curves applying to both values of m) as a function of the spectral index of the CS radiation, for $\eta = 10^{-2}$ (solid curves) and $\eta = 10^{-4}$ (dashed curves) in the case of magnetic field of equation (5.11). See Section 5.1.3 for other parameters.

present, the corresponding Thomson optical depth is $\tau_T \ll 1$, which then would lead to a curvy spectrum reflecting individual scattering profiles. Then, the similarity of the X-ray spectral index of that object to the average index of Seyfert 1s would have to be accidental, which we consider unlikely.

Figure 5.4 shows a comparison of CS and Comptonized bremsstrahlung emission as functions of α for two values of m and two values of η , and for $g = 0.1$, $N = 10$, $r_b = 2$, $\Theta = 0.2$. As expected, bremsstrahlung dominates at low values of η and high values of α , and its Eddington ratio is independent of m .

5.1.4 Magnetic fields in the disc

The magnetic field strength in a corona is limited by equation (5.11) provided most of the energy of the field is dissipated there, which seems to be a likely assumption. That field depends on the factor g , whose value appears uncertain, and which could, in principle, be much smaller than unity.

However, unless there is a physical mechanism amplifying magnetic field in the corona (which could be the case e.g. of an accreting corona), the field strength will

be always lower than that inside the disc, B_d . The latter is in turn limited by equipartition with the disc pressure, as upward buoyancy forces will rapidly remove any excess magnetic flux tubes from the disc. Such a field strength was adopted by Di Matteo (1998) in calculations of the rate at which energy was supplied to a corona. It has to be noted however, that this is a robust upper limit only and magnetic field pressure was estimated as α_v times the gas pressure by Shakura & Sunyaev (1973), which would approximately correspond to multiplying equations (5.15)–(5.16) below by $\alpha_v^{1/2}$. Also results of numerical simulations by Hawley, Gammie & Balbus (1995; see Balbus & Hawley 1998 for a review) suggest that the magnetic field in the Shakura-Sunyaev disc should remain below the equipartition value.

Here, we utilize formulae for the vertically-averaged disc structure of Svensson & Zdziarski (1994), which take into account that a fraction, $f < 1$, of the energy dissipated in the disc is transported to the corona (see a discussion on the transport mechanisms in Beloborodov 1999). However, we recalculate the disc structure taking into account the additional pressure provided by the equipartition magnetic field. For consistency with the rest of this work, we assume equipartition with energy density rather than with pressure, which assumption has only a minor effect on our results. Expressions for B_d below are computed at $r = 11$, which is approximately the radius at which a radiation-dominated region first appears with increasing accretion rate (Svensson & Zdziarski 1994). For lower radii, somewhat higher values of B_d are obtained, but the contribution of those radii to the total dissipated power is small. In a disc region dominated by the gas pressure, we have then,

$$B_d \approx \frac{1.1 \times 10^8 \dot{m}^{2/5}}{(\alpha_v m)^{9/20} (1-f)^{1/20}} \text{ G}, \quad (5.15)$$

and we defined the dimensionless accretion rate, \dot{m} , in equation (1.4), so that the total luminosity (for a Schwarzschild black hole, which we assume) is $L = 0.06 \dot{m} L_E$.

In a disc region dominated by radiation pressure, we have,

$$B_d \approx 5.2 \times 10^7 [\alpha_v m (1-f)]^{-1/2} \text{ G}. \quad (5.16)$$

Note that the radiation-pressure dominated region appears only for accretion rates higher than certain value \dot{m}_{crit} . Hereafter, we will assume $\alpha_v = 0.1$ and that half of the accreted energy is dissipated in the corona, i.e., $f = 1/2$.

We first compare the maximum strength of coronal magnetic field of equation (5.11) with the disc field of equations (5.15)–(5.16). For parameters relevant to compact objects, the disc field is always stronger than the maximum coronal magnetic field, up to two orders of magnitude, except for extremely low accretion rates, $\dot{m} \lesssim 10^{-10}$. Thus the coronal models of Sections 5.1.2–5.1.3 are consistent with the limits on field amplification in the disc.

In general, given the uncertainties about the mechanism of magnetic field reconnection in active regions above accretion discs, we cannot rule out the presence of an average coronal field strength, $\langle B \rangle$, stronger than that predicted by the model of dissipation of magnetic field [equation (5.11)], and limited by equations (5.15)–(5.16),

$$\langle B \rangle = \varepsilon B_d, \quad (5.17)$$

where $\varepsilon < 1$ accounts for an inevitable decay of the field during a flare event. The dissipation rate of the magnetic field in a reconnection event is $\propto B^2$ (see e.g. section 12.4 in Longair 1992) so the field decays exponentially. Since the above average is weighted by the luminosity of an active region, which quickly decreases with decreasing B , ε can be, in principle, of the order of unity. Thus, we adopt $\varepsilon = 0.5$ in numerical examples below.

Assuming the magnetic field strength given by equation (5.17), we obtain for disc regions dominated by the gas pressure,

$$\frac{L_{\text{CS}}^{\text{th}}}{L} \approx \frac{200 \times 10^{-3.1\alpha}}{\alpha^{0.13+0.06\alpha}(1-\alpha)} \frac{\varepsilon^{1.82+0.91\alpha} N r_b^2 \Theta^{3.78-0.11\alpha} \dot{m}^{0.36\alpha-0.27} \varphi}{\alpha_v^{0.82+0.41\alpha} f(1-f)^{0.09+0.05\alpha} m^{0.41\alpha-0.18}} \quad (5.18)$$

for $0.4 \lesssim \alpha \lesssim 0.9$ and

$$\frac{L_{\text{CS}}^{\text{th}}}{L} \approx 0.052 \left(1 + \frac{3\varphi}{\alpha-1} \right) \frac{\varepsilon^{2.73} N r_b^2 \Theta^{3.66} \dot{m}^{0.09}}{\alpha_v^{1.23} f(1-f)^{0.14} m^{0.23} \alpha^{0.19}} \quad (5.19)$$

for $\alpha \gtrsim 1.1$. Similar expressions can be derived for regions dominated by the radiation pressure.

Figure 5.5 shows the above ratios for the same values of α , Θ and m (except that $m = 10^8$ was assumed for the average Seyfert 1 spectrum) as in Figure 5.2, as functions of \dot{m} for $\varepsilon = 0.5$, $r_b = 2$, and $N = 10$. We see that the obtained luminosity is comparable to the one dissipated in the corona only in the case of Cygnus X-1. In other cases, the CS process gives a small contribution, comparable to or lower than the contribution of bremsstrahlung. We caution that the plasma parameters inevitably change with \dot{m} , and thus the CS and bremsstrahlung luminosities shown for values of \dot{m} significantly different from those derived from observations cannot be trusted.

In the case of NGC 4258, we can reproduce the 2–10 keV power-law index and luminosity with $\Theta = 0.43$ and $r_b = 2$. We note, however, that the CS luminosity is a sensitive function of the size of active regions in this model, $L_{\text{CS}}^{\text{th}} \propto r_b^2$ (which dependence is much stronger than that in the previous coronal models). Based on equation (5.8), we expect r_b decreasing with the decreasing L . If this is indeed the case for NGC 4258, the model of coronal CS emission could be then ruled out for this object (unless $\Theta > 1$, as in the case discussed in Section 5.1.3 above).

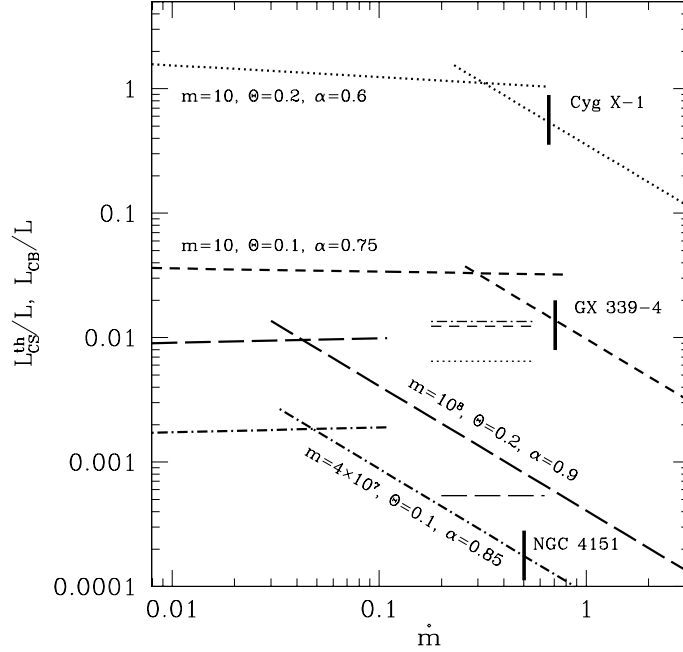


Figure 5.5: The ratio of the CS and Comptonized bremsstrahlung luminosities (heavy and thin lines, respectively; the latter ratio is independent of \dot{m}) to the power dissipated in a patchy corona as functions of the accretion rate in the case of the coronal magnetic field strength equal to 0.5 of that inside the disc. The solutions corresponding to dominance of the gas pressure and radiation pressure are shown for \dot{m} below and above $\sim \dot{m}_{\text{crit}}$, respectively. The chosen values of m , Θ , α are the same as in Figure 5.2. See Section 5.1.4 for details. The vertical bars mark our estimates of the accretion rates.

We therefore again conclude that, in coronal models, the thermal CS radiation can be important only in the case of stellar-mass sources with hard spectra. This radiative process is negligible in the case of objects with soft spectra (probably including low-luminosity sources) when Comptonization of photons from a cold accretion flow is expected to dominate. If the disc magnetic field pressure is less than that of equipartition, as discussed above, the predicted upper limits of $L_{\text{CS}}^{\text{th}}$ would be even lower.

5.1.5 General remarks

A general feature of models of accretion flows we used above is the dependence of $B \propto m^{-1/2}$ [or very close to it, equation (5.15)]. This then implies decreasing values of $L_{\text{CS}}^{\text{th}}/L_{\text{E}}$ with m , and the relative importance of the thermal CS process much weaker in AGNs than in BHs. The predicted values of $L_{\text{CS}}^{\text{th}}$ strongly increase with increasing spectral hardness and temperature of the plasma. Both models can, in principle, explain emission of the hardest ($\alpha \lesssim 0.6$) among luminous (Eddington ratios of ~ 0.01), stellar-mass sources in terms of the thermal CS process. However, this process provides a negligible contribution to the X- and γ -ray emission of luminous BHs with soft spectra and of luminous AGNs regardless of α .

The hot flow and coronal models differ in their predictions for the relative importance of the CS process with decreasing L/L_{E} . In the hot flow model, there is clearly a range of $L/L_{\text{E}} \ll 0.01$, in which the CS process can yield a dominant contribution to L even in the case of AGNs. On the other hand, the coronal models have rather weak dependences of $L_{\text{CS}}^{\text{th}}/L$ on L/L_{E} . However, at some low value of L/L_{E} , bremsstrahlung emission becomes dominant. Therefore, we have found that, in the coronal models, there is no range of L/L_{E} (except for hard, stellar-mass sources, see above) in which the CS process could dominate energetically. In both models, bremsstrahlung is expected to give the main contribution to L in very weak sources.

There are, however, two complications in the picture above. First, the plasma parameters are expected, in general, to depend on L/L_{E} , which will modify theoretical dependences of $L_{\text{CS}}^{\text{th}}/L$ on the Eddington ratio. This is especially the case of the electron temperature, which is expected to be higher in low-luminosity sources, due to less efficient plasma cooling. This would strongly increase the efficiency of the CS process. We did not consider temperatures much higher than those observed in luminous objects. Unfortunately, we have as yet no observational constraints on the plasma temperature in low-luminosity sources.

Second, we have considered here accretion onto non-rotating black holes. Black-hole rotation increases, in general, the efficiency of accretion, and the CS process may yield then luminosities higher than those found here. This is, in fact, confirmed by a study of Kurpiewski & Jaroszyński (1999), who have considered advection-dominated flows and have found that an increase of the black-hole angular momentum leads to increase of the CS emission. This happens due to both the synchrotron emission itself as well its Comptonization becoming much more effective in innermost regions of the disc. Analysis of those issues is, however, beyond the scope of this work.

5.2 Hybrid CS emission

5.2.1 Efficiency of hybrid CS emission

With the use of the tools developed in Section 4.3.2 we can now estimate the efficiency of Comptonized synchrotron emission from a hybrid plasma, compared to the thermal case, for the accretion flow models introduced in the previous Section. For NGC 4151 we use exactly the same parameters of the source as those in Section 5.1.1, while for Cygnus X-1 and GX 339–4 we assume plasma parameters as obtained from observational constraints on the presence of non-thermal electrons (see below).

We first calculated the amplification of the CS emission due to the presence of non-thermal electrons in the frame of the hot flow model as a function of δ for the three sources. The results are shown in Figure 5.6. We can see that for all three sources, a non-thermal tail in the electron distribution as weak as $\delta \lesssim 10^{-3}$ amplifies the power produced by the CS process sufficiently to reproduce the observed luminosities of those sources. This shows that the hybrid CS emission is energetically capable of producing the observed hard X-ray and γ -ray spectra both in BHBs in their hard states and in Seyfert galaxies.

Unlike the thermal case, where the relative efficiency of the CS emission was much lower for AGNs, the hybrid CS emission is now efficient both for BHBs and AGNs. This stems from the fact that though the thermal CS emission is much less effective in AGNs, it is also much more amplified there by non-thermal effects, which we discussed in Section 4.2.2. Thus the hybrid CS emission turns out to be an efficient source of seed photons for Comptonization independent of the black hole mass or the luminosity.

This conclusion is qualitatively different from the one we have reached for the thermal case. A similar result can be obtained in the active regions model, since efficiencies of thermal CS emission were similar for the hot disc and active regions models, compare Figures 5.2 and 5.3.

5.2.2 Cygnus X-1

Hard state

In the case of hard state of Cygnus X-1, we use the electron distribution obtained by McConnell et al. (2000a) by fitting the spectra from the COMPTEL and OSSE detectors aboard *CGRO* with the *CompPS* model (the same we used in our fits to GX 339–4 data, Section 2.3), i.e. $\Theta = 0.17$, $\gamma_{\text{nth}} = 2.12$, $p = 4.5$, at assumed $\gamma_{\text{f}} = 10^3$, which corresponds to $\delta = 0.19$. We assume the source radius $r_0 = 20$, as in the thermal case. The equipartition field strength is $B = 6.3 \times 10^6$ G, which

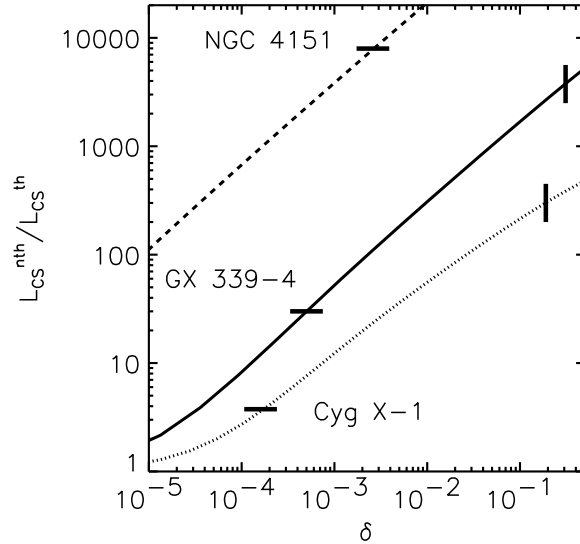


Figure 5.6: The amplification of the CS emission due to the presence of non-thermal electrons, $L_{\text{CS}}^{\text{nth}}/L_{\text{CS}}^{\text{th}}(\delta)$, for hot flow models of NGC 4151, GX 339-4 and Cygnus X-1 (dashed, solid and dotted curves, respectively). The horizontal lines correspond to the amplification required to account for the observed X-ray luminosities and the corresponding values of γ_{nth} are 2.61, 2.46, and 4.10 in the above three objects, respectively. Vertical lines correspond to δ obtained from observational constraints on non-thermal tails in Cygnus X-1 and GX 339-4.

value is calculated from equation (5.1), assuming that the spectral index is $\alpha = 0.6$ and with the use of the index – optical depth relation (3.25). The latter expression is appropriate for the thermal case which produces a small error in the hybrid case. This error is however negligible in this case, especially compared to uncertainties about the geometry (and so the real value of τ_{T}).

The estimated *thermal* CS luminosity in the case of Cygnus X-1 in the hot disc model was comparable to that observed from the source, see Figure 5.2. Then, we can see from Figure 5.6 that the non-thermal tail observed by McConnell et al. (2000a) would produce the CS luminosity ~ 100 times higher than that actually observed (see also Figure 4.2a, where thermal and hybrid synchrotron spectra are plotted for plasma parameters exactly as those assumed in this model). The requirement that $L_{\text{CS}}^{\text{nth}}$ cannot exceed the source luminosity constrains the magnetic field strength in the model to be $B \lesssim 6 \times 10^5$ G, which is ~ 10 times smaller than the equipartition value from equation (5.3).

A corresponding constraint for Cygnus X-1 can be obtained in a model of active coronal regions above the disc with magnetic field dissipation. Assuming $N = 10$ active regions of radius $r_b = 2$ and height $h_b = 0.2$ (i.e. as in Section 5.1.3), we obtain $B \lesssim 8 \times 10^6$ G, much less than the field strength required assuming dissipation of magnetic field [equation (5.11)], $B_{\text{diss}} = 5 \times 10^7$ G. Though varying N , R_b , H_b would change the upper limit on the field strength as well as the value of B_{diss} , the relation between these quantities would remain similar.

This results indicates that the mechanism of dissipation of disc field in small active regions above the disc cannot be responsible for the energy release in the corona. This stems from the fact that B_{diss} is the minimum field strength necessary for the magnetic field to dissipate enough energy so as to produce the observed luminosity. Therefore, either the model of active regions above a cold disc is not correct for the hard state of Cygnus X-1 or another mechanism of energy release must operate (but see discussion in Section 5.2.4).

We checked how sensitive the above results were to details of the observed spectra of Cygnus X-1. First, the spectral index of Cygnus X-1 varies, and the value $\alpha = 0.6$ assumed above (it could not be constrained observationally with enough precision) is the hardest one and spectra with $\alpha = 0.7$ have been also observed. Second, the relative normalization between the COMPTEL and OSSE spectra remains relatively uncertain, and it is possible that the former is less by ~ 2 (McConnell et al. 2000b) than the one used in the calculations above. This would then diminish the energy content in the electron non-thermal tail twice, which corresponds to the new value of $\gamma_{\text{nth}} = 2.31$. Thus, we have repeated our calculations for $\alpha = 0.7$ and $\gamma_{\text{nth}} = 2.31$. The resulting constraints on the magnetic field strength in the hot disc and active regions models are then $B \lesssim 1.3 \times 10^6$ G and $B \lesssim 1.4 \times 10^7$ G, respectively. These values are only about twice the previous upper limits, which does not affect our conclusions above.

Soft state

Given the above results, we checked whether also in the soft state of the object a similar constraint can be obtained. For that purpose we used a Cygnus X-1 soft state observation of Gierliński et al. (1999), which we refitted with the *CompPS* model for consistency with our other constraints. The plasma parameters we obtained were $\tau_T = 0.4$, $kT_e = 49$ keV, $p = 3.3$, $\gamma_{\text{nth}} = 1.68$, $\gamma_f = 19$, which corresponded to $\delta = 0.33$.

We then calculated the hybrid synchrotron spectrum, again from a hot flow of $R = 3 \times 10^7$ cm (i.e. the same size as in the model for the hard state), with the magnetic field strength $B = 3.2 \times 10^6$ G, calculated from equation (5.3). In Figure 5.7 we show the Comptonization continuum resulting from fits to the data (assuming

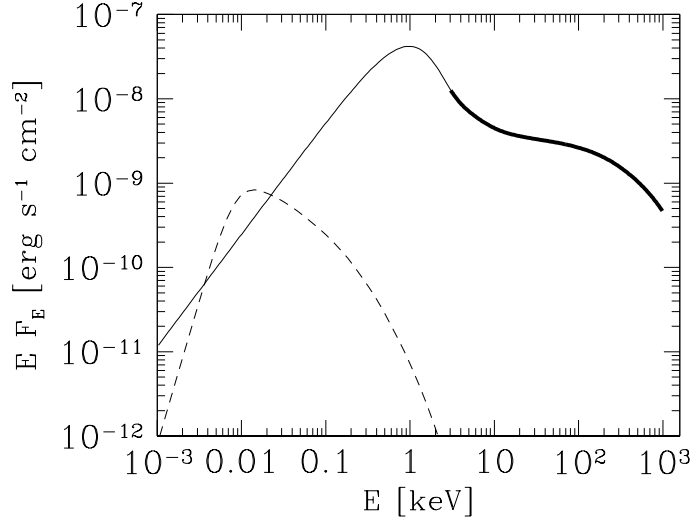


Figure 5.7: The hybrid synchrotron emission from a plasma in a hot flow, of parameters relevant for the soft state of Cygnus X-1 (dashed curve), compared against the spectrum from Comptonization of cold disc emission (solid curve) obtained from fits to the data in the range 3 – 1000 keV (thick) and extrapolated to lower energies (thin), see text.

that the observed disc emission of $kT_{\text{seed}} = 0.4$ keV is the source of seed photons), with absorption and contribution from reflection features and iron line neglected. Also the predicted synchrotron emission is plotted.

We see that the Comptonized synchrotron spectrum (of the shape similar to the Comptonization spectrum observed) would be by almost two orders of magnitude weaker, than the observed one. Since in the soft state the size of the inner hot flow is expected to be smaller than in the hard state (which we deduce from larger reflection and stronger gravitational effects, see Gierliński et al. 1999), the actual expected CS luminosity would be even lower. An identical result can be obtained for the active regions model. Thus, in the soft state the synchrotron emission, either thermal or hybrid, is negligible as a source of seed photons, compared to the prominent disc component and does not provide us with any constraints on the field strength.

It is interesting to note that the amount of non-thermal electrons is very similar in both states of Cygnus X-1. Then, the significant difference between the spectra in the two states (see Section 1.2.1) is due to different values of τ_T and kT_e . In the hard state the temperature and optical depth are higher, so that thermal Comptonization dominates, while in the soft state the non-thermal component is more prominent.

One can speculate that similar values of δ might suggest that similar energy release mechanisms operate in the two states. Then, it is possible that the difference between the two states is quantitative only and due to smaller optical depth of the

hot plasma accompanied by stronger cold disc emission in the soft state. This could be achieved if e.g. the hot phase was produced, at decreasing luminosity, by evaporation of the cold disc, which is in fact predicted by theoretical models (Róžańska & Czerny 2000).

5.2.3 GX 339–4

Similar constraints as above can be obtained for GX 339–4. We use hybrid plasma parameters, as fitted in Section 2.3.1, i.e. $kT_e = 48$ keV and $\gamma_{\text{nth}} = 1.63$, corresponding to $\delta = 0.31$.

As in the thermal case we assume for the hot flow model $R = 3 \times 10^7$ cm and the equipartition field strength (corresponding to the value of τ_T fitted to the data) is $B = 7.5 \times 10^6$ G. The hybrid CS luminosity would be then $L_{\text{CS}}^{\text{nth}} = 4.3 \times 10^{38}$ erg s^{-1} , which exceeds the observed one by a factor of ~ 40 . If we assumed $\delta = 0$, the CS luminosity would be $L_{\text{CS}}^{\text{th}} = 1.6 \times 10^{35}$ erg s^{-1} , i.e. the non-thermal tail in the electron distribution amplifies the synchrotron emission by a factor of $\sim 3 \times 10^3$. For the CS luminosity to equal the observed one, the magnetic field strength would have to be $B = 2.2 \times 10^6$ G, which value is a few times smaller than the equipartition strength in the hot flow.

In the active regions model (we assume the same values of N , R_b and H_b as for Cygnus X-1) the magnetic field required to dissipate enough energy so as to reproduce the source luminosity would be $B_{\text{diss}} = 4 \times 10^7$ G. Then, however, the CS luminosity from hybrid plasma would amount to $L_{\text{CS}}^{\text{nth}} = 4 \times 10^{38}$ erg s^{-1} , exceeding the observed one by a factor of ~ 30 . The CS luminosity would equal the observed one at $B = 7 \times 10^6$, when, however, magnetic field would not be able to dissipate enough energy.

Thus, the constraints we obtain for GX 339–4 are for both models very similar to those for Cygnus X-1.

5.2.4 General remarks

Observations suggest that the CS process in bright accreting black holes (at a few per cent of the Eddington luminosity) probably is not a dominant source of seed photons (see Section 1.5.3). In particular, the presence of a correlation between the spectral index and the strength of X-ray reflection (see Section 1.5.1) appears to imply that blackbody emission of the cold media where X-ray reflection occurs is the main source of seed photons for thermal Comptonization. This correlation becomes, however, substantially weaker for sources with hard spectra, $\alpha < 0.8$ (which is the case of all three objects we considered above), which would allow for some contribution of synchrotron emission to the seed photon flux. In either

case (if the synchrotron emission were either a negligible or only not a dominant source of seed photons) the magnetic field would have to be even weaker than that obtained from the above analyses, which would strengthen our constraints on the field strength.

The form of the non-thermal distribution we assumed [equation (4.1)] approximates well the true solution of the Fokker-Planck equation for relativistic electrons. However, when the power-law tail extends down to non-relativistic energies, $\gamma_{\text{nth}} \sim 1$, the distributions expected from acceleration processes are power laws in either the kinetic energy or the momentum, e.g. $\propto (\gamma - 1)^{-p}$ for the former. Clearly, the smaller γ_{nth} (i.e. the larger δ), the larger the difference between those distributions. Then, the actual modification of the synchrotron spectrum at a given value γ_{nth} would be somehow smaller than that we calculated in Section 4.2.2. Also, the relation between γ_{nth} and δ would change. Nevertheless, the above effects would modify our results only quantitatively without affecting our conclusions.

It has to be noted, however, that recently McConnell et al. (2002) fitted the same Cygnus X-1 COMPTEL and OSSE data, with models including X-ray reflection. They used the *CompPS* model as well as another model which calculates spectra from hybrid plasmas, namely *eqpair* of Poutanen & Coppi (1998). Then for the former they obtained $\delta = 1.36$, much larger than that resulting from *CompPS* fits of McConnell et al. (2000a), while the spectrum still closely resembled the thermal one, since the optical depth was sufficiently large (see Section 1.4.2). On the other hand we estimate from their *eqpair* fit parameters that this model yielded δ of the order of a few percent, i.e. smaller than the value we used. It has to be remembered, however, that the shape of non-thermal distribution is in general not a power-law in the *eqpair* model.

Thus, constraints on the electron distribution are still model-dependent and better quality data in the $\gtrsim 100$ keV range are required, so as to constrain more precisely both the shape of the cut-off and the high-energy tail in the spectrum.

The influence of a weak, non-thermal, component in the electron distribution on radiation spectra has also been independently considered by Özel, Psaltis & Narayan (2000). Their study has been devoted to the case of ADAFs, and their spectra are integrated over all radii of the flow. In contrast to our results, they do not note any shift in the turnover frequency at the peak of the synchrotron spectrum. This appears to result from their study being constrained to the ADAF model at low accretion rates, in which case electrons in the innermost parts of the accretion flow reach rather high temperatures, at which the amplification of synchrotron emission by a non-thermal tail is much weaker, see Section 4.2.2. These temperatures are significantly higher than those we consider based on observational data from luminous accreting black holes.

On the other hand, Özel et al. (2000) find a significant excess non-thermal emission at frequencies well below the peak of the integrated synchrotron spectrum. This excess results from radiation emitted at large radii, where the electron temperature is low, and where the synchrotron emission (both optically thick and optically thin) around the local turnover frequency can be strongly amplified by the presence of a non-thermal tail, as illustrated in Figure 4.2 above.

Also Ghisellini et al. (1998) compared the relative importance of Comptonization of synchrotron and disc photons in magnetically dominated, patchy coronae with hybrid plasmas. They assumed a given form of electron acceleration and then calculated the electron distribution taking into account a balance between the acceleration, escape, Compton cooling and synchrotron emission and self-absorption, which produced a hybrid distribution of the shape similar to ours. The magnetic field strength was constant for a series of models with varying luminosity, and their magnetic field was not directly compared to that produced in the disc.

Among the specific models they present, the CS process dominates only when $\Theta \sim 1$ and the magnetic energy density is more than one order of magnitude higher than that of radiation, see their figure 4. We find that the parameters of their models with the CS process dominating, correspond approximately to $\eta \sim 10^{-4}$, i.e. to low-luminosity sources, in our model above (assuming $r_b \sim 1$ and $N \sim 10$). Then, at $\Theta \sim 1$, we obtain predictions about the significance of the CS process similar to theirs.

Thus, though they considered hybrid electron distributions, their findings are in general compatible with our results for purely thermal plasmas in Section 5.1. This is most likely because Ghisellini et al. (1998) present the CS spectra only for those cases, when the equilibrium plasma distribution was very close to the thermal one and the temperature was high.

5.3 Relation between the optical and X-ray spectrum in GX 339–4

GX 339–4 was observed simultaneously by *Ariel-6* satellite in 1981 (Ricketts 1983) in X-rays (and was then classified as being in the hard state) and in the optical range (Motch et al. 1982). As we stated in Section 2.1, the optical emission of GX 339–4 is believed to originate not in the star, but in the disc or an outflow. It is therefore most likely produced by synchrotron processes, since blackbody emission of that strength from a Shakura-Sunyaev cold disc would require an enormous disc size and can be thus immediately rejected.

Motch et al. (1983) analyzed the source variability both in X-rays and in the optical band, concluding that quasi-periodic variability on the timescale of ~ 20 s was present in both energy ranges. On timescales longer than ~ 15 s variability in the 1 – 13 keV range anti-correlated with the optical variability, while a rather weak positive correlation was observed for the 13 – 20 keV band. Optical variability led the X-ray one by ~ 3 s. Besides, ~ 20 ms X-ray flares corresponded to dips in the optical band.

This allowed Fabian et al. (1982) to propose that the optical emission might be due to synchrotron radiation from a source of the temperature ~ 100 keV and the size of $\sim 10^8$ cm. Then, the optical emission would be correlated with harder X-rays produced in the same plasma, while anti-correlated with the softer X-ray band, which would be produced by emission from a cooler plasma of the temperature of a few keV. However, in all recent models of the hard state, the spectrum from a few to 13 keV is assumed to be produced in the same high-temperature plasma where harder X-rays, 13 – 20 keV, originate and where optical synchrotron emission should be produced (though above 10 keV the reflected component is also present in the spectrum).

It is in principle possible that for reasons e.g. related to the structure of magnetic field, synchrotron photon emission could be significantly more variable than the power delivered to the Comptonizing plasma. Then at the almost constant Comptonization luminosity and variable seed photon flux, the Comptonization spectrum would have to pivot for the luminosity to remain constant indeed. Then, if the pivoting took place between the optical and X-ray band we would observe an anti-correlation of the emission in the two bands. This would agree with the findings of Motch et al. (1983) for the soft X-ray band. However, the lack of an anti-correlation between optical emission and X-rays above 13 keV would pose a problem for the model. We also note here that the energy at which the spectrum should pivot is different from that we found in Section 2.4 when analyzing the X-ray variability.

There is an interesting similarity between GX 339–4 and an accreting black hole J1118+480 (Kanbach et al. 2001). Optical emission from this object is very strong. Also a similar anti-correlation between optical and X-ray flux was observed, with the optical minimum preceding the X-ray maximum by 2 – 5 sec. Unlike GX 339–4, optical emission then was found to peak ~ 0.5 s after the X-ray peak. Interestingly, optical spectrum had narrower auto-correlation function than X-rays, which may suggest that the primary variability is in the optical band (produced by synchrotron emission) which is then Comptonized.

We thus checked whether self-absorbed synchrotron radiation in an extended accretion flow could be energetically capable of producing the optical emission observed in GX 339–4. We were motivated by the fact that the spectrum from our

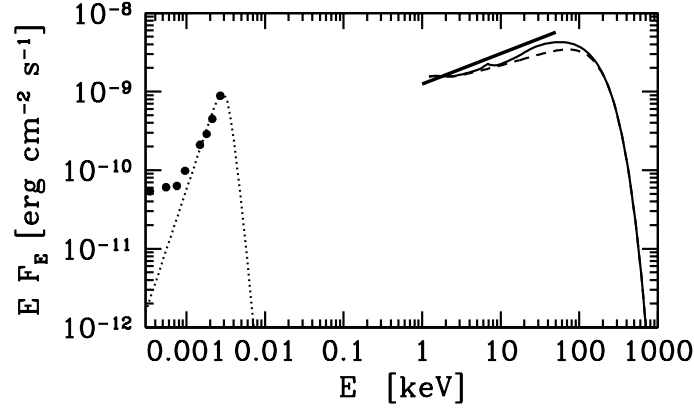


Figure 5.8: The optical spectrum of GX 339-4 from May 1981 observation (circles) and the power-law fit to the 1-50 keV simultaneous X-ray data (Ricketts 1983, thick straight line). Superimposed is our fit to the spectrum from *Ginga* and OSSE observation (in the observed range, 1.2 to 1000 keV), dataset 1, where solid line marks the total spectrum (soft excess neglected) and the dashed line represents the Comptonization continuum alone. The thin dotted line represents thermal synchrotron spectrum, see text.

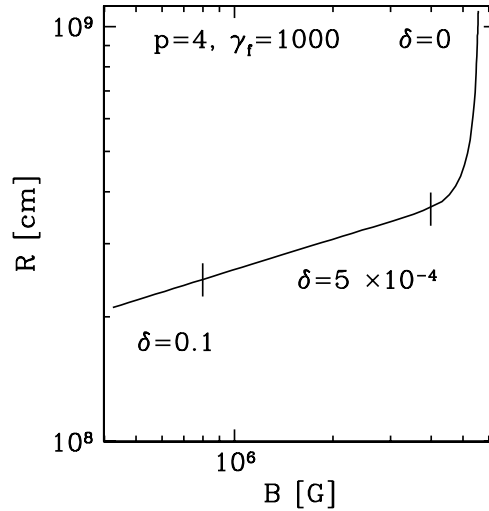


Figure 5.9: The relation between the size of the emitting region and the magnetic field strength inside, parameterized by the values of δ .

Ginga and OSSE observation, dataset 1 (Table 2.1), had turned out to be very similar to the X-ray spectrum obtained by Ricketts (1983), who fitted it in the range 1 – 50 keV by a power-law of index 1.5 (see Figure 5.8, where the optical and X-ray spectra are shown). Then, the extension to lower energies of the underlying continuum power-law component in our spectrum would match the optical spectrum at a flux by a factor of ~ 5 weaker. This might correspond to a situation where a part of the optical synchrotron emission is Comptonized (we remind that the *Ginga* data do not constrain precisely the soft photon source). However, if the interpretation of the variability pattern we proposed in Section 2.4 were correct, it would rule out the interpretation of the optical emission as being the source of seed photons for Comptonization, due to different pivoting energy required.

We assumed that the uppermost observational point in the optical spectrum, at the energy $E = 2.7$ eV and the observed flux $F_E = 8.9 \times 10^{-10} \text{ cm}^{-2} \text{ s}^{-1}$ corresponded to synchrotron emission at the turnover frequency, where the plasma becomes optically thin to synchrotron absorption. Then, assuming plasma temperature and optical depth as fitted to dataset 1, we calculated numerically the magnetic field strength and spherical source size, the emission of which would reproduce these two values. The results are presented in Figure 5.9, where the relation between the source size and the required field strength is parameterized by the amount of energy carried by non-thermal electrons (for which case we assumed $p = 4$ and $\gamma_f = 1000$), i.e. for a given δ we read the required values of B and R from the plot. We see that for a purely thermal plasma the required source size would be $R \sim 10^9$ cm, at $B \sim 6 \times 10^6$ G. For $\delta \gtrsim 0.1$, the values of R and B are by an order of magnitude smaller. At the same time, the magnetic field strength expected in a hot accretion disc flow, if the field remained in equipartition with pressure (dominated by virial ions) would be $B \sim 10^6$ G at $R \sim 10^8$ cm and $B \sim 10^5$ G at $R \sim 10^9$ cm.

As a reference, we have shown in Figure 5.8 thermal synchrotron spectrum which luminosity and turnover frequency match the optical data. Note that in general the self-absorbed synchrotron spectrum (below the turnover frequency) will be softer than that presented, due to superposition of emission from regions of different plasma parameters.

We conclude that if non-thermal electrons were present at the amount found both in our dataset 4 and in the hard state of Cygnus X-1, synchrotron emission from outer regions of the accretion flow of $R \gtrsim 10^8$ cm could possibly explain the observed optical and X-ray spectrum. We note that the timescale of quasi-periodic oscillations (QPOs), ~ 20 s in the data reported by Motch et al. (1983) and ~ 3 s for the data from our dataset 4 (Revnivtsev et al. 2001) corresponds to Keplerian orbits at $R \sim 10^9$ s (assuming $M = 10M_\odot$), while the flares timescale, 20 ms, is of the order of light-crossing time for such a region.

If this were the case, it would pose a serious problem for accretion disc modelling. A highly non-local energy dissipation mechanism would be required, since most of the gravitational energy is liberated at much smaller radii. It also has to be noted that contemporary models of QPOs predict that they are not directly connected to the Keplerian frequency and are in fact produced at much smaller radii (e.g. Belloni et al. 2002).

Optical emission could also originate in an elongated outflow, possibly a jet, which presence is suggested by radio observations (Fender et al. 1997 and references therein; Corbel et al. 2000). Such an interpretation is further encouraged by quenching of radio emission during the soft state of the object, where the hot flow is suppressed (Fender et al. 1999). However, there is no natural interpretation to the frequency of the QPO in this model.

The profile of optical emission lines favours the outflow hypothesis, since double-peaked emission lines have been found in the soft state of GX 339-4 by Soria et al. (1999), while they observed broad, single-peaked profiles in the hard state. They attributed the difference in the line profiles to the origin of the line, suggesting that it had been produced in the outflow in the hard state and in the disc in the soft state.

A possible way to distinguish between the two cases would be to measure the polarization of the optical radiation, which should be non-zero for an outflow with a directed magnetic field. If the optical emission were indeed due to synchrotron emission from an outflow, this might nevertheless constitute another source of soft photons undergoing Comptonization. On the other hand, if the seed photons for Comptonization were *not* produced in the outflow, then the optical data might in principle pose some constraints on the outflow configuration relative to the Comptonizing corona.

Chapter 6

Summary

In this Thesis we have investigated, on the theoretical side, the process of synchrotron emission and its Comptonization in optically thin, semi-relativistic plasmas of parameters typical for accreting black holes.

We reviewed analytical approximations of synchrotron emission found in the literature and developed more useful formulae. We also quantitatively analyzed the modification of the synchrotron emission spectrum when a weak non-thermal component is present in the electron distribution.

With the use of the model of Zdziarski (1985) we developed an analytical description of the Comptonization of synchrotron emission both in thermal and hybrid plasmas. Approximate formulae for the luminosity produced by this process have been obtained. In particular they allow for calculating the *amplification* of the CS emission due to the presence of non-thermal electrons in the plasma. This in turn allows for direct comparison of the efficiency of thermal and hybrid CS processes, when the former has been calculated with other models.

For estimates of efficiency of the CS emission, we introduced two simplified models of accretion flows. The first describes a hot, two-temperature, optically thin accretion flow, which corresponds to the model of Shapiro et al. (1976) or to an optically thin ADAF. The other model describes a patchy corona above a cold disc, where the magnetic field strength is related to the energy dissipated in the process of reconnection. In this approach main features of more advanced models have been retained, while it allows for easy analytical estimates of the luminosity produced by CS processes in accretion flows.

On the observational part, we analyzed X- and γ -ray data from four observations of a Galactic black hole candidate, GX 339–4, when the source was in its hard state and from one observation when the object was found in the off state. For that purpose models of Comptonization and relativistic reflection were used. We were able to constrain the most important parameters of these models with reasonably

good accuracy and in one of the observations we estimated the extent to which the Comptonizing plasma could be hybrid.

The results of spectral and temporal analyses we had obtained were discussed in the general frame of accretion flow models. Furthermore we investigated the relation between X-ray and optical emission in GX 339–4, the latter attributed to synchrotron radiation.

The tools describing analytically the CS emission in accreting black holes allowed us to obtain constraints on the efficiency of this process. For that purpose we used observational data from the hard state of GX 339–4 (our own analysis of the data) as well as from Cygnus X-1 and Seyfert galaxies, NGC 4151 and NGC 4258 (data analyzed by other authors). We obtained such constraints both for thermal and hybrid plasmas and discussed the differences between the two cases. In the latter one we were able to obtain constraints on the magnetic field strength in accreting black holes.

Efficiency of thermal CS process

We have checked that the thermal synchrotron radiation in a *purely thermal* plasma is in general an ineffective source of seed photons for Comptonization in *luminous* (i.e. at $L/L_{\text{Edd}} \gtrsim 0.01$) sources. The results we obtained for plasma parameters typical for hard state BHBs and Seyfert 1s showed that the CS process would be energetically capable of reproducing the observed spectra only of BHBs with very hard spectra ($\alpha \lesssim 0.6$) like Cygnus X-1. The conclusions were almost identical within both frameworks we used, the hot disc model and the model of active regions.

On the other hand, the CS process in a hot flow can dominate the spectrum of low-luminosity AGNs ($L/L_{\text{Edd}} \ll 0.01$), though in this case also contribution from bremsstrahlung emission at large radii can be important in γ -rays. On the contrary, the CS process in the coronal model was found to be inefficient also in low-luminosity sources.

The results for the hot flow model are not new in fact, as it was already estimated by Shapiro et al. (1976) that thermal synchrotron emission cannot provide enough seed photons for Comptonization in Cygnus X-1. However, it has been recently suggested that the thermal CS emission can be effective enough in the model of active regions (e.g. Di Matteo et al. 1997b) and we showed that these results were incorrect.

Efficiency of hybrid CS process

We found that adding a weak non-thermal component to the electron distribution changes the efficiency of CS emission dramatically, because in a thermal plasma

these are high-energy electrons from the tail of the Maxwellian distribution that are responsible for most of the luminosity produced in a self-absorbed synchrotron spectrum. Thus, a non-thermal tail as weak as carrying only $\sim 10^{-3}$ of the energy of the thermal distribution can amplify the synchrotron emission by orders of magnitude, so that its Comptonization is energetically capable of reproducing the observed X- and γ -ray spectra of Seyfert 1 galaxies and BHBs independent of their mass or the luminosity. These conclusions are very weakly sensitive to the exact shape of the hybrid electron distribution, and the energy content of the non-thermal tail is the main parameter controlling the efficiency of hybrid CS. The exception here is the soft state of BHBs, where the blackbody component is so strong that the hybrid synchrotron emission is negligible as a source of soft photons.

Unlike the case of thermal CS emission, the efficiency of hybrid CS processes does not decrease with the luminosity or the black hole mass. First, this is because the amplification of the CS emission (compared to the thermal one) is particularly strong when the temperature is low and the Thomson optical depth large, which is the configuration found in the most luminous sources. Second, the amplification is much larger for supermassive black holes, as a result of weaker magnetic fields.

We believe the importance of our result concerning hybrid CS emission lies in particular in showing that the exact shape of the electron distribution is much more important for accretion flow models than previously thought. From the point of view of observers, the data from Seyfert 1s and BHBs in their hard states could be well fitted with thermal models and only in a few cases the data directly supported the presence of hybrid distributions. Even in those cases, the quality of the data was too low to constrain the shape of the electron distribution (in particular the exact slope of the power-law tail) precisely. Thus, with these data it is impossible to deduce what acceleration processes heat electrons in accretion flows (which is a very important question from the point of view of disc dynamics) and this is why hybrid distribution were not interesting from the point of view of theoreticians. Instead, we show that – since everything suggests that magnetic fields do have to be present in accretion flows – the existence of hybrid distributions has much more direct consequences for accretion flow models and has to be taken into account already in the analyses of currently available data.

Another consequence of our findings is that the CS emission should be now taken into account in modelling of radiative processes from luminous accreting black holes. It would be e.g. interesting to test the reflection – index correlation (Zdziarski et al. 1999) against the efficiency of CS processes, i.e. to find out how strong CS emission is allowed by this correlation for sources with harder spectra, where the correlation becomes weaker.

Constraints on the magnetic field strength

Probably the most important of our results is that it is possible to obtain an observational upper limit on the magnetic field strength in the optically thin plasma close to the black hole. This is because the hybrid CS process in accreting black holes is efficient enough to produce luminosities exceeding the observed ones, unless the magnetic field is sufficiently weak. Observations suggest that synchrotron emission is a negligible source of seed photons, and thus the CS emission should be much lower than that observed, which would further strengthen the limits we obtain.

There are, however, two limitations to this method. First, its results are model-dependent, in the sense that we can constrain the field from above not from first principles, but within a particular model, which is not necessarily correct. On the other hand, in this way consistency of models involving magnetic fields can be checked. Second, since the CS luminosity depends strongly on the amount of non-thermal electrons, the uncertainties in available constraints on the latter imply a large uncertainty in our constraints on the field strength. Also, as we have discussed in Sections 2.3.1 and 5.2.4, the obtained electron distribution functions depended on the details of modelling the data.

Keeping all those limitations in mind, we nevertheless attempted at constraining the field strength in GX 339–4 and Cygnus X-1. The observational constraints were much stronger for the latter source (due to COMPTEL data available), but we nevertheless obtained similar conclusions. In the model of hot, optically thin flow, the maximum allowed field strength was by an order of magnitude smaller than that corresponding to equipartition with gas pressure. Similar limit was obtained on the theoretical grounds, with investigations of the magneto-rotational instability (e.g. Balbus & Hawley 1998) for optically thick discs and for optically thin flows it would be expected to be similar (M. Begelman, private communication).

On the other hand, we found that in the model of active coronal regions the limiting field strength is too weak (by an a factor of a few) to liberate enough energy and thus the model might be unphysical. This conclusion should be however treated cautiously, since we used a simplified model of the release of magnetic field energy, in particular because this process is dynamical while we dealt with time-averaged quantities. It could be also in principle possible that the regions where electrons are accelerated by magnetic fields and where they radiate their energy are separated. Thus, apart from necessity for better quality data, also more sophisticated modelling of coronal dissipation of magnetic field is necessary to strengthen our conclusions.

Conclusions specific to GX 339–4

The observations of GX 339–4 we analyzed served not only for constraining the hybrid distribution. In particular, we found a relation between the temperature (or rather electron mean energy, since we considered hybrid distributions) of the Comptonizing plasma and the luminosity, with the temperature decreasing at increasing brightness. This trend can be explained in the frame of advection dominated flows.

The hybrid synchrotron emission from a hot, optically thin accretion disc would be, at least energetically, capable of reproducing the optical spectrum of GX 339–4. It could be then self-Comptonized to produce the observed X- and γ -ray spectrum. The required source size would be, however, $\gtrsim 10^8$ cm and thus inconsistent with contemporary accretion flow models, which predict energy release at smaller radii. We concluded that the optical emission was more likely to be produced by an outflow.

This is supported by our interpretation of the energy-dependent X-ray variability of the source on short time scales as due to variable soft photon flux at a constant power dissipated in the Comptonizing plasma. This interpretation requires the temperature of seed photons to be > 0.1 keV and thus rules out the possibility that synchrotron emission (at energies $\ll 0.1$ keV) constitutes a source of seed photons in the hard state of GX 339–4. Thus, if this interpretation of the variability pattern were correct, it would strengthen our constraints on the magnetic field in this object.

Bibliography

- Abramowicz M. A., Czerny B., Lasota J. P., Szuszkiewicz E., 1988, *ApJ*, 332, 646
- Abramowicz M. A., Chen X.-M., Granath M., Lasota J.-P., 1996, *ApJ*, 471, 762
- Abramowicz M. A., Igumenshchev I. V., Quataert I., Narayan R., 2002, *ApJ*, 565, 1101
- Abramowitz M., Stegun I. A., 1970, *Handbook of Mathematical Functions*. Wiley, New York
- Anders E., Ebihara M., 1982, *Geochim. Cosmochim. Acta*, 46, 2363
- Antonucci R. R. J., Miller J. S., 1985, *ApJ*, 297, 621
- Arnaud K. A., 1996, in Jacoby G. H., Barnes J., eds., *Astronomical Data Analysis Software and Systems V*, ASP Conf. Series Vol. 101, San Francisco, p. 17
- Baganoff F. K. et al., 2001a, *ApJ*, submitted (astro-ph/0102151)
- Baganoff F. K. et al., 2001b, *Nature*, 413, 45
- Balbus S. A., Hawley J. F., 1991, *ApJ*, 376, 214
- Balbus S. A., Hawley J. F., 1998, *Rev. Mod. Phys.*, 70, 1
- Bekefi G., 1966, *Radiation Processes in Plasmas*. Wiley, New York
- Belloni T., Psaltis D., van der Klis M., 2002, *ApJ*, in press (astro-ph/0202213)
- Beloborodov A. M., 1998, *MNRAS*, 297, 739
- Beloborodov A. M., 1999, *ApJ*, 510, L123
- Bisnovatyi-Kogan G. S., Blinnikov S. I., 1977, *A&A*, 59, 111
- Bisnovatyi-Kogan G. S., Lovelace R. V. E., 1997, *ApJ*, 486, L43
- Blandford R. D., Znajek R. L., 1977, *MNRAS*, 179, 433
- Blandford R. D., Payne D. G., 1982, *MNRAS*, 199, 883
- Blandford, R. D., Begelman M. C., 1999, *MNRAS*, 303, L1
- Böttcher M., Liang E. P., Smith I. A., 1998, *A&A*, 339, 87
- Bouchet L. et al., 1993, *ApJ*, 407, 739
- Chandrasekhar S., 1960, *Proc. Natl. Acad. Sci.*, 46, 253
- Chanmugam G., Barrett P. E., Wu K., Courtney M. W., 1989, *ApJS*, 71, 323

- Chen W., Shrader C. R., Livio M., 1997, *ApJ*, 491, 312
- Chen X., Abramowicz M. A., Lasota J. P., 1997, *ApJ*, 476, 61
- Clavel J., et al., 1987, *ApJ*, 321, 251
- Corbel S., Fender R. P., Tzioumis A. K., Nowak M., McIntyre V., Durouchoux P., Sood R., 2000, *A&A*, 359, 251
- Cunningham, C. T., 1975, *ApJ*, 202, 788
- Dermer C. D., Miller J. A., Li H., 1996, *ApJ*, 456, 106
- Di Matteo T., 1998, *MNRAS*, 299, L15
- Di Matteo T., Blackman E. G., Fabian A. C., 1997a, *MNRAS*, 291, L23
- Di Matteo T., Celotti A., Fabian A. C., 1997b, *MNRAS*, 291, 805
- Di Matteo T., Celotti A., Fabian A. C., 1999, *MNRAS*, 304, 809
- Di Salvo T., Done C., Życki P. T., Burderi L., Robba N. R., 2001, *ApJ*, 547, 1024
- Done C., 2002, *Philosophical Transactions of the Royal Society*, submitted (astro-ph/0203246)
- Done C., Mulchaey J. S., Mushotzky R. F., Arnaud K. A., 1992, *ApJ*, 395, 275
- Dulk G. A., 1985, *ARA&A*, 23, 169
- Eckart A., Genzel R., 1996, *Nature*, 383, 415
- Epstein R. I., Feldman P. A., 1967, *ApJ*, 150, 109
- Esin A. A., McClintock J. E., Narayan R., 1997, *ApJ*, 489, 865
- Fabian A. C., Guilbert P. W., Motch C., Ricketts M., Ilovaisky S. A., Chevalier C., 1982, *A&A*, 111, L9
- Fabian A. C., Rees, M. J., Stella, L., White, N. E., 1989, *MNRAS*, 238, 729
- Felten J. E., Rees M. J., 1972, *A&A*, 17, 226
- Fender R. P., Spencer E. R., Newell S. J., Tzioumis A. K., 1997, *MNRAS*, 286, L29
- Fender R. et al., 1999, *ApJ*, 519, L165
- Feng Y. X., Zhang S. N., Sun X., Durochoux P., Chen W., Cui W., 2001, *ApJ*, 553, 394
- Frontera F. et al., 2001, *ApJ*, 546, 1027
- Galeev A. A., Rosner R., Vaiana G. S., 1979, *ApJ*, 229, 318
- Gammie C. F., Popham R., 1998, *ApJ*, 498, 313
- Ghisellini G., Svensson R., 1990, in Brinkmann W. et al., eds., *Physical Processes in Hot Cosmic Plasmas*. Kluwer Academic Publishers, p. 395
- Ghisellini G., Svensson R., 1991, *MNRAS*, 252, 313
- Ghisellini G., Haardt F., Fabian A. C., 1993, *MNRAS*, 263, L9
- Ghisellini G., Haardt F., Svensson R., 1998, *MNRAS*, 297, 348

- Ghisellini G., Guilbert P. W., Svensson R., 1988, *ApJ*, 334, L5
- Gierliński M., 2000, PhD Thesis, N. Copernicus Astronomical Center, Warsaw
- Gierliński M., Zdziarski A. A., Done C., Johnson W. N., Ebisawa K., Ueda Y., Haardt F., Philips B. F., 1997, *MNRAS*, 288, 958
- Gierliński M., Zdziarski A. A., Poutanen J., Coppi P. S., Ebisawa K., Johnson N. W., 1999, *MNRAS*, 309, 496
- Gilfanov M., Churazov E., Revnivtsev M., 1999, *A&A*, 352, 182
- Gilfanov M., Churazov E., Revnivtsev M., 2000, *MNRAS*, 316, 923
- Gilfanov M., Churazov E., Revnivtsev M., 2001, in *Proc. 5th CAS/MPG Workshop on High Energy Astrophysics*, in press (astro-ph/0002415)
- Ginzburg V. L., Syrovatskii S. I., 1969, *ARA&A*, 7, 375
- Gondek D., Zdziarski A. A., Johnson W. J., George I. M., McNaron-Brown K., Magdziarz P., Smith D., Gruber D. E., 1996, *MNRAS*, 282, 646
- Grabelsky et al., 1995, *ApJ*, 441, 800
- Grindlay J. E., 1979, *ApJ*, 232, L33
- Grove J. E. et al., 1998, *ApJ*, 500, 899
- Haardt F., Maraschi L., Ghisellini G., 1994, *ApJ*, 432, L95
- Hartmann D., Woosley S. E., Arons J., 1988, *ApJ*, 332, 777
- Hawley J. F., Gammie C. F., Balbus S. A., 1995, *ApJ*, 440, 742
- Heinz S., Begelman M. C., 200, *ApJ*, 535, 104
- Ichimaru S., 1977, *ApJ*, 214, 840
- Igumenshchev I. V., Abramowicz M. A., 1999, *MNRAS*, 303, 309
- Ivanenko D. D., Sokolov A. A., 1948, *Dokl. Akad. Nauk SSSR*, 59, 1551
- Iwasawa K. et al., 1996, *MNRAS*, 282, 1038
- Jackson J. D., 1975, *Classical Electrodynamics*. Wiley & Sons, New York
- Jaroszyński M., Abramowicz M. A., Paczyński B., 1980, *Acta Astr.*, 30, 1
- Johnson W. N., McNaron-Brown K., Kurfess J. D., Zdziarski A. A., Magdziarz P., Gehrels N., 1997, *ApJ*, 482, 173
- Jones, T. W., Hardee, P. E., 1979, *ApJ*, 228, 268
- Kanbach G., Straubmeller C., Spruit H. C., Belloni T., 2001, *Nature*, 414, 180
- King A. R., Davies M. B., Ward M. J., Fabbiano G., Elvis M., 2001, *ApJ*, 552, L112
- Kong A. K. H., Kuulkers E., Charles P. A., Homer L., 2000, *MNRAS*, 312, L49
- Kubota A., 2000, PhD thesis, Tokyo University, Tokyo
- Kurpiewski A., Jaroszyński M., 1999, *A&A*, 346, 713

- Lasota J.-P., Abramowicz M. A., Chen X., Krolik J., Narayan R., Yi I., 1996, *ApJ*, 462, 142
- Li H., Miller J. A., 1997, *ApJ*, 478, L67
- Li H., Kusunose M., Liang E. P., 1996, *ApJ*, 460, L29
- Lightman A. P., White T. R., 1988, *ApJ*, 335, 57
- Lightman A. P., Zdziarski A. A., 1987, *ApJ*, 319, 643
- Longair M. S., 1992, *High Energy Astrophysics*. Cambridge University Press, Cambridge
- Lynden-Bell D., 1969, *Nature*, 223, 690
- Maejima Y., Makishima K., Matsuoka M., Ogawara Y., Oda M., Tawara Y., Doi K., 1984, *ApJ*, 285, 712
- Mahadevan R., 1997, *ApJ*, 477, 585
- Mahadevan R., Narayan R., Yi I., 1996, *ApJ*, 465, 327
- Makishima K. et al., 1986, *ApJ*, 308, 635
- Makishima K. et al., 1994, *PASJ*, 46, L77
- Makishima K. et al., 2000, *ApJ*, 535, 623
- Malysheva L. K., 1997, *Astron. Lett.*, 23, 585 [in Russian: *AZh Pisma*, 23, 667]
- Markert T. H., Canizares C. R., Clark G. W., Lewin W. H. G., Schnopper H. W., Sprott G. F., 1973, *ApJ*, 184, L67
- Massey P., Johnson K. E., DeGioia-Eastwood K., 1995, *ApJ*, 454, 171
- McConnell M. L. et al., 1994, *ApJ*, 424, 933
- McConnell M. L. et al., 2000a, *ApJ*, 543, 928
- McConnell M. L. et al., 2000b, in McConnell M. L., Ryan J. M., eds., *AIP Conf. Proc. Vol. 510, The Fifth Compton Symposium*. Melville, New York, p. 114
- McConnell M. L. et al., 2002, *ApJ*, in press (astro-ph/0112326)
- Mirabel I. F., Rodriguez L. F., 1999, *ARA&A*, 37, 409
- Miyoshi M. et al., 1995, *Nature*, 373, 127
- Motch C., Ilovaisky S. A., Chevalier C., 1982, *A&A*, 109, L1
- Motch C., Ricketts M. J., Page C. G., Ilovaisky S. A., Chevalier C., 1983, *A&A*, 119, 171
- Mushotzky R. F., Done C., Pounds K. A., 1993, *ARA&A*, 31, 717
- Narayan R., Yi I., 1994, *ApJ*, 428, L13
- Narayan R., Yi I., 1995, *ApJ*, 452, 710
- Narayan R., McClintock J. E., Yi I., 1996, *ApJ*, 457, 821

- Narayan R., Mahadevan R., Grindlay J. E., Popham R. G., Gammie C., 1998, *ApJ*, 492, 554
- Novikov I. D., Thorne K. S., 1973, in: DeWitt C., DeWitt B., eds., *Black Holes*, New York, Gordon & Breach
- Nowak M. A., Wilms J., Dove J. B., 2002, *MNRAS*, in press (astro-ph/0201383)
- Osterbrock D. E., 1974, *Astrophysics of Gaseous Nebulae*. Freeman, San Francisco
- Özel F., Psaltis D., Narayan R., 2000, *ApJ*, 541, 234
- Pacholczyk A. G., 1970, *Radio Astrophysics*. Freeman, San Francisco
- Petrosian V., 1981, *ApJ*, 251, 727
- Petrosian V., McTiernan J. M., 1983, *Phys. Fluids*, 26, 3023
- Piraino S., Santangelo A., Ford E. C., Kaaret P., 1999, *A&A*, 349, L77
- Poutanen J., Svensson R., 1996, *ApJ*, 470, 249
- Poutanen J., Coppi P., 1998, *Physica Scripta*, T77, 57
- Poutanen J., Fabian A. C., 1999, *MNRAS*, 306, L31
- Press W. H., Teukolsky S. A., Vetterling W. T., Flannery B. P., 1992, *Numerical Recipes*. Cambridge Univ. Press, Cambridge
- Pringle J. E., 1976, *MNRAS*, 177, 65
- Puchnarewicz E. M., Mason K. O., Siemiginowska A., Fruscione A., Comastri A., Fiore F., Cagnoni I., 2001, *ApJ*, 550, 644
- Quataert E., Gruzinov A., 1999, *ApJ*, 520, 248
- Revnivtsev M., Gilfanov M., Churazov E., 2001, *A&A*, 380, 520
- Revnivtsev M., Borozdin K. N., Priedhorsky W. C., Vikhlinin A., 2000, *ApJ*, 530, 955
- Reynolds C.S., Young A. J., Begelman M. C., Fabian A. C., 1999, *ApJ*, 514, 164
- Rhoades C. E., Ruffini R., 1974, *Phys. Rev. Lett.*, 32, 324
- Ricketts M. J., 1983, *A&A*, 118, L3
- Robinson P. A., Melrose D. B., 1984, *Australian J. Phys.*, 37, 675
- Ross R. R., Fabian A. C., Young A. J., 1999, *MNRAS*, 306, 461
- Różańska A., Czerny B., 2000, *MNRAS*, 316, 473
- Rybicki G. R., Lightman A. P., 1979, *Radiative Processes in Astrophysics*. Wiley-Interscience, New York
- Scheuer P. A. G., 1968, *ApJ*, 151, L139
- Schott G. A., 1907, *Ann. Physik.*, 24, 635
- Schott G. A., 1912, *Electromagnetic Radiation*. Cambridge University Press
- Schwinger J., 1949, *Phys. Rev.*, 75, 1912

- Shakura N. I., 1972, *Sov. Astron.*, 16, 756
- Shakura N. I., Sunyaev R. A., 1973, *A&A*, 24, 337
- Shapiro S. L., Lightman A. P., Eardley D. M., 1976, *ApJ*, 204, 187
- Smith I. A., Liang E. P., 1999, *ApJ* 519, 771
- Smith I. A. et al., 1999, *ApJ*, 519, 762
- Soria R., Wu K., Johnston H. M., 1999, *MNRAS*, 310, 71
- Sunyaev R. A., Titarchuk L. G., 1980, *A&A*, 86, 121
- Sunyaev R., Revnivtsev M., 2000, *A&A*, 358, 617
- Svensson R., 1984, *MNRAS*, 209, 175
- Svensson R., Zdziarski A. A., 1994, *ApJ*, 436, 599
- Takahara F., Tsuruta S., 1982, *Prog. Theor. Phys.*, 67, 485
- Tanaka Y., Lewin W. H. G., 1995, in Lewin W. H. G., van Paradijs J., van den Heuvel E. P. J., eds., *X-Ray Binaries*, Cambridge Univ. Press, Cambridge, p. 126
- Tanaka Y. et al., 1995, *Nature*, 375, 659
- Thorsett, S. E., Chakrabarty, D., 1999, *ApJ*, 512, 288
- Titarchuk L., 1994, *ApJ*, 434 313
- Trubnikov B. A., 1958, *Doklady Akad. Nauk. SSSR*, 118, 913
- Trudolyubov S. et al., 1998, *A&A*, 334, 895
- Ueda Y., Ebisawa K. Done C., 1994, *PASJ*, 46, 107
- Ulrich M., Maraschi L., Urry M. C., 1997, *ARA&A*, 35, 445
- van der Klis M., 1994, *ApJS*, 92, 511
- Velikhov E. P., 1959, *Sov. Phys. JETP*, 9, 995
- Véron-Cetty M. P., Véron P., 2000, *The Astron. Astrophys. Review*, 10, 81
- Wardziński G., Zdziarski, A. A., 2000, *MNRAS*, 314, 183
- Wardziński G., Zdziarski, A. A., 2001, *MNRAS*, 325, 963 (Erratum: 2001, *MNRAS*, 327, 351)
- Wilms J., Nowak M. A., Dove J. B., Fender R. P., Di Matteo T., 1999, *ApJ*, 522, 460
- Wilms J. et al., 2001, *MNRAS*, 328, L27
- Wilson C. D., Done C., 2001, *MNRAS*, 325, 167
- Wind J. P., Hill E. R., 1971, *Australian J. Phys.*, 24, 43
- Witt H. J., Czerny B., Życki P. T., 1997, *MNRAS*, 286, 848
- Yamauchi S., Koyama K., 1993, *ApJ*, 404, 620
- Zdziarski A. A., 1985, *ApJ*, 289, 514
- Zdziarski A. A., 1986, *ApJ*, 303, 94

- Zdziarski A. A., 1998, *MNRAS*, 296, L51
- Zdziarski A. A., 1999, in Poutanen J., Svensson R., eds., *High Energy Processes in Accreting Black Holes*, ASP Conf. Series 161, p. 16
- Zdziarski A. A., 2000, in: Martens P. C. H. , Tsuruta S., Weber M. A., eds., *Highly Energetic Physical Processes and Mechanisms for Emission from Astrophysical Plasmas*, IAU Symp. 195, San Francisco, ASP, 153
- Zdziarski A. A., Johnson W. N., Magdziarz P., 1996, *MNRAS*, 283, 193
- Zdziarski A. A., Lubiński P., Smith D. A., 1999, *MNRAS*, 303, L11
- Zdziarski A. A., Fabian A. C., Nandra K., Celotti A., Rees M. J., Done C., Coppi P. S., Madejski G. M., 1994, *MNRAS*, 269, L55
- Zdziarski A. A., Poutanen J., Mikołajewska J., Gierliński M., Ebisawa K., Johnson W. N., 1998, *MNRAS*, 301, 435
- Życki P. T., Czerny B., 1994, *MNRAS*, 266, 653